GEMS & GEMOLOGY

SPRING 2021
VOLUME LVII

THE QUARTERLY JOURNAL OF THE GEMOLOGICAL INSTITUTE OF AMERICA

Internal Structures of Natural Pearls from *Pinctada maxima*

Identification of Resin-Filled Turquoise

Spinel Inclusions Chart

GEMS & GEMOLOGY

Spring 2021
VOLUME 57, No. 1

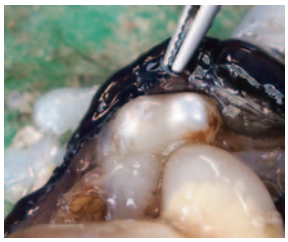
p. 6

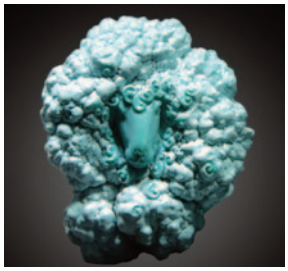
p. 23


p. 47


p. 69


p. 72

Editorial

Feature Articles

Charts

Regular Features

Editorial Staff

Editor-in-Chief
Duncan Pay

Managing Editor
Stuart D. Overlin
soverlin@gia.edu

Associate Editor
Brooke Goedert

Technical Editors
Tao Z. Hsu
tao.hsu@gia.edu

Jennifer Stone-Sundberg
jstone@gia.edu

Editors, Lab Notes
Thomas M. Moses
Shane F. McClure

Editors, Micro-World
Nathan Renfro
Elise A. Skalwold
John I. Koivula

Editors, Gem News
Emmanuel Fritsch
Gagan Choudhary
Christopher M. Breeding

Contributing Editors
James E. Shigley
Raquel Alonso-Perez

Editor-in-Chief Emeritus
Alice S. Keller

Assistant Editor
Erin Hogarth

Customer Service
Martha Erickson
(760) 603-4502
gandg@gia.edu

Production Staff

Creative Director
Faizah Bhatti

Photo/Video Producer
Kevin Schumacher

Photographer
Robert Weldon

Illustrator
Russel Samson

Multimedia Associate
Christopher Bonine

Production Supervisor
Richard Canedo

Video Production
Larry Lavitt
Pedro Padua
Albert Salvato

Editorial Review Board

Ahmadjan Abduriyim, Tokyo, Japan
Timothy Adams, San Diego, California
Edward W. Boehm, Chattanooga, Tennessee
James E. Butler, Washington, DC
Alan T. Collins, London, UK
Sally Eaton-Magaña, Carlsbad, California
John L. Emmett, Brush Prairie, Washington
Emmanuel Fritsch, Nantes, France
Eloïse Gaillou, Paris, France
Al Gilbertson, Carlsbad, California
Gaston Giuliani, Nancy, France
Lee A. Groat, Vancouver, Canada
Yunbin Guan, Pasadena, California
Peter Heaney, University Park, Pennsylvania
Richard W. Hughes, Bangkok, Thailand
Jaroslav Hyršl, Prague, Czech Republic
Dorrit Jacob, Canberra, Australia
A.J.A. (Bram) Janse, Perth, Australia
Mary L. Johnson, San Diego, California
Stefanos Karampelas, Paris, France
Lore Kiefert, Lucerne, Switzerland
Simon Lawson, Maidenhead, UK
Ren Lu, Wuhan, China
Thomas M. Moses, New York, New York
Laura Otter, Canberra, Australia
Aaron Palke, Carlsbad, California
Ilene Reinitz, Chicago, Illinois
Nathan Renfro, Carlsbad, California
Benjamin Rondeau, Nantes, France
George R. Rossman, Pasadena, California
Sudarat Saeseaw, Bangkok, Thailand
Karl Schmetzer, Petershausen, Germany
Andy Shen, Wuhan, China
Guanghai Shi, Beijing, China
James E. Shigley, Carlsbad, California
Elisabeth Strack, Hamburg, Germany
Nicholas Sturman, Bangkok, Thailand
D. Brian Thompson, Florence, Alabama
Fanus Viljoen, Johannesburg, South Africa
Wuyi Wang, New York, New York
Christopher M. Welbourn, Reading, UK
Chunhui Zhou, New York, New York
J.C. (Hanco) Zwaan, Leiden, The Netherlands

GEMS & GEMOLOGY

gia.edu/gems-gemology

Subscriptions
Copies of the current issue may be purchased for $29.95 plus shipping. Subscriptions are $79.99 for one year (4 issues) in the U.S. and $99.99 elsewhere. Canadian subscribers should add GST. Discounts are available for renewals, group subscriptions, GIA alumni, and current GIA students. To purchase print subscriptions, visit store.gia.edu or contact Customer Service. For institutional rates, contact Customer Service.

Database Coverage
Gems & Gemology's impact factor is 0.767, according to the 2019 Thomson Reuters Journal Citation Reports (issued July 2020). *G&G* is abstracted in Thomson Reuters products (Current Contents: Physical, Chemical & Earth Sciences and Science Citation Index—Expanded, including the Web of Knowledge) and other databases. For a complete list of sources abstracting *G&G*, go to gia.edu/gems-gemology, and click on "Publication Information."

Manuscript Submissions
Gems & Gemology, a peer-reviewed journal, welcomes the submission of articles on all aspects of the field. Please see the Author Guidelines at gia.edu/gems-gemology or contact the Managing Editor. Letters on articles published in *G&G* are also welcome. Please note that Field Reports, Lab Notes, Gem News International, Micro-World, Diamonds from the Deep, and Charts are not peer-reviewed sections but do undergo technical and editorial review.

Copyright and Reprint Permission
Abstracting is permitted with credit to the source. Libraries are permitted to photocopy beyond the limits of U.S. copyright law for private use of patrons. Instructors are permitted to reproduce isolated articles and photographs/images owned by *G&G* for noncommercial classroom use without fee. Use of photographs/images under copyright by external parties is prohibited without the express permission of the photographer or owner of the image, as listed in the credits. For other copying, reprint, or republication permission, please contact the Managing Editor.

Gems & Gemology is published quarterly by the Gemological Institute of America, a nonprofit educational organization for the gem and jewelry industry.

Postmaster: Return undeliverable copies of *Gems & Gemology* to GIA, The Robert Mouawad Campus, 5345 Armada Drive, Carlsbad, CA 92008.

Our Canadian goods and service registration number is 126142892RT.

Any opinions expressed in signed articles are understood to be opinions of the authors and not of the publisher.

About the Cover

The internal structures of natural pearls from the marine mollusk Pinctada maxima *are the subject of the lead article in this issue. The scattered loose pearls on the cover are from Paspaley's natural pearl collection, which includes one discovered in the 1970s at the Eighty Mile Beach fishing grounds. Courtesy of Paspaley Pearls Pty Ltd.*

Printing is by L+L Printers, Carlsbad, CA.

GIA World Headquarters The Robert Mouawad Campus 5345 Armada Drive Carlsbad, CA 92008 USA

© 2021 Gemological Institute of America All rights reserved.

ISSN 0016-626X

FSC www.fsc.org MIX Paper from responsible sources FSC® C006300

Internal Structures of Natural Pearls from *Pinctada maxima*, Identification of Resin-Filled Turquoise, Spinel Inclusions Chart, and More.....

Spring ushers in a feeling of renewal, and as we start to slowly recover from the global pandemic, it is a welcome sentiment. Join us as we investigate the inner structures of natural *Pinctada maxima* pearls, the technical evolution of turquoise treatments using resin filling, and a mathematical approach to predicting color in uniaxial gemstones. Even though the Tucson gem shows were canceled this February, we are able to offer more than 20 pages of captivating interviews covering how many in the trade have been weathering the situation along the entire supply chain.

"A mathematical method using visible spectroscopy to accurately predict color, the most important quality for a colored gemstone..."

Natural *Pinctada maxima* pearls take center stage in the lead article as Artitaya Homkrajae and fellow GIA researchers conduct a detailed analysis of 774 natural pearls collected from wild marine mollusks. These pearls were classified into six broad internal structural types based on X-ray techniques such as real-time microradiography (RTX) and X-ray computed microtomography (μ-CT). The results of this work support the efforts to aid in the dependable identification of natural versus cultured pearls by gemological laboratories.

In the second article, Ling Liu and a team from the Gemmological Institute, China University of Geosciences in Wuhan use ultraviolet fluorescence, spectrofluorometry, and Fourier-transform infrared (FTIR) spectrometry to characterize resin-filled turquoise. Their research addresses an urgent need to detect the prevalence and constantly evolving treatment techniques applied to turquoise sourced from China's Hubei Province.

Next, Che Shen and coauthors provide a mathematical method using visible spectroscopy to accurately predict color, the most important quality for a colored gemstone, and guidance on cutting backed by science. This comprehensive study predicts the color of a uniaxial gem when viewed in any direction by reconstructing unpolarized spectra provided the polarized spectra and relative viewing angle to the c-axis are known.

In our last article, Nathan Renfro and coauthors present a beautiful array of inclusions in natural, treated, and synthetic spinel, as well as inclusions of spinel in other gemstones. Their colorful spinel inclusions chart is enclosed with every printed copy of this issue. Laminated versions of it, along with the five inclusion charts, are also available at store.gia.edu.

As always, interesting gemological findings abound in our regular sections. Discover natural diamonds displaying asterism and bicolor rough diamond crystals featuring distinct colorless and pink areas in *Lab Notes*, while *Micro-World* delights with a glimpse into the inner landscapes of gems: a kaleidoscopic play of interference colors seen in thin-film fluid inclusions in aquamarine and a cloud inclusion shaped like a diamond profile mimicking its diamond host. The *Gem News International* section features a virtual report on the pandemic's impact and how the trade adapted their business practices to continue to flourish, as well as the headline-grabbing Cookie Monster geode and a glance back in time at hand-drilled holes in diamond briolettes. This issue also contains the annual *G&G* Challenge, where you can test your gemological knowledge of our 2020 issues. Finally, be sure to see our announcement of the Dr. Edward J. Gübelin Most Valuable Article Award winners.

We hope you enjoy the Spring 2021 edition of *Gems & Gemology*!

Duncan Pay | Editor-in-Chief | dpay@gia.edu

Internal Structures of Known *Pinctada maxima* Pearls: Natural Pearls from Wild Marine Mollusks

Artitaya Homkrajae, Areeya Manustrong, Nanthaporn Nilpetploy, Nicholas Sturman, Kwanreun Lawanwong, and Promlikit Kessrapong

Natural pearls form in mollusks without any human assistance, whereas cultured pearls form as a result of human intervention. In general practice, the identification of natural versus cultured pearls is determined by the internal structure revealed by X-ray techniques, particularly real-time microradiography (RTX) and X-ray computed microtomography (µ-CT). Interpretation of the results is based on reference samples studied previously. Therefore, a reference database founded on reliable samples obtained directly from known sources is an important factor. The internal structures of 774 natural marine pearls collected in situ by two of the authors from freshly opened wild *Pinctada maxima* mollusks were studied in detail to gain a better understanding of the internal structural characteristics of natural *P. maxima* pearls. Based on the internal features obtained from RTX and µ-CT analyses, the samples were classified into six broad growth structure types: (1) tight or minimal growth, (2) organic-rich concentric, (3) dense core, (4) void, (5) linear, and (6) miscellaneous structures. Tight or minimal growth structures are typically observed in natural pearls and was noted in the majority of these samples. Some exhibited particular forms of organic-rich concentric, void, or linear structures resembling those previously observed and reported in some non-bead cultured (NBC) pearls produced from the same mollusk species. Such overlapping features demonstrate the challenges of distinguishing some natural and NBC pearls submitted to gemological laboratories. This article will present the diverse range of internal features found in natural *P. maxima* pearls, discuss the complexities sometimes encountered during the identification process, and share the protocols GIA applies in such situations. The work strengthens GIA's reference collection database on the internal structures of pearls, supporting its goal of providing dependable results on pearls submitted by clients. In this context, the authors intend to conduct further studies on natural and cultured pearls of known origins from various environments and mollusks to make GIA's database even more comprehensive.

Pearls are biogenic gem materials that may form naturally without human intervention, or with assistance from humans in a culturing process. Natural and cultured pearls often display similar external appearances and occasionally cannot be differentiated without examining their internal structures. Over the last century, scientists and gemological laboratories have used film X-radiography and digital real-time microradiography (RTX) to reveal these interior growth patterns (Alexander, 1941; Webster, 1950; Benson, 1951; Sturman, 2009; Scarratt and Karampelas, 2020). Around 2010, X-ray computed microtomography (µ-CT) began to be applied to pearl testing. This application provides high-resolution 3D imaging of the morphological structures, allowing fine growth features to be viewed in greater detail compared to traditional X-radiography (Karampelas et al., 2010; Krzemnicki et al., 2010; Otter et al., 2014; Karampelas et al., 2017). RTX and µ-CT are the main techniques used today by GIA and other gemological laboratories for pearl identification.

As with most research, interpretation of the results is based on data collected over the years, as well as the experience of those performing the work. Thus, a sample's source or the way in which it was obtained are very important factors to consider when creating a reliable database (Pardieu and Rakotosaona, 2012; Vertriest et al., 2019). In accordance with its existing guidelines for collecting gemstone reference samples

See end of article for About the Authors and Acknowledgments.
Gems & Gemology, Vol. 57, No. 1, pp. 2–21,
http://dx.doi.org/10.5741/GEMS.57.1.2
© 2021 Gemological Institute of America

TABLE 1. GIA pearl sample classification codes.

		Origin
A-type: Collected in the field by a GIA gemologist diving to collect the shell at the source/farm		Known sample
A1	Collected in situ directly from a freshly opened mollusk (video and/or photo record available).	
A2	Collected from a freshly opened mollusk. However, unable to document where the pearl formed because it fell out of the pearl sac during the opening process.	
A3	Collected from the bottom of a container after the mollusk's soft tissues have passed through a mechanical separator.	
B-type: Collected in the field by a diver/operator witnessed by a GIA gemologist at the source/farm		Known sample
B1	Collected in situ directly from a freshly opened mollusk (video and/or photo record available).	
B2	Collected from a freshly opened mollusk. However, unable to document where the pearl formed because it fell out of the pearl sac during the opening process.	
B3	Collected from the bottom of a container after the mollusk's soft tissues have passed through a mechanical separator.	
C-type: Collected from a trusted source (pearl diver/farmer/manufacturer/dealer)		Reported sample
C1	Bought/loaned/donated from a trusted source (diver, farmer, etc.) in the local market (close to the source) with supporting information on sample origin.	
C2	Bought/loaned/donated from a trusted source (diver, farmer, etc.) in the international market with supporting information on sample origin.	
D-type: Collected from an unknown source or unfamiliar dealers/suppliers/farmers		Reported sample
D1	Bought/loaned/donated from unknown source in the local market (close to the source) with supporting information on sample origin.	
D2	Bought/loaned/donated from unknown source in the international market with supporting information on sample origin.	
E-type: No information about how the pearl was collected		Unknown sample
E1	Bought/loaned/donated from an unknown or unfamiliar source, but lacking any records/documents on sample origin.	

in the field, GIA has applied pearl sample classification codes reflecting the different degrees of origin dependability (table 1). Those listed as A-type samples are the most dependable, while E-type samples are the least dependable. Collecting pearls directly from freshly opened mollusks is the ideal situation (A and B type), but this is not always possible, especially when it comes to natural pearls. In many cases, research can only be carried out on samples purchased or loaned from pearl farmers or reputable dealers (C and D type). These samples are often described as being "reportedly" from a source or mollusk, and in most cases they serve as useful references in pearl identification matters. However, there are occasions where these reported samples are not sufficiently dependable to reach confident determinations, and more reliable reference samples are needed. E samples lack specific origin information, but can still be useful for some research such as color treatment or surface quality enhancement comparisons. A reference collection constructed of "known samples" that carefully documents how, when, and where they were acquired is an essential foundation for research on origin identification. Samples with known origin provide the highest degree of data reliability.

Pinctada maxima is a well-known mollusk species in the *Pinctada* genus, which is widely distributed throughout the central Indo-Pacific region (Southgate and Lucas, 2008). As with other mollusks, it can produce natural pearls, though it is now more

In Brief

- Pearl identification (natural vs. cultured) is dependent on the internal structure obtained by X-ray techniques, in particular RTX and μ-CT analyses.
- Interpretation of the results is based on reference samples collected over the years. Therefore, reliable samples obtained directly from known sources are critical.
- The internal structures of 774 natural marine pearls collected in situ from freshly opened wild *Pinctada maxima* mollusks were studied.
- Various forms of internal structures were observed. While the majority displayed tight or minimal growth structures, some exhibited particular forms of organic-rich concentric, void, or linear structures similar to some NBC pearls, demonstrating the challenges of pearl origin identification.

Figure 1. A map showing the location where GIA staff retrieved natural pearls produced by wild Pinctada maxima *mollusks fished from the historical beds off Eighty Mile Beach in Broome, Western Australia. Image from Google Maps.*

commonly associated with shell (mother-of-pearl) and cultured pearl production. Bead-cultured (BC) pearls are the primary product, although, some non-bead cultured (NBC) pearls are also produced as a byproduct of the culturing process. NBC pearls (sometimes referred to as "keshi") are cultured pearls that form without a bead within a cultured pearl sac, instigated by human actions (CIBJO, 2017).

While the identification of most NBC pearls is straightforward, differentiating between some natural and NBC pearls can be challenging because both types are formed almost entirely of nacre and do not contain a shell bead nucleus. The reports on *P. maxima* pearls from Western Australia (Scarratt et al., 2012) and Lombok, Indonesia (Sturman et al., 2016), are GIA's pioneering studies on pearls of known origin. The samples in both reports were classified as B-type samples since they were collected in situ from mollusks by GIA gemologists after the shells were recovered, and the information for each pearl retrieved is well documented. In each case the samples helped to promote standardized identification calls on pearls produced from *P. maxima* mollusks since there are no questions concerning their origin. For this reason, GIA intends to continue studying samples of known origin from *P. maxima* in order to expand the dependable database of internal structures for gemologists to access when needed.

The authors have studied the internal structures of three different groups of known *P. maxima* pearls, and the various growth features observed within each group will be discussed in a series of three articles. This, the first installment, looks at the natural pearls retrieved directly from unoperated wild mollusks. The second article will cover NBC and BC pearls that were grown in cultured pearl sacs that developed from pieces of mantle tissue inserted into the gonad areas. The final article will address pearls that formed in the mantle area or adductor muscle, or were attached to the shell, of operated mollusks.

Figure 2. A selection of natural P. maxima *pearls retrieved directly from the wild mollusks examined in this study, shown on a* P. maxima *shell. The largest pearl weighs 19.94 ct. Photo by Nuttapol Kitdee.*

MATERIALS AND METHODS

In late September 2013, a GIA pearl team (authors AH and AM) with the assistance of the Paspaley Pearling Company, once again had the opportunity to visit the historical *P. maxima* mollusk beds off Eighty Mile Beach in Broome, Western Australia (Scarratt et al., 2012, figure 1). Although the main purpose of the pearling expedition off Eighty Mile Beach was to collect wild *P. maxima* shells from the ocean floor as a part of the Australian shelling quota system (WAMSC, 2015), GIA's primary objective was to collect natural pearls found in the mollusks. In total, 774 natural pearls were found in 20,488 opened mollusks (figure 2), and those authors present were able to retrieve pearls and record the exact locations where 370 of them formed within the mollusk (B1 sample type).

On opening the shells, the search started with a visual inspection of the soft organs for any obvious pearls. This was followed by a fingertip search to feel for any seed pearls or pearls that might have formed

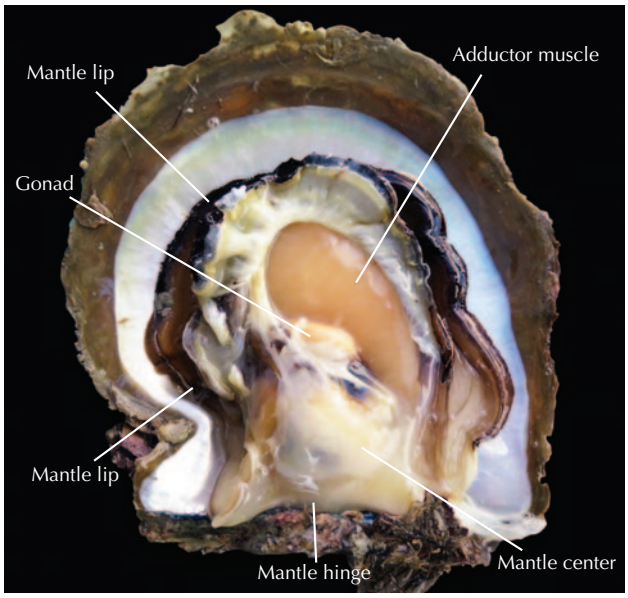

Figure 3. Searching for natural pearls in the mollusk body began with a visual inspection and then the soft organs (mantle lip, mantle hinge, mantle center, and adductor muscle) were explored with fingertips. Natural pearls were found in all areas, apart from the gonads, and some were found loosely attached to the shell surface. The mantle lip shown in the image is retracted; it originally extended to the shell's edge (ventral margin). Note: The naming convention was developed by GIA and initially presented in 2014. Photo by Nanthaporn Nilpetploy.

Figure 4. Aside from the mantle area, some seed pearls were found embedded in the adductor muscle. The pearl in the image (indicated by the white arrow) weighs 0.14 ct. Photo by Areeya Manustrong.

in areas hidden from view by the mantle that extended around the lip, down to the hinge and the central part (figure 3). The adductor muscle was also checked for the presence of pearls. The majority of pearls retrieved from the known positions were found in various parts of the mantle, either close to the lip, toward the hinge or in the central part of the mollusk (table 2). However, it was very interesting to see that some seed pearls were also found embedded in the adductor muscles (figure 4). As would be expected for natural wild shells, no pearls were found in the gonads. Moreover, a few were loosely attached to the shell surface, and were subsequently removed by applying gentle finger pressure. The latter are considered to be whole pearls and typically show circular marks of organic-rich material on their surface where they were connected to the shell (Lawanwong et al., 2019). These findings are in keeping with the observations from Australian fisheries recorded by Kunz and Stevenson (1908):

> Within the adductor muscle are found seed-pearls and small baroque; the large pearls are found embedded in the mantle, where their presence may be detected as soon as the shell is opened, the pearly gleam contrasting with the light blue of the mantle. Sometimes, though rarely, large pearls are found loose within the shell, whence they roll out when the shell is opened.

It came as no surprise that some specimens did not produce any pearls, while others contained more than one pearl. More commonly, pearls formed in individual sacs in adjacent areas (figure 5, left) or in separate areas within the mollusk, though in some cases several individual pearls formed within the same sac (figure 5, right).

Shell opening was carried out over eight days by several people on the vessel. The exact position in which some of the remaining 404 pearls formed inside the mollusks could not be documented because they fell out of the sac during the shell opening process (B2 sample type). This could have resulted

TABLE 2. Natural *P. maxima* pearl samples examined in this study.

Position where found in the mollusk	Mantle	Adductor muscle	Attached to shell	Unknown	Total
Number of pearls	217	138	15	404	774

Figure 5. Pearls were commonly found in individual sacs in adjacent areas or in separate areas within the mollusk (left). However, some individual natural pearls were found together in the same pearl sac (right). Photos by Artitaya Homkrajae.

from the abrupt retraction of the mantle lip from the shell edge (ventral margin) when cutting through the mollusk or from the perforation of the pearl sac by a knife. The balance of the 404 pearls were recovered later in the process from the bottom of a container after the mollusks' soft tissues had passed through a mechanical separator (B3 sample type). Nonetheless, all the samples studied are undoubtedly classified as natural pearls of known origin, as they formed in wild mollusks (i.e., unbred, non-hatchery raised, unoperated) that had never been involved in any pearl culturing process. The measurements ranged from 0.49 mm to 16.16 × 15.57 × 13.24 mm, and the weights ranged from negligible to 19.94 ct.

The internal structures of the 774 natural marine pearl samples, on loan to GIA, were recorded using RTX and µ-CT analyses. The RTX analysis was performed using a Pacific X-ray Imaging (PXI) GenX-90P X-ray system with 4-micron microfocus, 90 kV voltage, and 0.16 mA current X-ray source with an exposure time of 200–400 milliseconds per frame, combined with a PerkinElmer 1512 flat panel detector with a maximum of 128 frames average and 74.8 micropixel pitch with 1944 × 1536 pixel resolution. The samples that showed intriguing or indistinct structures were selected for more detailed µ-CT work to better view the internal structures. The µ-CT work was carried out with a ProCon CT-mini X-ray system with a 5-micron microfocus, 90 kV voltage, and 0.18 mA X-ray current source. Two detectors with a frame grabber card were used to capture the results: a Hamamatsu flat panel detector C7921CA-29 with 50 micropixel pitch and 1032 × 1032 pixel resolution, and a Varex 1207 flat panel detector with 74.8 micropixel pitch and 1536 × 864 pixel resolution. RTX and µ-CT data were collected in GIA's Bangkok laboratory. Because the work focused on the samples' internal structures, other aspects including physical, spectroscopic, and chemical characteristics are not presented.

OBSERVATIONS AND RESULTS

A natural pearl is the result of an accidental occurrence during the normal life cycle of a mollusk (Strack, 2006). Various conditions influence the formation of pearls, such as water environment and a mollusk's health (Gervis and Sims, 1992; Bondad-Reantaso et al., 2007), so it is common to find various types of internal structures in natural pearls, as well as cultured pearls. Based on the internal features obtained by RTX and µ-CT analyses, natural pearl samples can be separated into six broad growth structure types (figure 6):

1. Tight or minimal growth
2. Organic-rich concentric
3. Dense core
4. Void
5. Linear
6. Miscellaneous

From all 774 natural pearls examined in this study, 45 were selected in order to provide a representative overview of the various internal structures observed. The RTX and µ-CT results of each sample are shown in tables 3 through 8, along with the sample number, weight, and measurement in the first column and a macro image in the third column. The second column shows the image captured during each pearl's retrieval, if applicable, from within the mollusk. The position of each pearl is indicated by a black arrow and noted in the first column. Those listed as "unknown" were the ones where the pearl's position could not be documented because it fell out of the pearl sac during the opening process or was later recovered from the mechanical separator. The RTX and µ-CT results are grayscale images in which differing shades of bright and dark grayscale intensity correspond to X-ray density (i.e., the different degrees of attenuation the component materials have to X-rays). Mineralized materials such as arag-

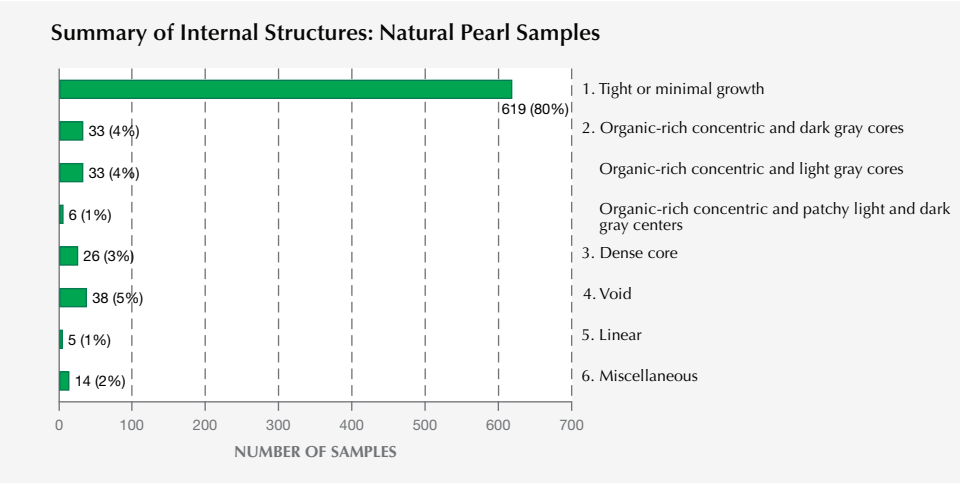

Figure 6. Summary of the six internal structures found in the 774 natural pearl samples studied, with the percentage of each structure type within the group.

onite or calcite are denser or more radiopaque than organic-rich features or voids filled with gases and/or liquid; hence, an area composed entirely of aragonite will appear lighter than an area containing organic-rich or void features which generally appear darker (Wehrmeister et al., 2008; Sturman, 2009; Otter et al., 2014). *[Note: In this article, the description of an internal structure as "dark gray" and "light gray" corresponds to its X-ray density, not its actual color.]*

TABLE 3. Examples of natural pearls from wild mollusks with tight or minimal growth structures (type 1).

Sample details	Position where found in the mollusk	Macro image	RTX image	µ-CT image
1-1 (mantle hinge) 1.45 ct 6.71 x 5.62 mm				
1-2 (mantle hinge) 0.65 ct 4.85 x 4.57 x 5.89 mm				
1-3 (adductor muscle) 0.30 ct 3.98 x 3.71 x 3.00 mm				
1-4 (mantle hinge) 0.63 ct 6.33 x 4.25 x 3.10 mm				

The position of the pearl in the mollusk is indicated by a black arrow. The white arrows indicate the more radiopaque (lighter gray) areas observed.

TABLE 4. Examples of natural pearls from wild mollusks with organic-rich concentric structures (type 2).

Sample details	Position where found in the mollusk	Macro image	RTX image	µ-CT image
Dark gray core				
2-1 (mantle lip) 2.20 ct 8.29 x 6.80 x 6.22 mm	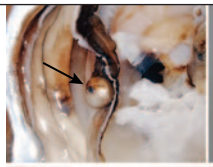		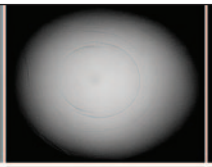	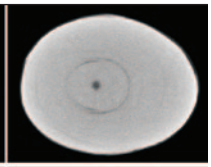
2-2 (attached to shell) 19.94 ct 16.23 x 15.65 x 13.21 mm			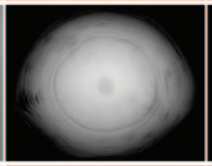	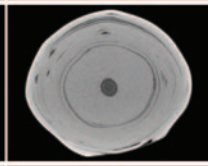
2-3 (mantle lip) 1.38 ct 6.40 x 5.89 x 5.78 mm	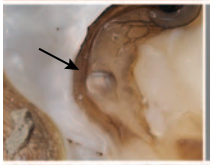		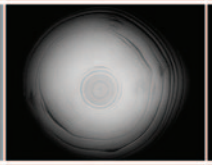	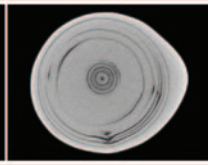
2-4 (mantle center) 0.37 ct 4.05 x 3.84 x 3.55 mm			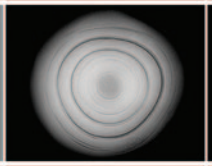	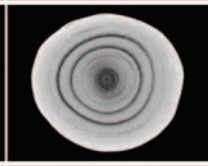
2-5 (mantle lip) 0.74 ct 5.17 x 4.60 mm			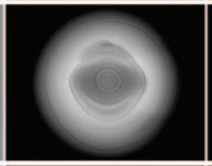	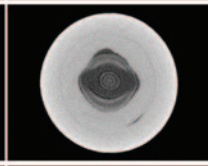
2-6 0.45 ct 4.14 x 3.76 mm	Unknown		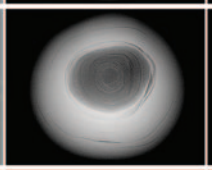	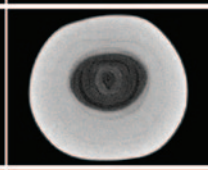
2-7 (mantle lip) 0.39 ct 4.31 x 3.93 x 3.07 mm			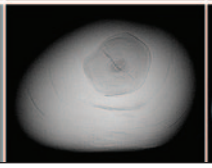	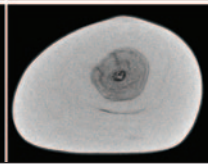
Light gray core				
2-8 0.59 ct 4.45 mm	Unknown		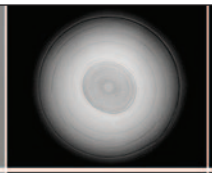	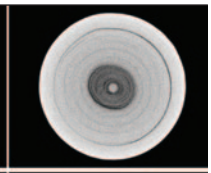
2-9 0.30 ct 3.93 x 3.73 x 2.78 mm	Unknown		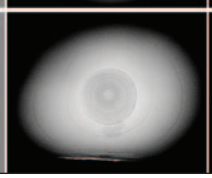	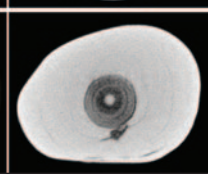

The position of the pearl in the mollusk is indicated by a black arrow.

TABLE 4 (continued)

Sample details	Position where found in the mollusk	Macro image	RTX image	µ-CT image
		Light gray core		
2-10 0.17 ct 3.44 x 2.88 x 2.63 mm	Unknown		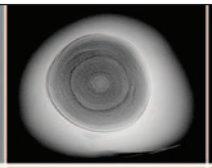	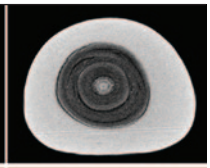
2-11 0.14 ct 2.82 mm	Unknown	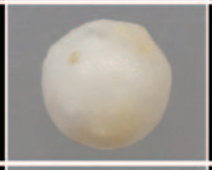	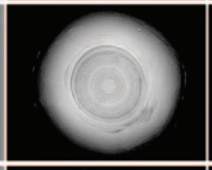	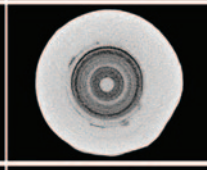
2-12 0.34 ct 3.79 x 3.65 x 3.41 mm	Unknown	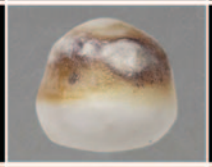	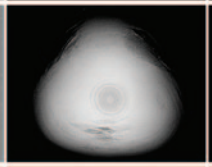	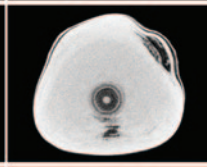
2-13 0.37 ct 3.90 x 3.65 mm	Unknown		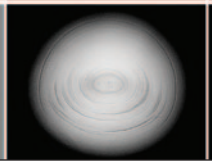	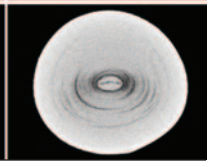
		Patchy light and dark gray centers		
2-14 (mantle center) 1.10 ct 6.20 x 5.68 x 4.60 mm		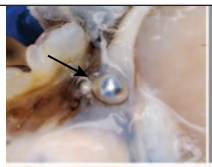		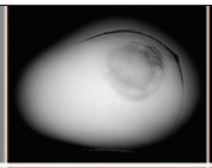
2-15 (mantle center) 0.12 ct 2.92 x 2.05 mm		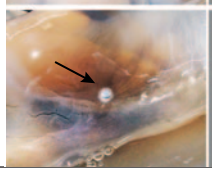		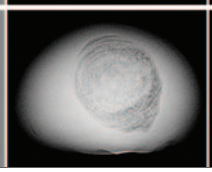

The position of the pearl in the mollusk is indicated by a black arrow.

Type 1: Tight or Minimal Growth Structures. 619 samples (~80%) recovered displayed this structure. They lacked any clear internal growth structures, or only showed a few weak growth patterns (fine structural curved lines correlating with the pearl's shape) by RTX analysis (table 3). The majority of the pearls also revealed very little structure when examined by µ-CT analysis. In addition, slightly lighter gray (more radiopaque) areas were observed in some instances, as shown in samples 1-2 and 1-3 (indicated by white arrows). These areas may be composed of some material or substance that has a higher X-ray density than nacre. Since the pearls did not contain questionable internal features related to any type of cultured pearl formation, they would, in almost all cases, be identified as natural pearls.

Type 2: Organic-Rich Concentric Structures. Around 9% of the samples in this study displayed organic-rich concentric structures of various sizes and patterns (table 4). They ranged from examples with a very small core (sample 2-1) to those with large concentric layered areas occupying almost half of the pearl's interior (sample 2-10). µ-CT analysis clearly revealed cores with different forms, such as a dark gray core (more radiolucent), a light gray core (more radiopaque), or varying degrees of contrast with patchy light and dark gray centers within the con-

centric structures. The dark gray cores are not empty spaces, but rather they are filled with a solid/semi-solid organic-rich phase (samples 2-1 to 2-7). The sizes of the dark gray cores varied from small spots to large irregular areas shown in samples 2-6 and 2-7. The light gray cores appeared to be dense material and had a radiopacity similar to that of the outer nacre; hence, they are probably $CaCO_3$. These cores varied in size, with the majority of them appearing small and rounded, as shown in samples 2-8 to 2-12. Sometimes the shape and structures varied, as in sample 2-13, which showed an ovoid core and a linear-appearing feature running across its center (magnified in figure 7). The structure of sample 2-13 was inconsistent with the majority of pearls in the group; it has never been observed in known or "reportedly" natural samples in our experience and has not been noted in the literature. This unusual structure may be challenging to identify, especially in laboratory conditions when information on the pearl's origin is unknown, and therefore greater care is needed in its interpretation. It could easily be misidentified as a NBC pearl since the majority of light gray cores observed in natural pearls are typically rounded, and off-round cores have been observed in known NBC pearls produced by the *P. maxima* mollusk (Manustrong et al., 2019). Moreover, the central feature within the core has a linear form, and such features have been observed in NBC pearls produced by various mollusk species. Similar linear features, although not exactly the same, are often considered sufficient evidence to classify pearls as NBC (Hänni, 2006; Sturman, 2009; Krzemnicki et al., 2010; Sturman et al., 2016; Nilpetploy et al., 2018a; Manustrong, 2018). RTX and µ-CT imaging of samples 2-14 and 2-15 showed patchy concentric structures that appeared neither light nor dark gray, and these were due in part to differences in the organic content within the areas. These samples also lacked dark or light gray cores.

Type 3: Dense Core Structures. A small portion, approximately 3% of the group, contained solid light gray (more radiopaque) core features, usually single but sometimes multiple, at their centers (table 5). The X-ray attenuation of these cores closely matched some similar features observed in type 2 samples. However, they were not enclosed by clear organic-rich concentric structures; hence, they were classified as a separate structural type, referred to here as a "dense core." These dense cores usually appeared as a single structure that was round, off-round, or irregularly shaped, and they were often associated with some faint organic-rich layers (samples 3-1 to 3-3). A few examples, such as samples 3-4 and 3-5, showed two or more cores that formed together as multi-nuclei. Irregular dense core structures have only been observed in natural pearls, in the authors' experience, and have not been reported in any NBC pearls. However, an off-round feature associated with the main core in sample 3-5 looks suspicious and could be construed as being a light gray $CaCO_3$ "seed" feature sometimes found in NBC pearls (Krzemnicki et al., 2010, 2011; Nilpetploy et al., 2018a; Manustrong et al., 2019). Thus, if this pearl was tested without any supporting provenance, it could be interpreted as being NBC. Nevertheless, the greater detail revealed by µ-CT analysis showed faint growth layers inside the feature, in contrast to the $CaCO_3$ "seed" features,

Figure 7. µ-CT slices in three directions of sample 2-13 revealed an ovoid core and a linear-looking feature running through the center. Based on these two features, the pearl could possibly be misidentified as NBC if it were submitted for testing without any supporting information about its origin.

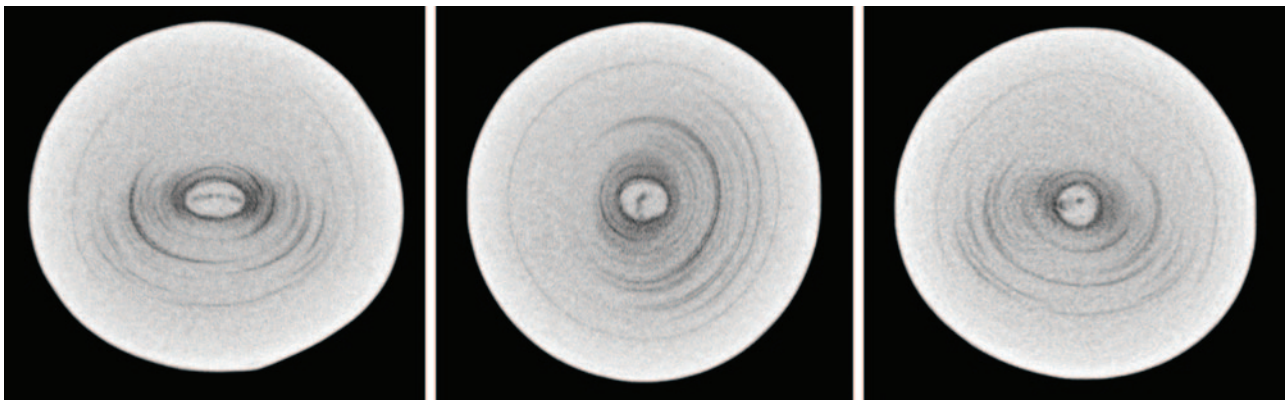

TABLE 5. Examples of natural pearls from wild mollusks with dense core structures (type 3).

Sample details	Position where found in the mollusk	Macro image	RTX image	µ-CT image
3-1 0.19 ct 3.37 x 2.97 x 2.42 mm	Unknown	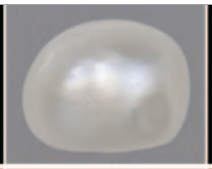	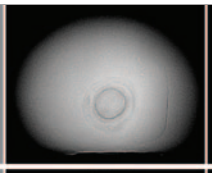	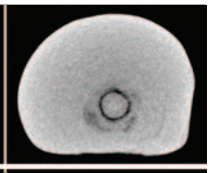
3-2 0.14 ct 2.85 x 2.68 x 2.57 mm	Unknown		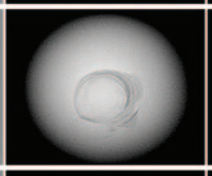	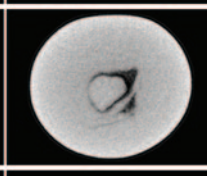
3-3 (mantle hinge) 0.50 ct 5.92 x 3.46 x 3.22 mm			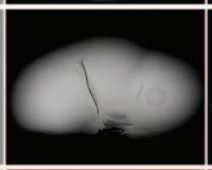	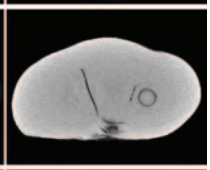
3-4 1.55 ct 7.02 x 5.79 x 5.60 mm	Unknown		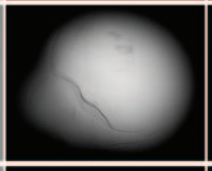	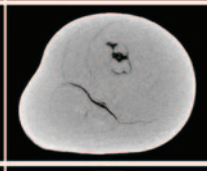
3-5 (mantle hinge) 0.13 ct 2.86 x 2.76 x 2.38 mm	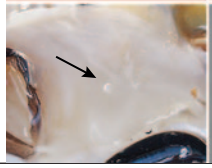		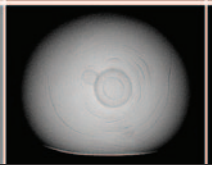	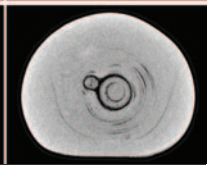

The position of the pearl in the mollusk is indicated by a black arrow.

which are usually tight and contain no structure (magnified in figure 8). In this example, where the internal structural characteristics overlap and do not correspond with the majority of structures observed

Figure 8. µ-CT slices in three directions of sample 3-5 revealed a satellite off-round feature next to the main core. The feature has similarities to light gray $CaCO_3$ "seed" features observed within some NBC pearls. However, it revealed faint growth structure within, which is rare to see in the $CaCO_3$ seeds observed in NBC pearls. The overlapping characteristics do not correspond with the majority of structures observed in natural and NBC pearls, which could create some doubts about the identification of this pearl, leading to an inconclusive result. The circular feature in the image on the right is an artifact and should be ignored.

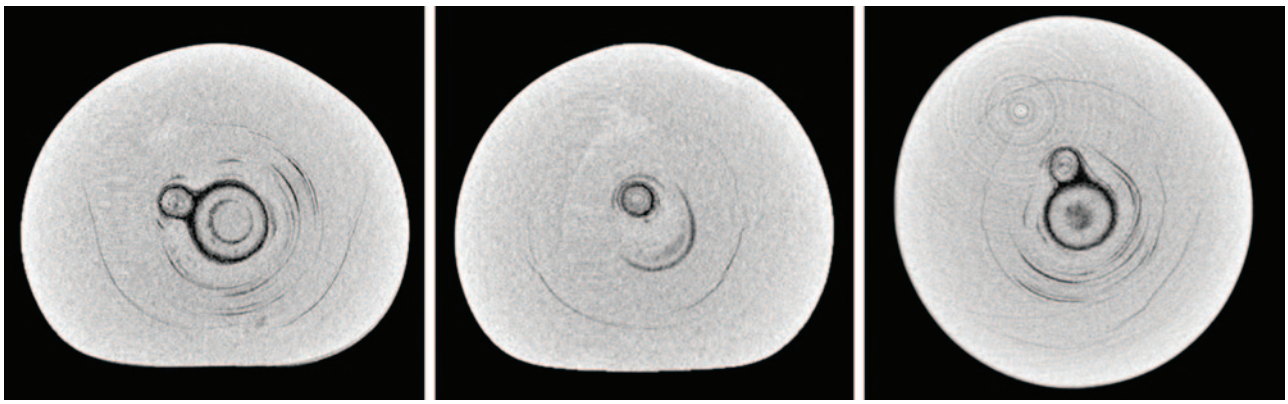

TABLE 6. Examples of natural pearls from wild mollusks with void structures (type 4).

Sample details	Position where found in the mollusk	Macro image	RTX image	µ-CT image
4-1 (mantle lip) 0.93 ct 5.99 x 4.52 x 4.38 mm			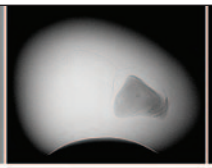	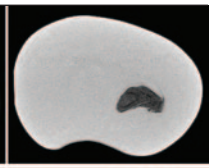
4-2 (mantle lip) 1.13 ct 5.75 x 5.69 x 1.53 mm	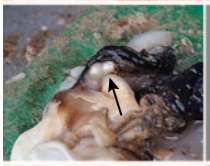		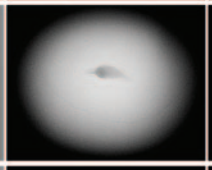	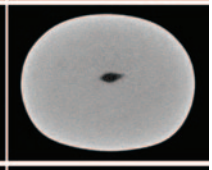
4-3 (mantle lip) 0.28 ct 4.09 x 3.61 x 2.56 mm	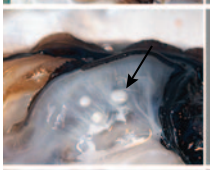		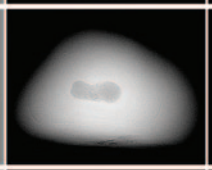	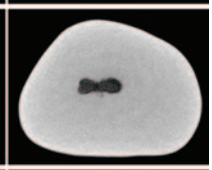
4-4 (mantle lip) 0.09 ct 2.63 x 2.50 x 1.90 mm	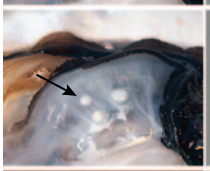		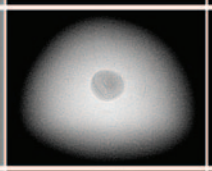	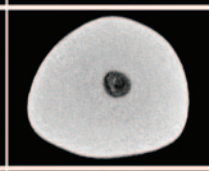
4-5 1.04 ct 5.64 x 5.06 x 4.96 mm	Unknown		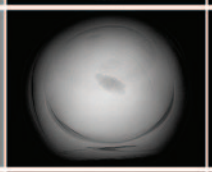	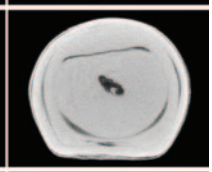
4-6 (mantle center) 2.65 ct 10.07 x 8.41 x 4.58 mm	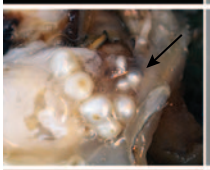		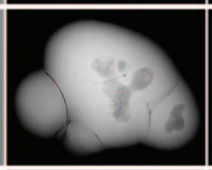	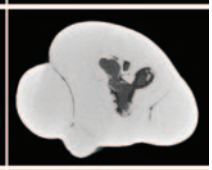
4-7 0.21 ct 3.40 x 3.18 x 2.71 mm	Unknown		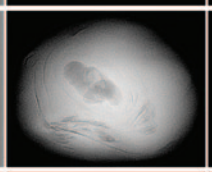	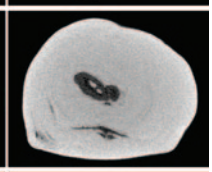
4-8 0.22 ct 3.55 x 3.09 x 2.63 mm	Unknown		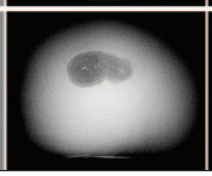	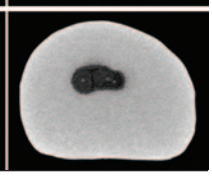

The position of the pearl in the mollusk is indicated by a black arrow.

in natural and NBC pearls, an inconclusive opinion may well result.

Type 4: Void Structures. When discussing the internal characteristics of pearls, *voids* usually refer to radiolucent features that are less dense or more transparent to X-rays, such as cavities or areas filled with gas and/or liquid phases. Voids generally appear as various shades of dark gray, and thus they may resemble organic-rich features in low-resolution X-ray images. Voids are commonly observed in saltwater NBC pearls, especially pearls from *Pinctada* species

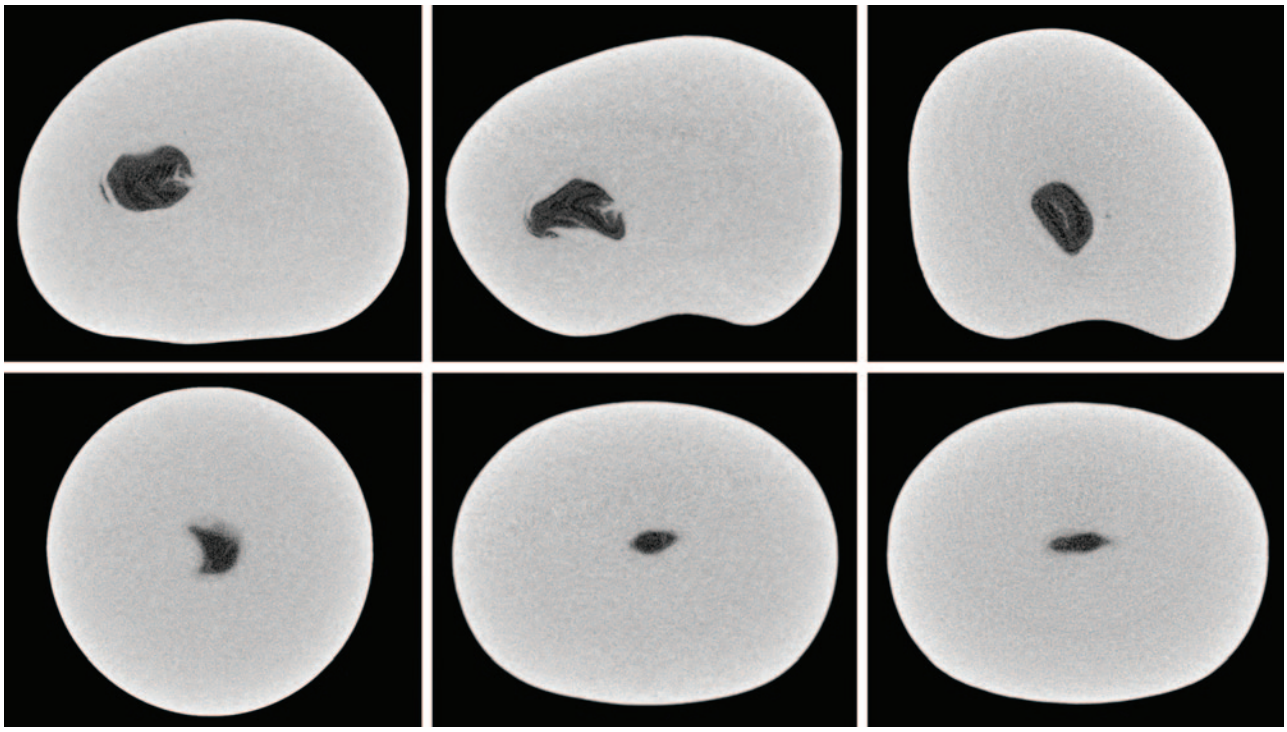

Figure 9. µ-CT slices in three directions of samples 4-1 (top row) and 4-2 (bottom row) revealed a void feature in both. The void of sample 4-1 is filled by organic-rich features more consistent with voids found in natural pearls, whereas the void in sample 4-2 looks empty even though there are actually a few very small light gray features. The structure of 4-2 appears more NBC in nature than its twin retrieved from the pearl sac, even though it is a known natural pearl.

(Wehrmeister et al., 2008; Sturman, 2009; Krzemnicki et al., 2010; Otter et al., 2014; Sturman et al., 2016; Nilpetploy et al., 2018a; Manustrong, 2018; Al-Alawi et al., 2020). In many cases, voids are a key identification feature by which to differentiate NBC from natural pearls. Only ~5% of the group showed void-related characteristics, and most of these exhibited centrally positioned irregular void-like forms after RTX analysis (table 6). However, µ-CT analysis revealed that many of these voids were filled with fine organic-rich growth features (samples 4-1 and 4-3 to 4-6), and some showed small light gray features in the center of organic-rich structures (samples 4-7 and 4-8) rather than the apparently empty spaces usually observed in NBC pearls. The voids are also small relative to the size of the pearl, while those found in saltwater NBC pearls tend to be larger and more elongated, extended lengthwise, usually taking up more than half of the pearl's length.

While natural voids do show some differences from those encountered in NBC pearls, identification challenges could cause some pearls to be misidentified. A couple of samples in this study showed voids similar to those characteristically found in NBC pearls, and they would almost certainly be classified as NBC if tested under blind conditions. It is interesting to note that samples 4-1 and 4-2 were retrieved from the same pearl sac and both possessed void features. However, the void in sample 4-2 does not appear to be filled with organic-rich growth structure and contains fewer light gray linear features, a common observation in NBC pearls (magnified in figure 9).

Type 5: Linear Structures. Most linear structures are thin voids, with or without organic-rich material partially filling them. Owing to the different appearances of both types of formation, they are separated into different groups in this article. Linear structures have been regarded as characteristic of NBC pearls from both saltwater and freshwater environments (Scarratt et al., 2000; Sturman, 2009; Krzemnicki et al., 2010; Sturman et al., 2016; Nilpetploy et al., 2018a; Manustrong, 2018; Al-Alawi et al., 2020).

Interestingly, 5 of the 774 natural pearl samples also displayed linear structures (table 7). Sample 5-1

TABLE 7. Examples of natural pearls from wild mollusks with linear structures (type 5).

Sample details	Position where found in the mollusk	Macro image	RTX image	µ-CT image
5-1 (mantle lip) 1.14 ct 6.75 x 5.37 x 4.51 mm	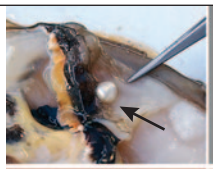	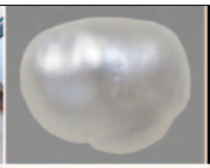	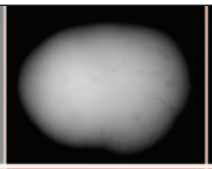	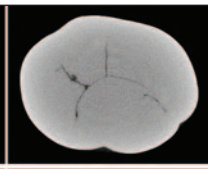
5-2 1.61 ct 9.50 x 5.42 x 4.58 mm	Unknown		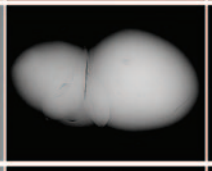	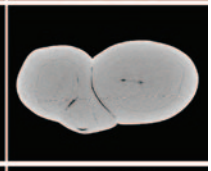
5-3 (mantle lip) 2.03 ct 7.38 x 6.85 x 5.73 mm	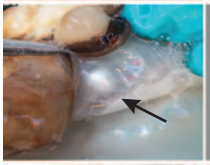		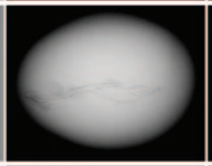	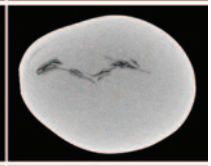
5-4 (mantle lip) 0.26 ct 4.91 x 3.91 x 2.66 mm	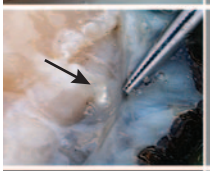		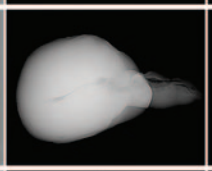	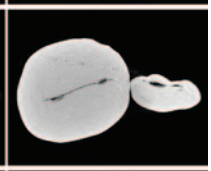
5-5 0.24 ct 3.57 x 3.00 mm	Unknown		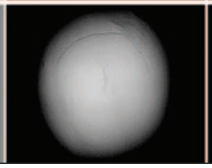	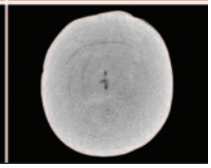

The positions of the pearl in the mollusk is indicated by a black arrow.

showed a complex linear feature corresponding, to some degree, with the pearl's baroque outline. In the authors' experience, such linear structures may be characteristic of NBC pearls, but this example demonstrates that is not always the case. Sample 5-2 consisted of three portions, two of them having a

Figure 10. µ-CT slices in three directions of sample 5-2 revealed a long linear structure in the center of both parts of the pearl. These linear features could lead to it being misidentified as a NBC pearl, despite the associated growth patterns also present. The circular feature in the image on the right is an artifact and should be ignored.

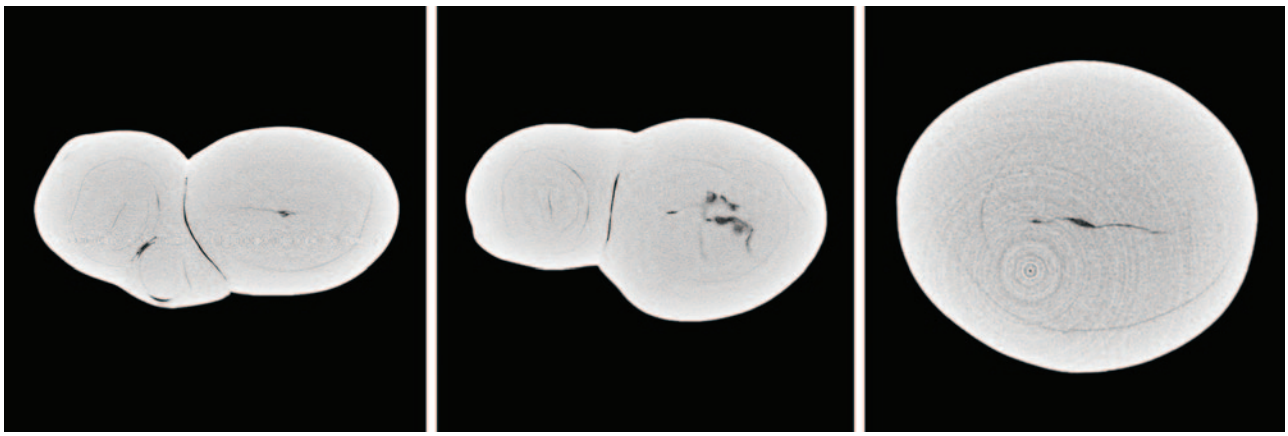

TABLE 8. Examples of natural pearls from wild mollusks with miscellaneous structures (type 6).

Sample details	Position where found in the mollusk	Macro image	RTX image	µ-CT image
Marine organisms				
6-1 1.22 ct 6.02 x 5.73 x 5.43 mm	Unknown		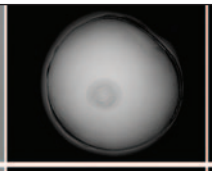	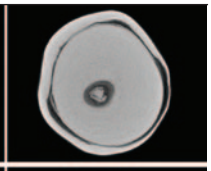
6-2 0.26 ct 3.70 x 3.02 x 2.84 mm	Unknown		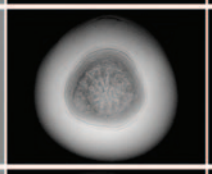	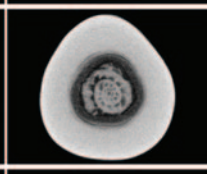
6-3 0.22 ct 3.56 x 3.07 x 2.63 mm	Unknown		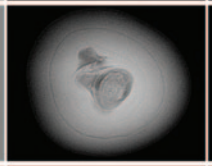	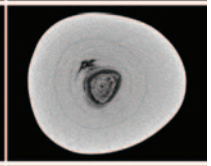
6-4 0.13 ct 3.02 x 2.79 x 2.26 mm	Unknown		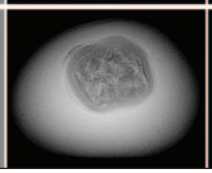	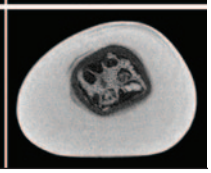
Internal fractures				
6-5 (attached to shell) 0.54 ct 4.66 x 4.41 x 3.71 mm	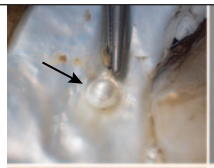		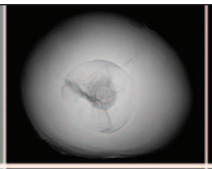	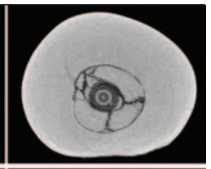
6-6 0.57 ct 5.56 x 4.24 x 3.48 mm	Unknown		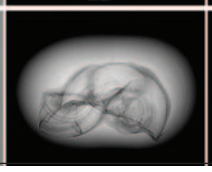	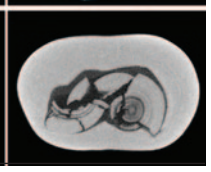
Alternate light and dark gray features				
6-7 0.21 ct 3.86 x 3.11 x 2.35 mm	Unknown		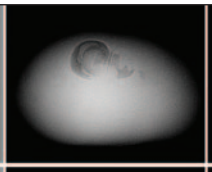	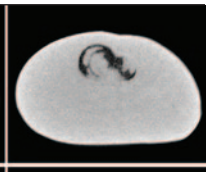
6-8 0.57 ct 6.56 x 3.70 x 3.05 mm	Unknown		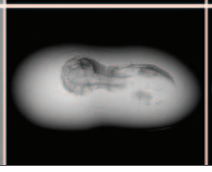	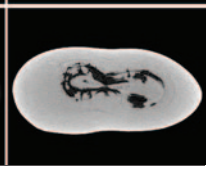

The position of the pearl in the mollusk is indicated by a black arrow.

long linear feature at the center (magnified in figure 10). Although the other portion only displayed a few growth patterns, the pearl's overall structure looked questionable and it could easily be misidentified as an NBC pearl. The linear structures revealed in samples 5-3 to 5-5 are quite distinct and correspond with the length of the pearl, a characteristic shown by many NBC pearls.

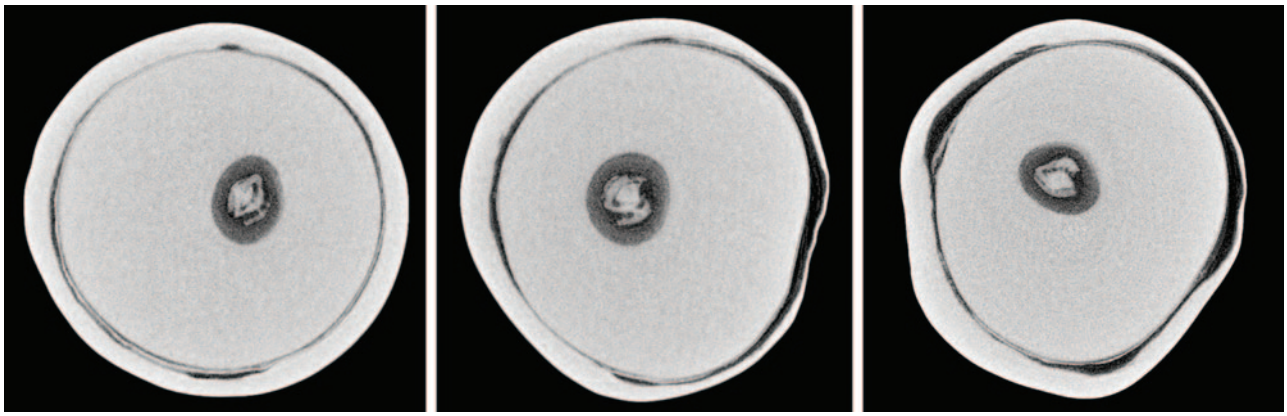

Figure 11. µ-CT slices in three directions of sample 6-1 revealed a shell-like formation at its core, probably enclosed by organic-rich material. A prominent outer ring is visible in all directions, which makes the pearl look questionable. As a result, it could be misidentified as an atypical bead cultured pearl (aBCP).

Type 6: Miscellaneous Structures. The final group of natural pearls were classified as those with "miscellaneous structures." This group includes samples possibly containing marine organisms entombed by nacre deposition, examples containing obvious internal fractures, and pearls exhibiting a mixture of structures that do not readily fit into any of the former five structure types listed (table 8).

Pearls with internal features that appear to be related to marine organisms are very rare, and only a few have been encountered in the GIA laboratory from the thousands of natural pearls submitted for identification and research. Some examples have been documented in the existing literature (Scarratt et al., 2012; Nilpetploy [nee Somsa-ard], 2015). Even so, the authors were surprised to find four samples in this study group with what are most likely marine organism features. Samples 6-1 to 6-3 revealed shell-like features at their center that likely initiated the formation of the pearls, together with displaced epithelial cells. The features measured 0.78 × 0.70 mm, 1.46 × 1.34 mm, and 0.72 × 0.50 mm in diameter, respectively. The resulting pearls are similarly small. The exact identity of the marine organisms is unknown; based on the morphology observed by µ-CT analysis, however, they could be one of the many benthic foraminifera species. Foraminifera are single-celled organisms (protists) with a test (shell) that can possess one or more chambers (Borrelli et al., 2018). They may be composed of organic compounds, sand grains, or other particles cemented together, or crystalline $CaCO_3$, and are usually less than 1 mm in size (Steele et al., 2001). One of the existing references (Nilpetploy [nee Somsa-ard], 2015) described what was thought to be an intricate foraminifera sphere observed in a 0.95 ct natural pearl. The core feature was encircled by a dark organic-rich area and accompanying void similar to the natural pearls described here. Sample 6-1 (magnified in figure 11) has a distinct outer ring that looks questionable and could be considered diagnostic of an atypical bead cultured pearl (aBCP), but it does not contain an "organic tail" typ-

Figure 12. µ-CT slices in three directions of sample 6-4 revealed a porous-looking structure in the main feature, possibly resembling the structure of coral from the Melithaea *genus, a fan coral distributed throughout the tropical Indo-Pacific region.*

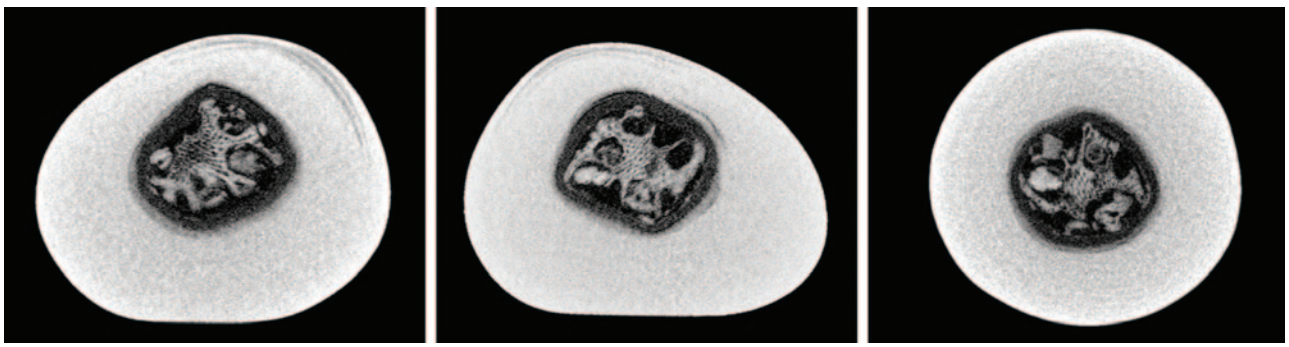

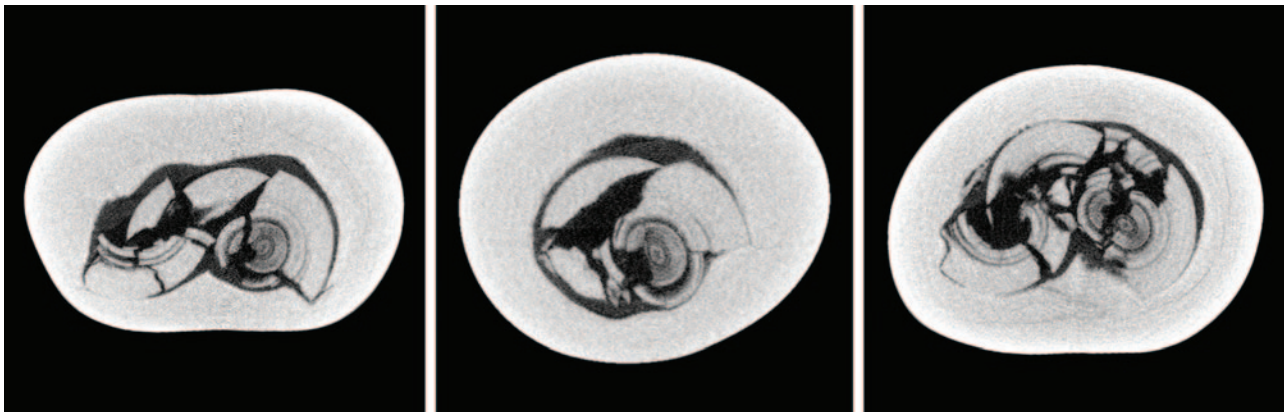

Figure 13. µ-CT slices in three directions of sample 6-6 revealed fragmented organic-rich concentric structure in the center of the pearl.

ically observed in aBCP pearls (Hänni et al., 2010; Scarratt et al., 2017; Kessrapong and Lawanwong, 2020). Therefore, it would be identified as a natural pearl, especially when its size and quality are also taken into account. Sample 6-4 displayed a large irregular radiopaque material together with some small fragments at its center. As the magnified images in figure 12 show, the material's structure differs from the three former samples, though its appearance is also likely that of a marine organism. The main feature, with its porous-looking pattern, bears some similarity to the structure of *Melithaea*, a genus of colonial soft coral (also known as fan coral), which is distributed throughout the tropical Indo-Pacific region (Jeong et al., 2018; Atlas of Living Australia, 2020).

Samples 6-5 and 6-6 displayed severe internal fracturing at the center of the features. X-ray computed tomography clearly revealed the intriguing structures of both pearls and indicated they were "fragmented." It is puzzling how such broken features can exist within known natural pearls whose overlying layers of nacre appear intact and where no drilling or external treatment of any kind exist. Sample 6-6 is especially perplexing, as the naturally formed concentric organic-rich inner structure has disintegrated into many parts (magnified in figure 13) to fill the void present. This intricate structure is highly unusual, and it would be challenging to correctly identify such a pearl in laboratory testing conditions. Some of these samples could be suspected of being the result of culturing using various atypical nuclei. Yet their generally very small size would suggest otherwise, and it is known that this is definitely not the case, as they are confirmed natural pearls.

Samples 6-7 and 6-8 revealed a mixture of structures alternating between more radiopaque (light gray) and more radiolucent (dark gray) features. The structure exhibited in sample 6-7 (magnified in figure 14) appears to take the form of two initiation features

Figure 14. µ-CT slices in three directions of sample 6-7 revealed two interconnected rounded initiation features in the center. The central areas in both features consist of material with the same radiopacity as the pearl's body. No characteristic NBC cultured pearl features, such as a void or linear structure, were noted. Therefore, the pearl would be classified as natural.

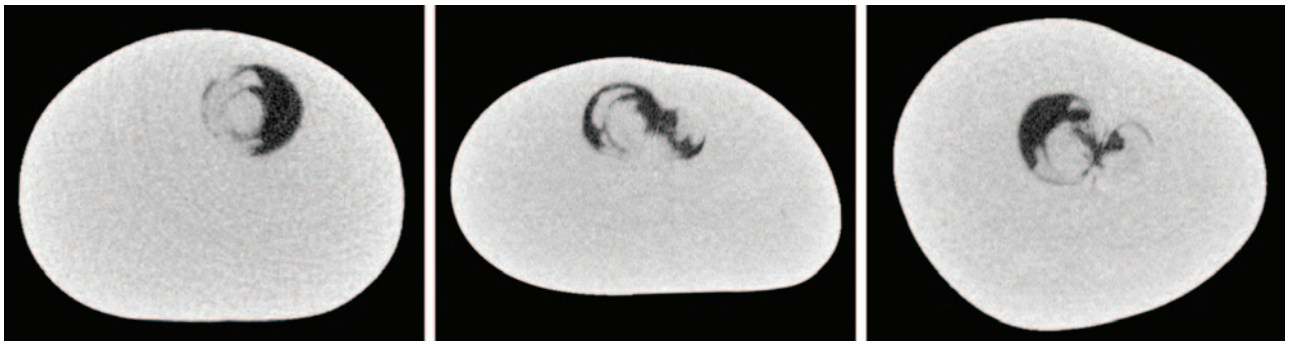

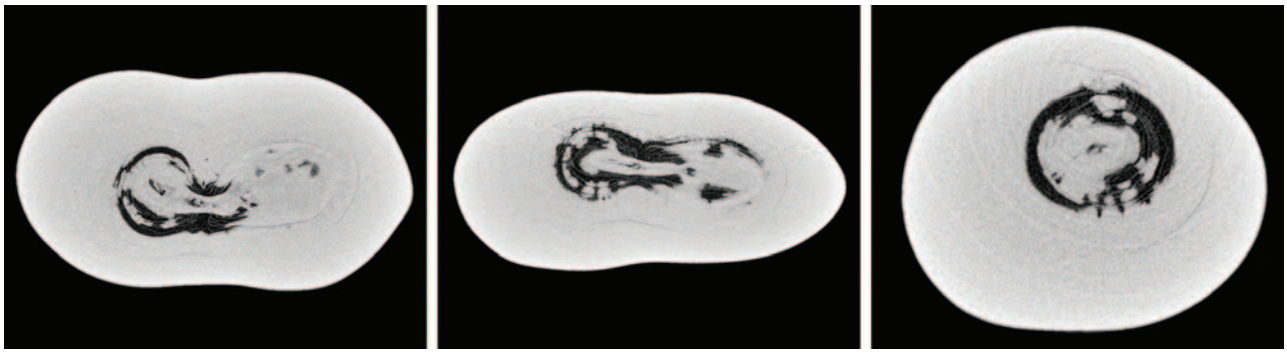

Figure 15. µ-CT slices in three directions of sample 6-8 revealed a complex elongated structure consisting of a linear-like feature at its center combined with dark gray areas of voids and organic matter, and other solid light gray areas. A similar structure has been observed in some known NBC pearl samples; therefore, the identification of this pearl is challenging, and it is highly possible it would be misidentified as NBC.

merging together. Although the structure is unusual, this sample would almost certainly be identified as a natural pearl since there are no characteristic cultured pearl features such as a void or a linear structure in the center. On the other hand, sample 6-8 (magnified in figure 15) displayed a complex elongated structure consisting of a linear-like feature at its center combined with dark gray areas of voids and organic matter, as well as other solid light gray areas. Such a structure looks suspicious, and in laboratory conditions the pearl could be misidentified as NBC.

DISCUSSION

Pearl identification mainly involves separating pearls that formed naturally (figure 16) from those that resulted from a culturing process. RTX is the primary technique used in gemological laboratories to examine a pearl's internal structure, while µ-CT is a high-resolution 3D imaging technique that is sometimes used to visualize internal structures in greater detail. Interpreting the structural results obtained depends on the research and data collection of known reference samples by well-trained, experienced gemologists. Studying this large group of natural pearls provided a greater understanding about the range of microradiographic structures encountered in natural pearls produced by wild *P. maxima* mollusks. The results showed that most of the natural pearl samples (~80%) exhibited tight or minimal growth structures (type 1). These pearls are straightforward to identify as natural. This observation is also consistent with the majority of natural pearls tested in all GIA's pearl testing locations. Tight or minimal growth structure is commonly observed in natural pearls produced by many mollusk species of both nacreous and non-nacreous pearls (Krzemnicki et al., 2010; Scarratt et al., 2012; Karampelas, 2017; Nilpetploy et al., 2018b; Scarratt and Hänni, 2004; Wing Yan Ho and Zhou, 2014; Wing Yan Ho, 2015; Wing Yan Ho and Yazawa, 2017).

Organic-rich concentric structures (type 2) are also known to be typical of natural pearls produced by various mollusk species (Krzemnicki et al., 2010, Scarratt et al., 2012; Sturman et al., 2014; Karampelas et al., 2017; Nilpetploy et al., 2018b), yet they were found in only about ~9% of the samples. This includes organic-rich concentric and dark gray (radiolucent) cores that are filled with organic-rich features (~4%), organic-rich concentric and light gray (more radiopaque) cores in which the majority of the cores are small and rounded (~4%), and organic-rich concentric and patchy light and dark gray structures lacking dark and light gray cores (~1%) (see figure 6). Most of the organic-rich concentric areas observed in natural pearls cover a relatively small portion of the pearl's interior. It is important to note that none of the pearls in this study showed any of the light gray $CaCO_3$ "seed" features reported by Manustrong et al. (2019; see tables 4 and 5) and previously reported by other authors (Krzemnicki et al., 2010, 2011; Nilpetploy et al., 2018a) as being associated with organic-rich concentric structures in some cultured pearls. At the time of this report, the irregular dense core structures (type 3) free of any clear organic-rich concentric features are only found in natural pearls and have not been reported in NBC pearls in the literature.

Voids (type 4) and linear structures (type 5) have been reported as characteristic features in *P. maxima* NBC pearls (Sturman et al., 2016), but they were found in only ~5% and ~1%, respectively, of the natural pearl

Figure 16. This 19.94 ct pearl is the largest from the collection of 774 natural pearls collected off Eighty Mile Beach in Broome, Western Australia. The pearl was loosely attached to the shell and removed by gentle finger pressure. Photo by Areeya Manustrong.

samples in this study. Considering that the internal structural features of natural and NBC pearls may overlap, the separation between the two can be challenging and their interpretation requires extra care. While the pearls' external appearance may also assist in their identification, it is a subjective element and can vary greatly depending on the gemologist's experience. Therefore, the internal structures of pearls provide the most important evidence and consequently are the primary means of identification. In general, the void structures observed in the natural pearl samples studied occupy a relatively small volume of the pearl, and are often filled with organic-rich growth structures. The linear features are perhaps the most questionable structures found in natural pearls since the structure is widely accepted as being an identifying feature of NBC pearls produced by various mollusks. Therefore, it is possible that some or all of the five natural pearls that revealed linear structures would be identified as NBC if submitted on a "blind" basis.

In the miscellaneous structures (type 6), the presence of a marine organism-like feature as a nucleus in four samples emphasized a frequently applied hypothesis that a natural pearl forms when an external foreign object reaches the mollusk's mantle (epithelium layer), and causes the epithelial cells to encroach into the connective tissue and enclose the object to create a pearl sac, which secretes the necessary components (Kunz and Stevenson, 1908; Landman et al., 2001; Strack, 2006; Southgate and Lucas, 2008). However, this is a rare occurrence, as only a very small number of pearls have reportedly shown this type of structure, and there are several theories about how natural pearls may form. These include: forming as a result of injury to, or abnormal growth of the epithelium cells; epithelium cells separating to form pearl sacs of their own accord; and health-related instigation. A concept mentioned in Strack (2006) may help to explain the severe internal fracturing of the features within the centers of samples 6-5 and 6-6:

> If the worm larvae survive within the pearl sac or even within the growing pearl, they will usually attack or soften the surrounding pearl cover after a period of hibernation. This means that they can cause the growing pearl to break into tiny pieces, which may themselves become the reason for the formation of a new pearl sac, or will become the nucleus of a new pearl.

Lastly, the relationship between the internal structure and the position in which a pearl forms inside the *P. maxima* mollusk species is not entirely clear at this time. Since it was not possible to record the position in which over 50% of the samples were found in the mollusk's body, this question could not be addressed. Such a study would require a greater sample set of pearls with suitably accurate records. However, it was noted that most of the pearls found in the adductor muscles possessed tight or minimal growth structures, while mantle pearls generally showed a variety of structure types.

CONCLUSIONS

The results of this study show that various forms of internal structures are observed in natural pearls. The majority of samples revealed limited growth features (minor growth patterns) or no clear structure at all (tight structure), confirming their natural identity. The relatively few samples that exhibited varying degrees of structural overlap, internal characteristics possibly observed in NBC pearls or natural pearls (i.e., off-round light gray cores in concentric organic-rich structure, voids, and linear features), raised concerns about the identification of such pearls when tested without any supporting provenance information. They demonstrated the complexities often faced with pearl identification. It is not unheard of for the same pearl to receive different determinations from different organizations based on the equipment and techniques used to obtain the data, the experience and specialized knowledge of gemologists interpreting the data, and the comprehensiveness of the reference sample database. Natural pearls containing either a large void relative to the pearl's size or a distinct linear feature have a greater probability of being defined as NBC. In cases where the structures are extremely complex or ambiguous, or do not conform with anything in the database, an "inconclusive" call is likely. GIA recognizes the ongoing pearl identification challenges and intends to continue studying the internal structures of known natural and cultured pearl samples from various environments and mollusks to strengthen its reference collection and database, thus ensuring GIA's gemologists have the most up-to-date information at hand before reaching any conclusions on a client's pearl submissions.

ABOUT THE AUTHORS

Ms. Homkrajae is a senior staff gemologist at GIA in Carlsbad, California. Ms. Manustrong is a staff gemologist, Ms. Nilpetploy is a senior staff gemologist, Mr. Sturman is a consultant to GIA, and Ms. Lawanwong and Mr. Kessrapong are analytics technicians, all in GIA's Bangkok laboratory.

ACKNOWLEDGMENTS

The authors would like to extend their appreciation to Paspaley Pearling Company, Australia, for loaning the samples to GIA's Bangkok laboratory for this study and permitting GIA staff to visit Australia in order to retrieve the pearls in person. They also wish to thank Tom Moses and Kenneth Scarratt for their support and for making the trips to Paspaley possible. Lastly, we thank the peer reviewers for valuable and constructive comments that improved this article.

REFERENCES

Al-Alawi A., Ali Z., Rajab Z., Albedal F., Karampelas S. (2020) Saltwater cultured pearls from *Pinctada radiata* in Abu Dhabi (United Arab Emirates). *Journal of Gemmology*, Vol. 37, No. 2, pp. 164–179.

Alexander A.E. (1941) Natural and cultured pearl differentiation. *G&G*, Vol. 3, No. 12, pp. 184–188.

Atlas of Living Australia (2020) *Melithaea*. Milne-Edwards & Haime, 1857, https://bie.ala.org.au/species/urn:lsid:biodiversity.org.au:afd.taxon:8f9a2eb5-de4f-4f60-98ce-476774f63b73

Benson L.B. (1951) Gem Trade Laboratory installs new pearl testing equipment. *G&G*, Vol. 7, No. 4, pp. 107–112.

Bondad-Reantaso M.G., McGladdery S.E., Berthe F.C.J. (2007) Pearl oyster health management: A manual. FAO Fisheries technical paper, No. 503, Rome, Italy, 120 pp.

Borrelli C., Panieri G., Dahl T.M., Neufeld K. (2018) Novel biomineralization strategy in calcareous foraminifera. *Scientific Reports*, Vol. 8, No. 1, 10201.

CIBJO, the World Jewellery Confederation (2017) *The Pearl Book*. CIBJO Pearl Commission.

Gervis M.H., Sims N.A. (1992) The biology and culture of pearl oysters (Bivalvia: Pteriidae). ICLARM Studies and Reviews 21, Manila, Philippines, 49 pp.

Hänni H.A. (2006) A short review of the use of "keshi" as a term to describe pearls. *Journal of Gemmology*, Vol. 30, No. 1/2, pp. 51–58.

Hänni H.A., Krzemnicki M.S., Cartier L.E. (2010) Appearance of new bead material in cultured pearls. *Journal of Gemmology*, Vol. 32, No. 1-4, pp. 31–37.

Jeong E-A., Moon J., Hiroshi K. (2018) Akoya cultured pearls with *Corallium* species bead nuclei. *The Journal of the Gemmological Association of Hong Kong*, Vol. 39, pp. 40–44.

Karampelas S. (2017) Black non-nacreous natural pearls from *Pteria* sp. *Journal of Gemmology*, Vol. 35, No. 7, pp. 590–592.

Karampelas S., Michel J., Zheng-Cui M., Schwarz J.-O., Enzmann F., Fritsch E., Leu L., Krzemnicki M.S. (2010) X-ray computed microtomography applied to pearls: Methodology, advantages, and limitations. *G&G*, Vol. 46, No. 2, pp. 122–127, http://dx.doi.org/10.5741/GEMS.46.2.122

Karampelas S., Al-Alawi A.T., Al-Attawi A. (2017) Real-time microradiography of pearls: A comparison between detectors. *G&G*, Vol. 53, No. 4, pp. 452–456, http://dx.doi.org/10.5741/GEMS.53.4.452

Kessrapong P., Lawanwong K. (2020) Atypical bead cultured *Pinctada maxima* pearls nucleated with freshwater non-bead cultured pearls. *GIA Research News*, April 6, https://www.gia.edu/gia-news-research/atypical-bcp-nucleated-with-nbcp

Krzemnicki M., Friess D., Chalus P., Hänni H.A., Karampelas S. (2010) X-ray computed microtomography: Distinguishing natural pearls from beaded and non-beaded cultured pearls. *G&G*, Vol. 46, No. 2, pp. 128–134, http://dx.doi.org/10.5741/GEMS.46.2.128

Krzemnicki M.S., Müller, Hänni H.A., Gut H.-P., Düggelin M. (2011) Tokki pearls: Additional cultured pearls formed during pearl cultivation: External and internal structures. *32nd International Gemmological Conference*, https://www.ssef.ch/wp-content/uploads/2018/01/SSEF_Tokki_pearls.pdf
Kunz G.F., Stevenson C.H. (1908) *The Book of the Pearl*. The Century Co., New York, 548 pp.
Landman N.H., Mikkelsen P.M., Bieler R., Bronson B. (2001) *Pearls: A Natural History*. Harry N. Abrams, Inc., New York, 232 pp.
Lawanwong K., Nilpetploy N., Manustrong A., Homkrajae A. (2019) Natural shell blisters and blister pearls: What's the difference? *GIA Research News*, August 26, https://www.gia.edu/gia-news-research/natural-shell-blisters-and-blister-pearls
Manustrong A. (2018) Gems News International: Very small akoya cultured pearls. *G&G*, Vol. 54, No. 1, pp. 103–105, https://www.gia.edu/gems-gemology/spring-2018-gemnews-very-small-akoya-cultured-pearls
Manustrong A., Kessrapong P., Lawanwong K., Nilpetploy N., Homkrajae A. (2019) Known non-nacreous non-bead cultured pearls and similar unknown pearls of likely cultured origin from *Pinctada maxima*. *GIA Research News*, September 4, https://www.gia.edu/gia-news-research/known-non-nacreous-non-bead-cultured-pearls
Nilpetploy N., Lawanwong K., Kessrapong P. (2018a) Non-bead cultured pearls from *Pinctada margaritifera*. *GIA Research News*, April 27, https://www.gia.edu/ongoing-research/non-bead-cultured-pearls-from-pinctada-margaritifera
——— (2018b) The gemological characteristics of Pipi pearls reportedly from *Pinctada maculata*. *G&G*, Vol. 54, No. 4, pp. 418–427, http://dx.doi.org/10.5741/GEMS.54.4.418
Otter L.M., Wehrmeister U., Enzmann F., Wolf M., Jacob D.E. (2014) A look inside a remarkably large beaded South Sea cultured pearl. *G&G*, Vol. 50, No. 1, pp. 58–62, http://dx.doi.org/10.5741/GEMS.50.1.58
Pardieu V., Rakotosaona N. (2012) Ruby and sapphire rush near Didy, Madagascar. *GIA Research News*, October 15, https://www.gia.edu/gia-news-research-nr101512
Scarratt K., Hänni H.A. (2004) Pearls from the lion's paw scallop. *Journal of Gemmology*, Vol. 29, No. 4, pp. 193–203.
Scarratt K., Karampelas S. (2020) Pearls evolution in the sector, production and technology. *InColor*, Spring/Summer, pp. 82–86.
Scarratt K., Moses T.M., Akamatsu S. (2000) Characteristics of nuclei in Chinese freshwater cultured pearls. *G&G*, Vol. 36, No. 3, pp. 98–109, http://dx.doi.org/10.5741/GEMS.36.2.98
Scarratt K., Bracher P., Bracher M., Attawi A., Safar A., Saeseaw S., Homkrajae A., Sturman N. (2012) Natural pearls from Australian *Pinctada maxima*. *G&G*, Vol. 48, No. 4, pp. 236–261, http://dx.doi.org/10.5741/GEMS.48.4.236
Scarratt K., Sturman N., Tawfeeq A., Bracher P., Bracher M., Homkrajae A., Manustrong A., Somsa-ard N., Zhou C. (2017) Atypical "beading" in the production of cultured pearls from Australian *Pinctada maxima*. *GIA Research News*, February 13, https://www.gia.edu/gia-news-research/atypical-beading-production-cultured-pearls-australian-pinctada-maxima
Somsa-ard N. (2015) Lab Notes: A natural pearl with an intriguing internal structure. *G&G*, Vol. 51, No. 4, pp. 434–436.
Southgate P.C., Lucas J.S (2008) *The Pearl Oyster*. Elsevier, Oxford, 574 pp.
Steele J.H., Thorpe S.A., Turekian K.K. (2001) *Encyclopedia of Ocean Sciences*. Elsevier, Amsterdam.
Strack E. (2006) *Pearls*. Rühle-Diebener, Stuttgart, Germany.
Sturman N. (2009) The microradiographic structures of non-bead cultured pearls. *GIA Research News*, November 20, https://www.gia.edu/gia-news-research-NR112009
Sturman N., Homkrajae A., Manustrong A., Somsa-ard N. (2014) Observations on pearls reportedly from the Pinnidae family (Pen pearls). *G&G*, Vol. 50, No. 3, pp. 202–215, http://dx.doi.org/10.5741/GEMS.50.3.202
Sturman N., Bergman J., Poli J., Homkrajae A., Manustrong A., Somsa-ard N. (2016) Bead-cultured and non-bead-cultured pearls from Lombok, Indonesia. *G&G*, Vol. 52, No. 3, pp. 288–297, http://dx.doi.org/10.5741/GEMS.52.3.288
Vertriest W., Palke A.C., Renfro N.D. (2019) Field gemology: Building a research collection and understanding the development of gem deposits. *G&G*, Vol. 55, No. 4, pp. 490–511, http://dx.doi.org/10.5741/GEMS.55.4.490
WAMSC, Western Australian Marine Stewardship Council (2015) MSC offers a pearler of an opportunity for gem producers. Latest News, August 28, http://www.wamsc.com.au/news/mediaitem.phtml?MediaID=37
Webster R. (1950) London Laboratory's new X-ray equipment. *G&G*, Vol. 6, No. 9, pp. 279–281.
Wehrmeister U., Goetz H., Jacob D.E., Soldati A., Duschner W., Xu H., Hofmeister W. (2008) Visualization of the internal structures of cultured pearls by computerized X-ray microtomography. *Journal of Gemmology*, Vol. 31, No. 1/2, pp. 15–21.
Wing Yan Ho J. (2015) Lab Notes: Large natural quahog pearl. *G&G*, Vol. 51, No. 1, pp. 63–64.
Wing Yan Ho J., Zhou C. (2014) Lab Notes: Natural pearls reportedly from a *Spondylus* species ("thorny" oyster). *G&G*, Vol. 50, No. 3, pp. 241–242.
Wing Yan Ho J., Yazawa E. (2017) Lab Notes: Natural conch "rosebud" pearls. *G&G*, Vol. 53, No. 2, pp. 230–231.

For online access to all issues of GEMS & GEMOLOGY from 1934 to the present, visit:

gia.edu/gems-gemology

TECHNICAL EVOLUTION AND IDENTIFICATION OF RESIN-FILLED TURQUOISE

Ling Liu, Mingxing Yang, Yan Li, Jingru Di, Ruoxi Chen, Jia Liu, and Chong He

Zhushan County is the most abundant source of commercial turquoise in China's Hubei Province, where mass production has been ongoing for several decades. Chinese turquoise production and consumption have created a significant industry and promoted local economic prosperity and development. Treatment techniques for turquoise have been updated and changed rapidly, sometimes even monthly. Traditionally, rough materials are treated with resin to reduce their high porosity to improve processability, appearance, and stability. In this research, the characteristics of resin-filled turquoise were investigated by ultraviolet fluorescence, spectrofluorometry, and Fourier-transform infrared spectrometry. The differences in three-dimensional fluorescence patterns between untreated and resin-filled turquoise are reported for the first time. The three-dimensional fluorescence patterns along with the ultraviolet reactions and infrared spectra allow for the identification of this filling. Unlike untreated turquoise, the resin-filled turquoise samples had a strong and main emission peak centered at approximately 444 nm and a secondary emission shoulder at approximately 460 nm under approximately 372 nm wavelength excitation in this research. This study sheds light on resin filling processes by observing the essential features of 342 turquoise specimens after treatment. Resin filling can decrease the porosity of turquoise to improve its color and its value, and this study provides identification guidelines for gemologists and useful information on the resin-filling process.

Turquoise, a hydrated copper aluminum phosphate mineral ($CuAl_6(PO_4)_4(OH)_8 \cdot 4H_2O$), has been appreciated as a valuable gem material worldwide for thousands of years. It has a wide range of colors, such as blue, blue-green, green, yellowish green, and greenish yellow. Among these colors, blue turquoise is the most popular and sought after in the commercial market (figure 1).

In the early 1980s, many residents of Shiyan City in China's Hubei Province owned turquoise, though few were conscious of its value. The locally produced turquoise was a great bargain at about US$100–$200/kg. Moreover, small fragments were even used there as outdoor decorative materials in the 1980s (figure 2). In 2009, the local government suddenly realized the significance of its turquoise resources and started to manage mining. Since then, prices have soared because of limited turquoise resources and regulation of mining.

Generally, the portion of rough turquoise suitable for processing into fashioned gemstones is much less than 5% of the mined total. Most natural turquoise contains fissures, pores, matrix, or other defects (figure 3, left and center). Much of the porous turquoise (figure 3, right) is termed "pale" or "chalky." This ma-

In Brief

- High-quality natural turquoise is in high demand in the commercial market. Various advanced treatment techniques are performed on this material due to its intrinsic porosity. The ability to detect and identify treated turquoise is urgently needed because of the prevalence of constantly evolving treatment techniques in the marketplace.
- In this research, resin-filled turquoise displayed strong signals under long-wave ultraviolet radiation, as well as three-dimensional fluorescence patterns and infrared spectra associated with resin. Spectrofluorometry is a newly employed nondestructive technique for routine identification of turquoise treatment.
- Turquoise with pale to moderate color can show dramatic improvement in appearance and stability after pore filling treatment. Turquoise porosity drastically decreases when pores are filled with resin, thereby improving its appearance.

See end of article for About the Authors and Acknowledgments.
GEMS & GEMOLOGY, Vol. 57, No. 1, pp. 22–35,
http://dx.doi.org/10.5741/GEMS.57.1.22
© 2021 Gemological Institute of America

Figure 1. A necklace with inlaid blue turquoise (5–12 mm in length) and a turquoise sculpture (100 mm in height). The sculpture on the right was photographed at the Tiangong Award exhibition. Photos by Mingxing Yang.

terial's low hardness makes it unsuitable for processing, and it is often accompanied by low color saturation and numerous micrometer- to nanometer-sized pores. With daily wear, the color and luster of turquoise may change gradually from prolonged absorption of sweat and skin oil. Nevertheless, many Chinese turquoise enthusiasts and collectors are passionate about its natural appearance and variations.

As a porous cryptocrystalline aggregate, rough turquoise has been subjected to filling treatment to make it easier to process and improve its appearance and stability (Koivula et al., 1992; Choudhary, 2010; McClure et al., 2010). Filling treatment has been performed on a variety of low-quality gemstones with pores, fractures, or fissures. Examples include opal (Gambhir, 2001; Filin and Puzynin, 2009; Hu et al.,

Figure 2. Turquoise fragments (0.2 × 0.2 cm to 1.0 × 1.3 cm) were used as outdoor decorative materials in the 1980s in Yun County, Hubei Province. Photos by Ling Liu.

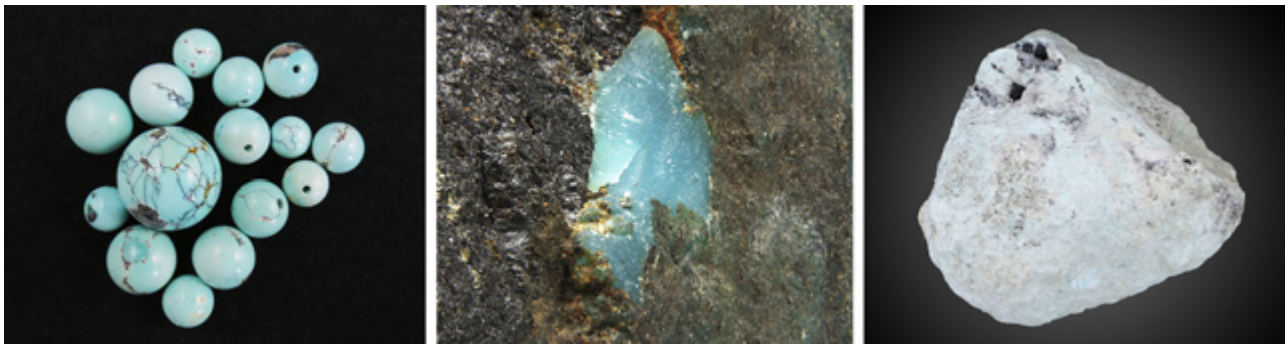

Figure 3. Left: Turquoise with fissures and pores (22.7 g total). Center: Turquoise surrounded by matrix (field of view 7.4 mm). Right: "Pale" or "chalky" turquoise (298 g). Photos by Ling Liu.

2013), tourmaline (Deng et al., 2009), emerald (Kammerling et al., 1991; Johnson et al., 1999; Johnson, 2007), and ruby ("GAAJ Lab Alert," 2004; McClure et al., 2006).

In China, conventional pore fillers used for turquoise are wax and resin. The appearance and durability of "pale" or "chalky" turquoise can be greatly improved by pore filling to decrease its porosity (figure 4). Using this technique, porous material can be fully optimized to increase its value. Occasionally, however, treated turquoise products are unfavorable due to the material's uneven hardness. The resin agent permeates and infiltrates porous areas much more easily than the compact portion. Consequently, the porous portions develop a more saturated color than the compact portion after resin treatment. As a result, the resin-treated turquoise displays a mottled appearance with obvious and artificial boundaries after polishing (figure 5). Resin filling of material sold in China should be noted in a turquoise identification report according to the Chinese national testing standard.

Turquoise can also be impregnated with a mixture of resin, hardener, and colorant. However, such

Figure 4. A bracelet and necklace set with treated turquoise (37.17 g total). Photo by Ling Liu.

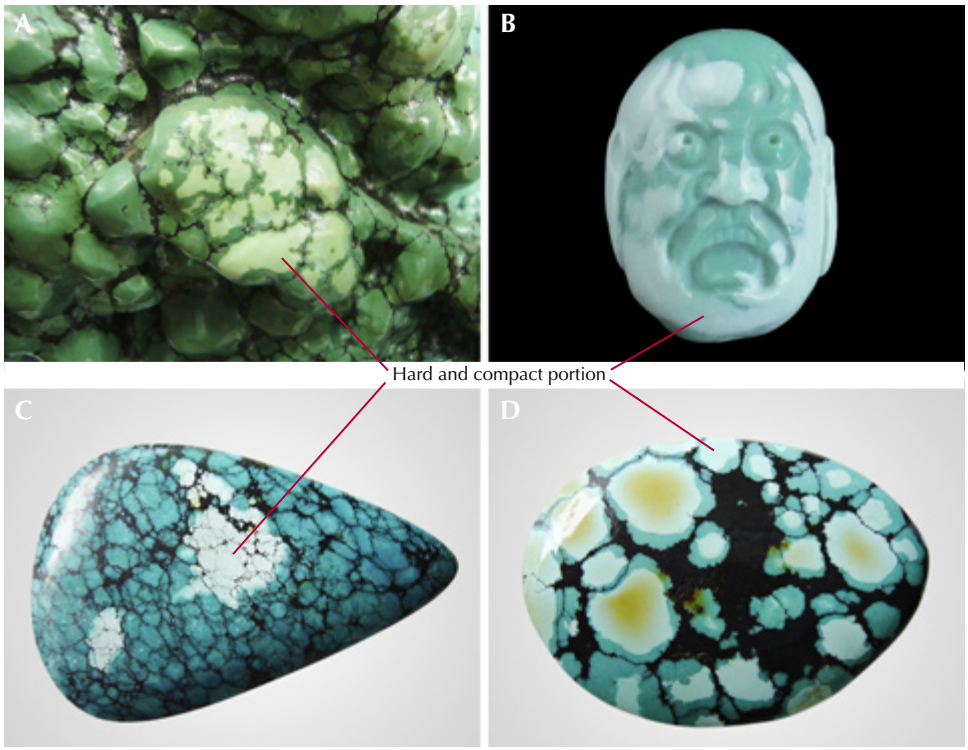

Figure 5. Turquoise with an unsatisfactory appearance after resin filling treatment. A: Close-up of a large ornament (field of view 90 mm). B: A carved ornament (3 g). C and D: Two pendants (60 and 50 mm in length, respectively). The lighter-colored portions are harder and more compact than the deeply colored portions before treatment, and therefore the resin treatment does not easily penetrate them. The artificial color boundaries generated during resin filling become obvious after polishing. Photos by Mingxing Yang and Ling Liu.

impregnation and dyeing treatment is unacceptable in the Chinese commercial trade. Additionally, the "Zachery" treatment developed in the United States can be applied to improve the color and polish of turquoise, which was first reported by *G&G* in 1999 (Fritsch et al., 1999). However, the specific equipment and agents used in the Zachery technique remain proprietary, and so far it has not been widely used in Hubei Province. Although Chinese manufacturers were initially unsure how this treatment works, they have tried to master the technology and succeeded in developing an electrochemical method (similar to the Zachery technique) to optimize not only blue turquoise, but also yellow and green materials. The thicker treated layer and saturated color produced by this electrochemical method are a significant improvement (Lin et al., 2019; Shen et al., 2018). Moreover, oiling is also widely applied to turquoise in the Chinese market today (Koivula et al., 1992; Hu et al., 2019). For a glossary of turquoise enhancement terminology, see box A.

Researchers have devoted great effort to the identification of treated turquoise, as well as various kinds of fillers such as resin, polymer, oil, plastic, and dyed substances (Lind et al., 1983; Chen et al., 2006; Moe et al., 2007; Chen et al., 2010a; Choudhary, 2010; McClure et al., 2010; Han et al., 2015; Bernardino et al., 2016; Zuo et al., 2017; Xu and Di, 2018; Hu et al., 2019; Liu et al., 2019; Xu and Yang, 2019). The treated examples mentioned above can be easily identified by different testing techniques, such as Raman and IR spectroscopy (Henn and Milisenda, 2005; Chen et al., 2006; Moe et al., 2007; Zuo et al., 2017), UV-Vis spectrophotometry (Han et al., 2015), energy-dispersive X-ray fluorescence (EDXRF; Fritsch et al., 1999), and pyrolysis–gas chromatography–mass spectrometry (Py-GC-MS; Schwarzinger and Schwarzinger, 2017). An intense band at ~1730 cm^{-1} is detected in the IR spectra of most organic-treated turquoise (i.e., polymer, plastic, or resin), which is assigned to the C=O stretching vibration. Elevated potassium is detectable exclusively in Zachery-treated turquoise (Fritsch et al., 1999).

The usual analytical techniques, such as IR spectroscopy, are sensitive to organic compounds. Counterfeiters have cunningly applied new inorganic substances to achieve superior color, luster, texture, and porcelain-like quality to pass inspection and cater to consumer demand for high-quality turquoise. More recently, many new approaches to turquoise treatment have emerged in the market using various inorganic fillers, such as aluminum dihydrogen phosphate (Zhou and Yuan, 2008; Chen et al., 2010b) and sodium silicate (also called "glass resin") (Deng et al., 2019). Few characteristic absorptions assignable to these fillers can be found in IR

BOX A: TERMINOLOGY OF TURQUOISE TREATMENT TECHNIQUES

Waxing: Turquoise (generally fashioned turquoise) is immersed in wax to coat its surface to enhance durability and appearance and prevent discoloration over time. This treatment is accepted in the trade.

Oiling: Turquoise is treated for several days or weeks by various types of oil (e.g., mineral or vegetable oil), which acts as a concealer and filler to hide superficial flaws (such as white spots) and decrease porosity for better color, appearance, and stability.

Dyeing: Turquoise is colored by various dyes or colored substances.

Resin filling: Under ambient conditions, resin and hardener are introduced into the pores of the turquoise to obtain a more stable material for processability and durability. With filling of the pores, the color of the turquoise improves because there is less light scattering.

Resin impregnation: Turquoise is impregnated with a combination of resin and hardener. The resulting altered color is dull and saturated. This process is different from resin filling. Both vacuum and pressure conditions are applied in the impregnation process but not in resin filling.

Resin impregnation and dyeing: Colorants are added and mixed with the resin and hardener. This treatment process is also performed under vacuum as well as pressure conditions, similar to resin impregnation.

Porcelain enhancement: A popular treatment technique that decreases the porosity of turquoise and improves the compactness, hardness, and luster without the use of organic polymers. Typically, this treatment involves filling turquoise with aluminum dihydrogen phosphate or sodium silicate. If turquoise is treated with phosphate substances, colorant could have been added if deemed necessary. If treated with sodium silicate, however, there is no addition of colorant.

Zachery treatment: Turquoise is treated with a potassium-containing compound for better stability and appearance. Its name refers to entrepreneurial electrical engineer James E. Zachery, who invented this process in the late 1980s (Fritsch et al., 1999).

Electrochemical method: Rough or fashioned turquoise is treated with electrolytes (usually containing potassium) based on electrochemical fundamentals (similar to the Zachery technique). The treated turquoise can achieve more saturated color not only on the surface but throughout the entire sample (Lin et al., 2019; Shen et al., 2018).

Yellow/black-fading: Turquoise is treated with chemical agents to get rid of black or yellow stain-like colors.

spectra and X-ray diffraction patterns, although scanning electron microscopy (SEM) is capable of revealing the anomalous structural characteristics of turquoise treated with aluminum phosphate adhesive (Zhou and Yuan, 2008; Chen et al., 2010b). Furthermore, some special chemical agents are used to get rid of black or yellow stain-like colors. Industry sources call this technique "yellow/black-fading" treatment and claim these stained turquoise materials can display the desired blue color after processing. Further investigation is necessary for this new treatment. Because treatment techniques have evolved so rapidly in China, their identification remains a great challenge. Some fillers are difficult to detect, and turquoise treated with inorganic substances exhibits nondescript reactions to routine and nondestructive examinations.

The pores of untreated and electrochemical-treated turquoise have been quantitatively analyzed in previous reports with the gas adsorption method and the X-ray micro-CT 3D imaging technique (Li et al., 2016; Lu et al., 2020). However, few reports have directly revealed the differences in characteristics and porosity between untreated and resin-filled turquoise (Liu et al., 2019; Xu and Yang, 2019).

This research systematically reports on resin filling techniques and the characteristics used to identify them. It also provides new insight into turquoise pores, as well as variations in the distinct features of untreated and resin-filled turquoise, namely their color and porosity. Additionally, this research aims to demonstrate the influence of pore filling on turquoise durability and appearance. The results provide valuable guidelines for detection and treatment.

MATERIALS AND METHODS

Samples. Turquoise specimens were prepared by different methods and labeled as group A, B, or C. Samples in group A and those in group C from a rough sample were provided by local dealers. Group B samples were purchased from a local dealer.

Group A. A set of 342 pieces of turquoise with various colors, sizes, and shapes were treated with resin and hardener in three different factories located in Zhushan County. Prior to filling, the samples were opaque, with

Figure 6. Left: A porous and chalky rough turquoise sample (group C) from Zhushan County (100–150 mm in diameter). Right: The mixed resin/hardener agents used for filling, offered by Bu Tian Sheng Yu Turquoise Co. Ltd. Photos by Ling Liu.

a dull to glassy luster. Their colors ranged from pale to deep blue, green-blue, green, or yellow.

Group B. Twenty circular specimens of turquoise with various specific gravities (2.19–2.84) were selected for pore observation. Each sample was cut in half; one half was treated with resin and hardener to enhance the color, while the other was left untreated for comparison.

Group C. A porous and chalky rough sample (figure 6, left) from Zhushan County was cut into a series of block specimens, but we selected two block samples for testing in this study. These specimens were subsequently divided into two groups: (1) untreated and polished and (2) treated with mixed agents of resin and hardener (hereafter referred to as "resin") (figure 6, right) for 2–3 days and then polished.

Characterization Techniques. Specific gravity was determined hydrostatically at the gem testing center of the China University of Geosciences (Wuhan) in Zhushan County. Images of all the samples were captured in a light box (D55 light source) under identical conditions to compare changes in color. Each group was characterized by different techniques (table 1).

Environmental scanning electron microscopy (ESEM) (FEI Quanta 200) was performed on the 20 untreated halves (group B), as well as two block specimens (group C). All samples were coated with carbon and tested in a vacuum at a voltage of 20 kV.

TABLE 1. Techniques used to characterize the turquoise samples prepared by various methods.

Group	No. of samples	Treatment	Characterization techniques	Purpose
A	342	Resin filling	Photography	Comparison and evaluation of quality before and after treatment
B	20	Untreated and Resin filling	ESEM and photography	Pore observation and appearance comparison
C	2	Untreated and Resin filling	UV fluorescence, 3D fluorescence, FTIR, ESEM, and photography	Identification of detection characteristics and porosity comparison

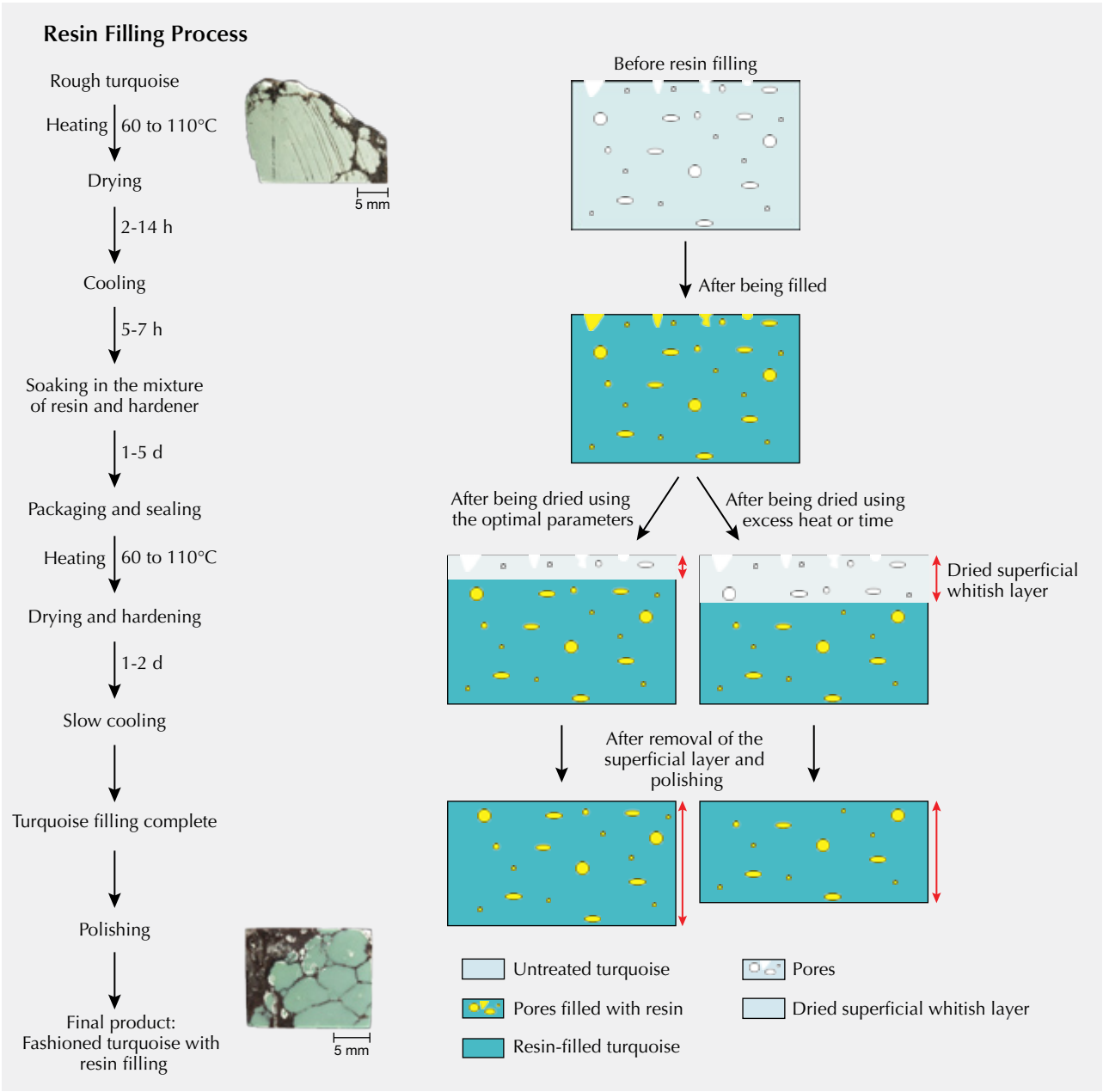

Figure 7. Flowchart (left) and schematic (right) of the process for resin filling of turquoise pores. Illustration by Ling Liu.

Ultraviolet fluorescence was observed under short-wave (SW, 254 nm) and long-wave (LW, 365 nm) UV radiation. 3D fluorescent patterns of untreated, resin-filled block specimens (group C), and resin were collected by a Jasco FP-8500 spectrofluorometer with a xenon lamp light source. The photomultiplier tube (PMT) voltage was adjusted for sample testing (520 V for untreated and resin-filled turquoise, 550 V for resin). The emission range (270–750 nm) was measured with the excitation ranging from 250 to 600 nm at a response time of 0.5 seconds and scan speed of 2000 nm/min. The E_x and E_m bandwidths were set to 5.0 and 2.5 nm, respectively.

Fourier transform infrared (FTIR) spectroscopy was recorded in the range of 400–4000 cm^{-1} with 64 scans at a resolution of 4.0 cm^{-1} using a Bruker VERTEX 80 FTIR spectrometer. The spectra of the untreated and resin-filled block specimens from group C, as well as the mixed agent of resin and hardener, were obtained using the KBr pellet method in transmission mode.

Resin Filling Process. Resin filling aims to enhance the texture or compactness of natural rough turquoise, which crumbles easily and is difficult to process due to its porous structure. The treatment can improve processability, durability, and stability, while also preventing the absorption of sweat, skin oil, and cosmetics. The procedures for our experiments were as follows (figure 7, left):

1. *Preheating and First Drying.* Turquoise needs to be dried by preheating in an oven because it is somewhat hygroscopic and contains water. The initial temperature was set at about 60–80°C and maintained for 2–8 hours depending on sample dimensions. Subsequently, the temperature was increased at a rate of 5–20°C every 2–8 hours. The optimal temperature was raised to ~110°C until all of the absorbed water was evaporated.
2. *Cooling.* The samples were slowly cooled down to room temperature over 5–7 hours. Turquoise should be protected from sharp dips in temperature, which can be destructive.
3. *Soaking*. The dried turquoise was soaked in a mixture of resin and hardener for 1–5 days at room temperature without pressure until it was adequately filled, and it was then packaged and sealed.
4. *Second Drying for Hardening*. Afterward, the samples were placed in an oven for secondary drying and hardening at a preliminary temperature of about 50–90°C for about 3.5 hours. The temperature was then increased by 5–10°C every five hours until peaking at 110°C. After the hardening procedure was completed, the oven was allowed to cool by 20°C every 2 hours until reaching room temperature.
5. Finally, the filled turquoise samples were polished to remove the remaining fillers and superficial whitish dried layer to achieve the improved appearance.

The temperatures and durations given here are approximate because the processing factories requested confidentiality. Optimal parameters mattered significantly for resin filling. Temperature and dwell time should be carefully adjusted according to the size and porosity of the turquoise, as excessive heat and durations damage its inner structure. In addition, a whitish dried layer is produced on the surface of the turquoise after the secondary drying process. If the secondary drying stage (for hardening) was too long, material would be wasted as a thick whitish dried layer would form and need to be removed after resin filling (figure 7, right).

RESULTS

After resin filling, the treated samples were opaque, with a superficial whitish layer; see figure 7 (right) and figure 8 (center). The fashioned treated turquoise displayed obviously enhanced color and luster after polishing (figure 8).

Changes in Turquoise Color After Resin Filling. Most of the samples showed distinct improvement in color after resin filling (figure 9). The most pronounced color changes were observed in chalky and whitish samples with very high porosity, which turned noticeably more saturated in color after the filling. Those samples that had deep color and compact structure were only slightly modified, with barely perceptible color changes discerned since agents would not easily permeate the more compact turquoise.

Figure 8. Variations in some samples at different stages of resin filling. Untreated turquoise (left), turquoise treated with resin before polishing (center), and turquoise treated with resin and polished (right). Photos by Ling Liu.

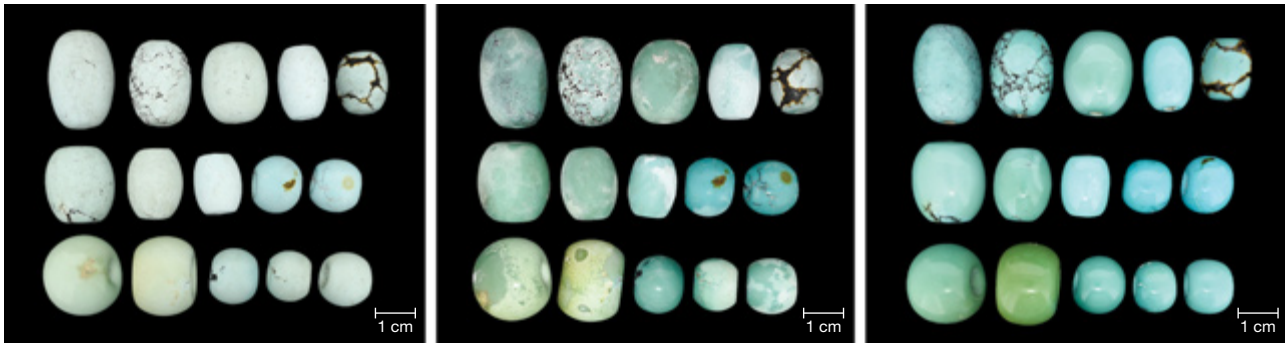

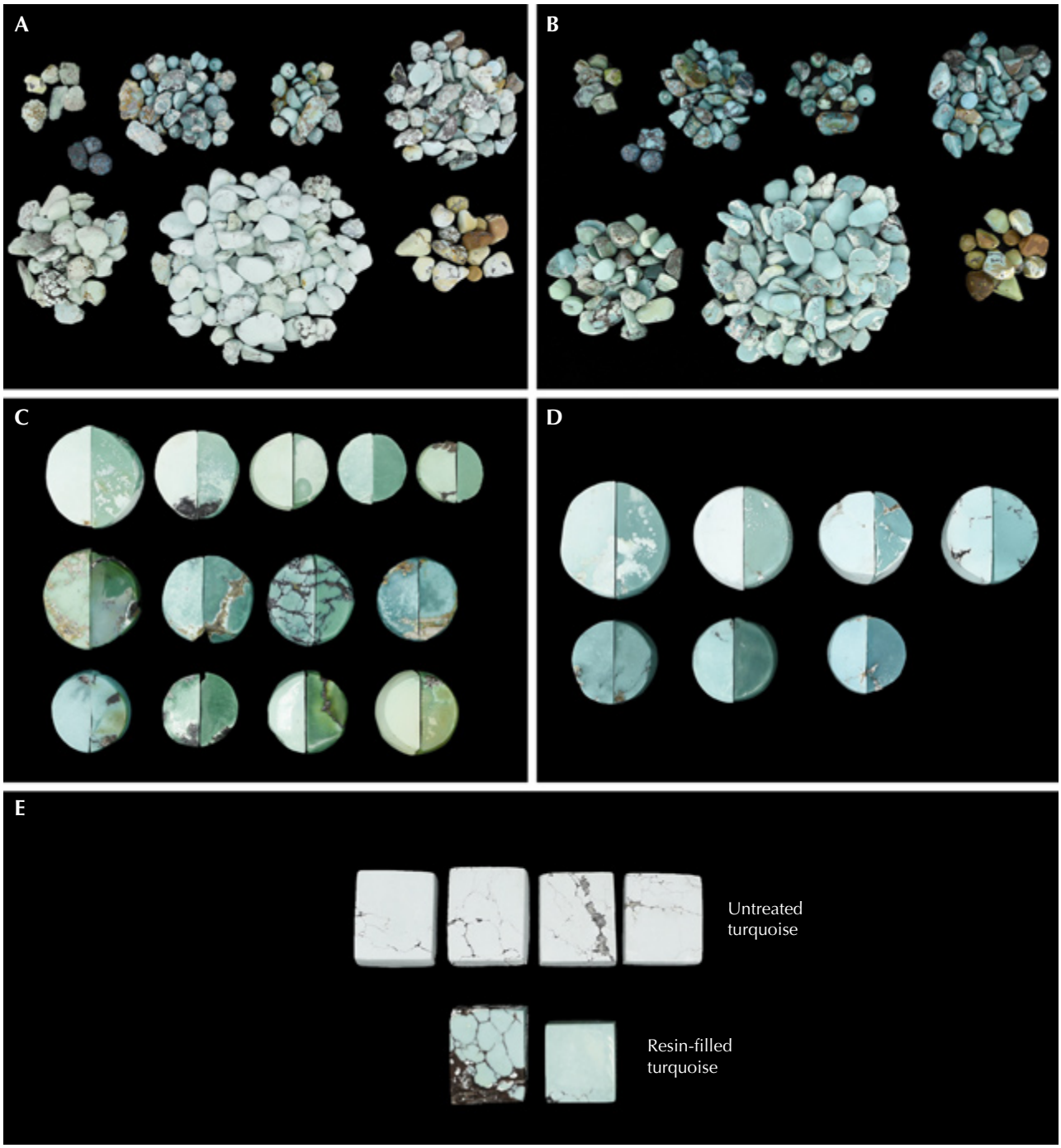

Figure 9. Comparison of untreated turquoise and resin-filled turquoise. Some samples (0.22–2.99 g) of group A before treatment (A) and after (B). C and D: Twenty pieces of turquoise (1.58–4.82 g) were cut in half (group B). The left half of each sample was left untreated, and the right side was treated with resin. Note the deeper and more saturated colors in the resin-filled halves. E: Block specimens (approximately 15 × 20 × 5 mm) cut from a porous and chalky rough sample for treatment alongside an untreated control group (group C). Photos by Ling Liu.

Changes in Turquoise Porosity After Resin Filling. The dark and irregular areas in the ESEM images of turquoise represent surface pores (figure 10). The pores were unevenly distributed and sometimes crowded together, ranging from 20 to 200 µm in diameter with various shapes (circle, triangle, rhom-

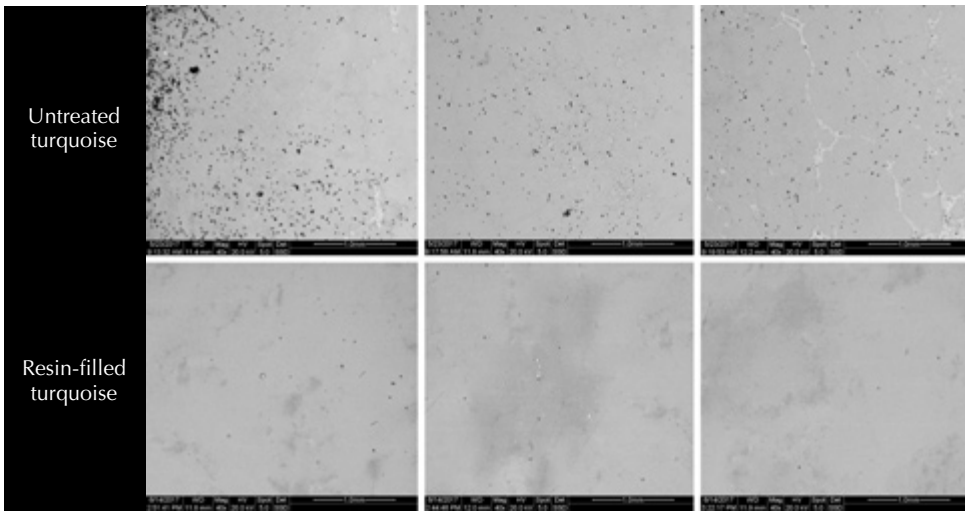

Figure 10. ESEM images showing the distribution of pores in untreated turquoise (top) and resin-filled turquoise (bottom). Note that the untreated turquoise has higher porosity, as evidenced by the dark spots in its ESEM images. Images by Ling Liu.

bus, or wormhole). Very few pores were observed in the ESEM images of the resin-filled sample. The untreated turquoise had higher porosity (approximately 1.9% surface porosity) than the resin-filled one (approximately 0.7%). The reduction of porosity confirmed that the resin effectively lowered the porosity and improved the appearance of samples.

Identification of the Treated Turquoise. *UV Fluorescence*. Untreated turquoise displayed an inert or very weak fluorescence reaction to both short- and long-wave UV. Resin-filled turquoise samples showed no fluorescence under short-wave UV radiation but strong blue fluorescence under long-wave UV (figure 11). The resin was inert to short-wave UV radiation but showed strong milky blue fluorescence under long-wave UV (again, see figure 11).

3D Fluorescence Patterns. There were distinct differences between the 3D fluorescence of untreated and resin-filled samples. Untreated turquoise fluoresced very weakly to the full excitation wavelength range (figure 12). The resin-filled turquoise, however, had a strong main emission peak centered at 444 nm under excitation at 372 nm, as well as a secondary emission shoulder at 460 nm.

Figure 11. Comparative fluorescence reactions of the untreated turquoise, resin-filled turquoise, and resin under SWUV (center) and LWUV (right). Photos by Yuyang Zhang; courtesy of Ling Liu.

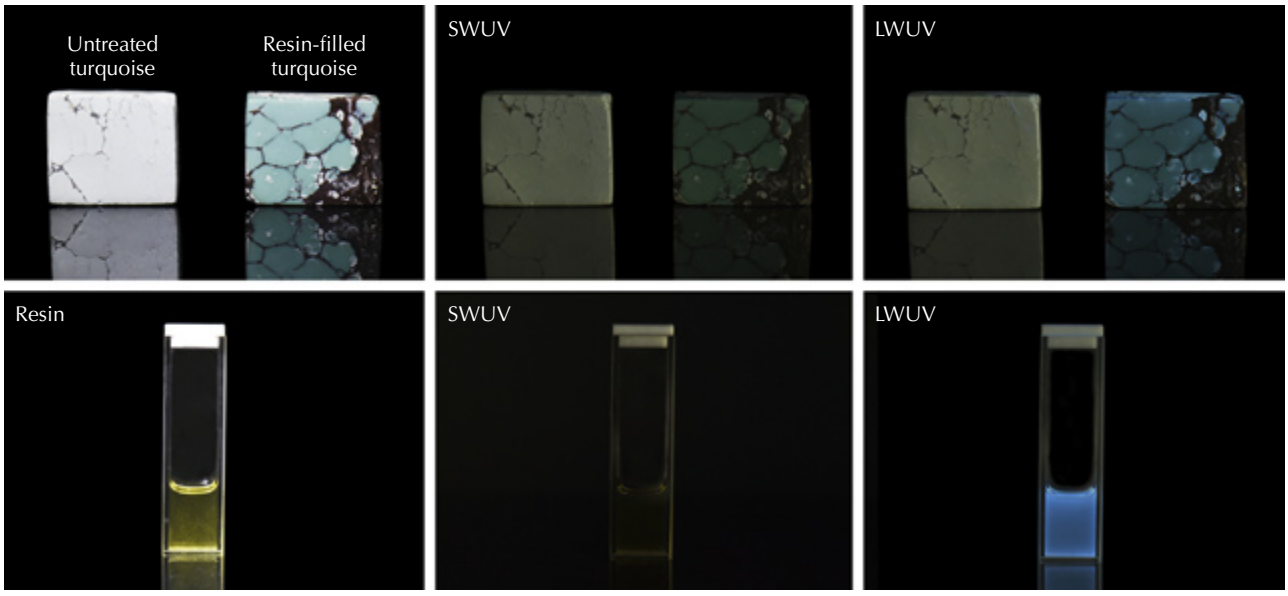

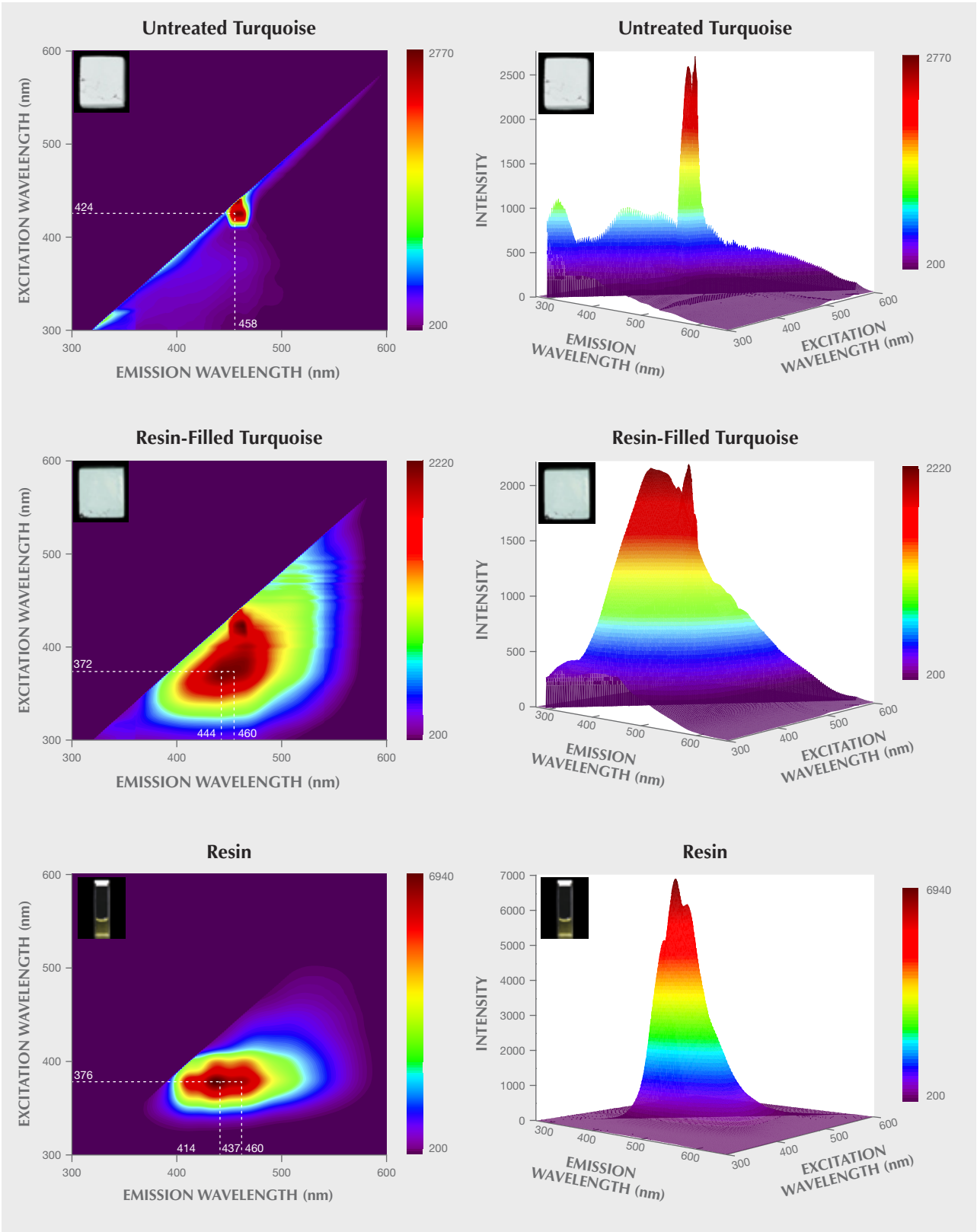

Figure 12. 3D fluorescence patterns of untreated turquoise, resin-filled turquoise, and resin. Note that the emission peak at 458 nm under 424 nm excitation in the untreated and resin-filled samples is attributed not to the tested samples but to the instrument.

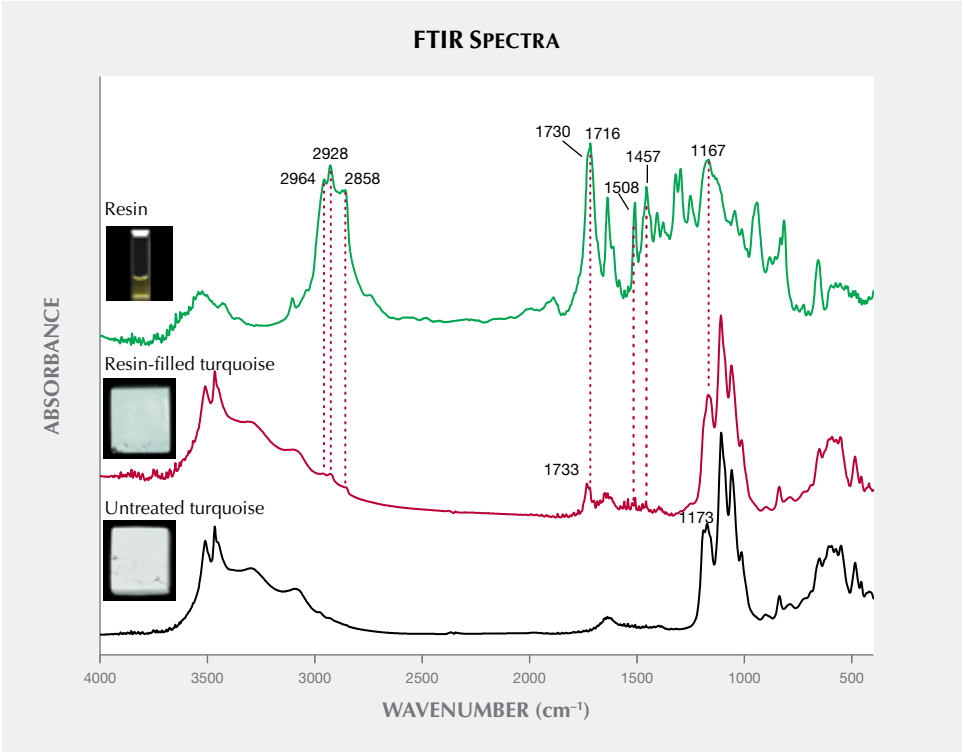

Figure 13. FTIR spectra of untreated turquoise (black line), resin-filled turquoise (red line), and resin (green line). Spectra offset for clarity.

The 3D fluorescence pattern of the resin was also investigated in this study. The pattern exhibited three strong emission peaks centered at 414, 437, and 460 nm when excited by 376 nm light. These three strong emission centers occurring in the resin's 3D fluorescence pattern matched well with those of the resin-filled turquoise. Accordingly, it was assumed that the presence of these strong emission peaks offered proof of resin filling. It should be noted that the varied types and dosages of organic substances used for resin treatment in each factory might alter the 3D fluorescence patterns of the resin-filled turquoise. The 3D fluorescence patterns of various resin-treated turquoise need to be further investigated.

Infrared Spectroscopy. The untreated turquoise showed important bands in two ranges, from 3000–3600 cm^{-1} and 1800–400 cm^{-1}, which are typical variations of OH, H_2O, and PO_4 according to previous research (Reddy et al., 2006; Chen and Qi, 2007; Chen et al., 2012; Cejka et al., 2015). The spectra of the resin-filled turquoise were characterized by the different combinations of turquoise and resin used in the treatment process. As expected, the filled turquoise samples exhibited additional diagnostic bands of resin at approximately 1733 cm^{-1} (figure 13), attributable to C=O vibration (Lind et al., 1983; Pavese et al., 2005; Chen et al., 2006; Moe et al., 2007). Other weak bands appeared at 2964, 2928, 2858, 1716, 1508, 1457, and 1167 cm^{-1} in the spectrum of resin-filled turquoise. The resin is responsible for these bands. It displayed prominent bands at 2964, 2928, 2858, 1730, 1716, 1637, 1509, 1455, 1405, 1377, 1319, 1296, 1251, 1167, 1044, 940, 815, and 656 cm^{-1}, as well as other weak bands.

There were notable differences in the fluorescence reactions and FTIR spectra of the untreated and treated turquoise, which offered diagnostic evidence for identifying resin-filled turquoise.

CONCLUSIONS

Resin filling can effectively improve the appearance of porous rough turquoise. Observations of pore distribution and quantity in both untreated and resin-filled turquoise reveal that most pores can be well filled by resin, resulting in a deeper color without the use of additional colorant. Untreated turquoise fluoresced very weakly to the full excitation wavelengths of light. But the resin-filled turquoise in this research had strong fluorescence under long-wave UV. Under 372 nm excitation, a strong main emission peak centered at 444 nm and a secondary emis-

sion shoulder at 460 nm occurred in its 3D fluorescence patterns. The filled turquoise had an intense band at 1733 cm^{-1}, and other weak bands in IR spectra as well. Fluorescence reactions and the occurrence of additional FTIR bands related to organic resin provide the evidence required to identify resin-filled turquoise.

Pore filling is an economically worthwhile approach to optimize porous rough turquoise, making it suitable for commercial jewelry or ornaments with high added value. The effectiveness of pore-filling treatment in improving the processability, appearance, and durability of this precious gemstone should be recognized, and it needs to be fully disclosed to the consumer.

ABOUT THE AUTHORS

Ms. Liu (lingliu0928@163.com) is a PhD candidate at the Gemmological Institute, China University of Geosciences in Wuhan (CUG). Professor Yang (yangc@cug.edu.cn, corresponding author), Associate Professor Li (yanli@cug.edu.cn), and Associate Professor Di are from Gemmological Institute, CUG. Mr. Chong He is a distinguished gemologist at the Gem Testing Center, CUG. Mrs. Jia Liu is a lab manager and Ms. Ruoxi Chen holds a master's degree in gemology from the Gemmological Institute, CUG.

ACKNOWLEDGMENTS

This research was financially supported by Grant No. 2018YFF0215400 from the National Key R&D Program of China and Grant No. 20BKG030 from the National Social Science Fund of China. This work was also partially supported by the Gemmological Institute, CUG. The authors sincerely thank Mr. Yang Xu at the Gem Testing Center, CUG for kind assistance. Many thanks to Mr. Haitao He (a manager at Baoyuan Mining Co. Ltd in Zhushan County) and the following companies for generously providing the specimens: Long Fu Turquoise Co. Ltd, Bu Tian Sheng Yu Turquoise Co. Ltd, and Hua Zhou Yi Lan Turquoise Co. Ltd.

REFERENCES

Bernardino N.D.E., Izumi C.M.S., de Faria D.L.A. (2016) Fake turquoises investigated by Raman microscopy. *Forensic Science International*, Vol. 262, pp. 196–200, http://dx.doi.org/10.1016/j.forsciint.2016.03.041

Cejka J., Sejkora J., Macek I., Malíková R., Wang L., Scholz R., Xi Y., Frost R.L. (2015) Raman and infrared spectroscopic study of turquoise minerals. *Spectrochimica Acta Part A: Molecular and Biomolecular Spectroscopy*, Vol. 149, pp. 173–182, http://dx.doi.org/10.1016/j.saa.2015.04.029

Chen Q.-L., Qi L.-J. (2007) Study on the vibrational spectra characters of water in turquoise from Ma'anshan. *Journal of Mineralogy and Petrology*, Vol. 27, No. 1, pp. 30–35 [in Chinese].

Chen Q.-L., Qi L.-J., Zhang Y. (2006) IR absorption spectrum representation of turquoise, treated turquoise and imitation. *Journal of Gems and Gemmology*, Vol. 8, No. 1, pp. 9–12 [in Chinese].

Chen Q.-L., Yuan X.-Q., Chen J.-Z., Qi L.-J. (2010a) Study on the treatment turquoise using Raman spectroscopy. *Spectroscopy and Spectral Analysis*, Vol. 30, No. 7, pp. 1789–1792 [in Chinese].

Chen Q.-L., Yuan X.-Q., Chen J.-Z., Zhou J.-H. (2010b) Structural characteristics of turquoise filled with aluminum phosphate adhesive. *Earth Science – Journal of China University of Geosciences*, Vol. 35, No. 6, pp. 1023–1028 [in Chinese].

Chen Q.-L., Yin Z.-W., Qi L.-J., Xiong Y. (2012) Turquoise from Zhushan County, Hubei Province, China. *G&G*, Vol. 48, No. 3, pp. 198–204, http://dx.doi.org/10.5741/GEMS.48.3.198

Choudhary G. (2010) A new type of composite turquoise. *G&G*, Vol. 46, No. 2, pp. 106–113, http://dx.doi.org/10.5741/GEMS.46.2.106

Deng C.-J., Wang D., Xu B., Bai F. (2009) Research on filling treatment of tourmaline. *Journal of Gems and Gemmology*, Vol. 11, No. 3, pp. 42–43, 58 [in Chinese].

Deng Q., Hu J.M., Wang X., Cao Y., Yang W. (2019) Identification of turquoise with "Jia Ci" treatment. In *Proceedings of the China International Gems & Jewelry Academic Conference*, Beijing, pp. 263–267.

Filin S.V., Puzynin A.I. (2009) Prevention of cracking in Ethiopian opal. *Australian Gemmologist*, Vol. 23, No. 12, pp. 579–582.

Fritsch E., McClure S.F., Ostrooumov M., Andres Y., Moses T.M., Koivula J.I., Kammerling R.C. (1999) The identification of Zachery-treated turquoise. *G&G*, Vol. 35, No. 1, pp. 4–16, http://dx.doi.org/10.5741/GEMS.35.1.4

GAAJ Lab Alert: Lead glass filled ruby (2004) Gemmological Association of All Japan, March 15, https://grjapan.ddo.jp/gaaj_report/2004/gaaj_alert-040315en.html

Gambhir R. (2001) Fire opal. *Canadian Jeweller*, Vol. 122, No. 6, p. 66.

Han W., Lu T.J., Dai H.R., Su J. (2015) Impregnated and dyed turquoise. *G&G*, Vol. 51, No. 3, pp. 343–345.

Henn U., Milisenda C. (2005) Turquoise—Properties and occurrences, imitations and treatments. *Gemmologie: Zeitschrift der Deutschen Gemmologischen Gesellschaft*, Vol. 54, No. 2–3, pp. 97–110.

Hu J.M., Wang X., Deng Q. (2019) Study on oiled turquoise. In *Proceedings of the China International Gems & Jewelry Academic Conference*, Beijing, pp. 268–272.

Hu Y., Fan L.W., Xue Q.F. (2013) Study on filling treatment and identification characteristics of opal from Ethiopian. *Journal of Gems and Gemmology*, Vol. 15, No. 2, pp. 32–37 [in Chinese].

Johnson M.L. (2007) Durability testing of filled emeralds. *G&G*, Vol.

43, No. 2, pp. 120–137, http://dx.doi.org/10.5741/GEMS.43.2.120
Johnson M.L., Elen S., Muhlmeister S. (1999) On the identification of various emerald filling substances. *G&G*, Vol. 35, No. 2, pp. 82–107.
Kammerling R.C., Koivula J.I., Kane R.E., Maddison P., Shigley J.E., Fritsch E. (1991) Fracture filling of emeralds: Opticon and traditional "oils." *G&G*, Vol. 27, No. 2, pp. 70–85, http://dx.doi.org/10.5741/GEMS.27.2.70
Koivula J.I., Kammerling R.C., Fritsch E. (1992) Gem News: Modern-day turquoise oiling. *G&G*, Vol. 28, No. 2, p. 137.
Li K., Lu T.J., Dai H., Chen H., Ke J., Zhang J. (2016) Quantitative analysis of turquoise pores by gas adsorption. In *Proceedings of the 2016 National Mineral Science and Engineering Symposium 2016*, pp. 10–12.
Lin X.D., Shen C.Q., Lin Z.Y. (2019) Current status and introduction of electrochemical treatment on turquoise. In *Proceedings of the China International Gems & Jewelry Academic Conference*, Beijing, pp. 258–262.
Lind T., Schmetzer K., Bank H. (1983) The identification of turquoise by infrared spectroscopy and X-ray powder diffraction. *G&G*, Vol. 19, No. 3, pp. 164–168, http://dx.doi.org/10.5741/GEMS.19.3.164
Liu J., Yang M.X., He C., Cao F.F. (2019) Filled turquoise and its corresponding filling solution. *Journal of Gems and Gemmology*, Vol. 21, No. 5, pp. 56–64 [in Chinese].
Lu T.J., Dai H., Tian G.F., Li K., Zhang J., Chen H., Ke J. (2020) Quantitative analysis of pore characteristics of natural and electrochemically treated turquoises based on gas adsorption method and X-ray micro-CT 3D imaging technique. *Earth Science Frontiers*, Vol. 27, No. 5, pp. 247–253, http://dx.doi.org/10.13745/j.esf.yx.2020.5.51 [in Chinese].
McClure S.F., Smith C.P., Wang W., Hall M. (2006) Identification and durability of lead glass–filled rubies. *G&G*, Vol. 42, No. 1, pp. 22–36, http://dx.doi.org/10.5741/GEMS.42.1.22
McClure S.F., Kane R.E., Sturman N. (2010) Gemstone enhancement and its detection in the 2000s. *G&G*, Vol. 46, No. 3, pp. 218–240, http://dx.doi.org/10.5741/GEMS.46.3.218
Moe K.S., Moses T.M., Johnson P. (2007) Polymer-impregnated turquoise. *G&G*, Vol. 43, No. 2, pp. 149–151, http://dx.doi.org/10.5741/GEMS.43.2.149
Pavese A., Prosperi L., Dapiaggi M. (2005) Use of IR-spectroscopy and diffraction to discriminate between natural, synthetic and treated turquoise, and its imitations. *Australian Gemmologist*, Vol. 22, No. 8, pp. 366–371.
Reddy B.J., Frost R.L., Weier M.L., Martens W.N. (2006) Ultraviolet-visible, near infrared and mid infrared reflectance spectroscopy of turquoise. *Journal of Near Infrared Spectroscopy*, Vol. 14, No. 4, pp. 241–250, http://dx.doi.org/10.1255/jnirs.641
Schwarzinger B., Schwarzinger C. (2017) Investigation of turquoise imitations and treatment with analytical pyrolysis and infrared spectroscopy. *Journal of Analytical and Applied Pyrolysis*, Vol. 125, pp. 24–31, http://dx.doi.org/10.1016/j.jaap.2017.05.002
Shen C.Q., Lin X.D., Lin Z.Y. (2018) Colour discussion on turquoise optimized by electrochemical method. *Journal of Gems and Gemmology*, Vol. 20, No. 4, pp. 16–22 [in Chinese].
Xu Y.F., Di J.R. (2018) Gemological identification of natural turquoise and treatment turquoise in Hubei. *Acta Petrologica et Mineralogica*, Vol. 37, No. 4, pp. 646–654 [in Chinese].
Xu Y.T., Yang M.X. (2019) Filling material and characteristic of polymer-impregnated turquoise in Anhui province. *Journal of Gems and Gemmology*, Vol. 21, No. 1, pp. 20–30 [in Chinese].
Zhou J.-H., Yuan X.-Q. (2008) Study on modification of loose turquoise by inorganics filling and cementation. *Journal of Gems and Gemmology*, Vol. 10, No. 3, pp. 31–35, 53 [in Chinese].
Zuo R., Dai H., Jiang X.P., Zhang Q., Zhou Y. (2017) Infrared spectral features of turquoise filled with acrylic polymer. *Geology of Anhui*, Vol. 27, No. 3, pp. 222–224, 236 [in Chinese].

For online access to all issues of GEMS & GEMOLOGY from 1934 to the present, visit:

gia.edu/gems-gemology

How to Calculate Color from Spectra of Uniaxial Gemstones

Che Shen, Aaron Palke, Ziyin Sun, and Mark D. Fairchild

Color is the most important quality for colored stones, one that is widely discussed and studied by gemologists. Understanding the color characteristics of a gemstone can provide a scientific basis to guide its cutting. This study uses visible spectroscopy to determine the unpolarized spectra of a uniaxial material from the polarized spectra (o-ray and e-ray) in order to predict the color of a uniaxial gem material when viewed in any direction. A seemingly intuitive way of doing this, by adding weighted amounts of the o-ray and e-ray *absorption* spectra, does not actually work for estimating the unpolarized spectra. The mathematically and physically correct way to reconstruct these unpolarized spectra is to add weighted polarized *transmittance* spectra and then to convert back to absorption if desired. This method allows color to be accurately predicted for a material when viewed in any direction as long as the polarized spectra and the viewing angle relative to the c-axis are known. This method has been verified by comparison with a synthetic V-bearing sapphire and a synthetic Cr-bearing sapphire cut into wafers (not faceted gemstones) at various angles relative to the optic axis.

Most gem materials are minerals with crystal structures exhibiting long-range order, such as diamonds, rubies, and sapphires. In order to fully understand their color behavior, one must consider these gem materials from the perspective of their crystallographic characteristics. All crystals can be divided into three categories: isometric, uniaxial (see figure 1), and biaxial.

Polarized Light. Light is a form of electromagnetic radiation that can be considered as waves traveling in one direction at the speed of light with electric and magnetic field components vibrating perpendicular to the direction of travel. The colorimetric properties of light that reaches our eyes are determined by the spectrum of wavelengths present in the light beam. In general, white light as produced by the sun or an incandescent bulb is unpolarized, meaning the electric field component has no preferred orientation, with every oscillation direction equally represented. When unpolarized light passes through either a uniaxial or biaxial material in a direction not parallel to the optic axis, it splits into two distinct rays that have electric field oscillation directions perpendicular to each other (Tilley, 2020). This can be seen by observing uniaxial or biaxial crystals with transmitted polarized light, where in most cases we will observe different colors with different orientations (see figure 2). This, in turn, is because most colored uniaxial or biaxial minerals will absorb light differently when the electric field polarization orientation of the light changes.

In Brief

- In order to quantitatively describe the color of gem materials, it is most appropriate to consider them under an unpolarized light condition.
- The color of a uniaxial gemstone can be predicted by its polarized spectra (o-ray and e-ray).
- The mathematically and physically correct way to reconstruct these unpolarized spectra is based on the square of cosine and sine functions of o-ray and e-ray, provided the incident light angle relative to the optic axis is known.

Color from the Spectrum. The perception of color as experienced by human observers is determined by three main factors: lighting condition, the human visual system, and the object itself. Colorimetry is the

See end of article for About the Authors and Acknowledgments.
Gems & Gemology, Vol. 57, No. 1, pp. 36–45,
http://dx.doi.org/10.5741/GEMS.57.1.36
© 2021 Gemological Institute of America

Figure 1. Corundum is an example of a negative uniaxial mineral. This ruby crystal in matrix from Mogok, Myanmar, is approximately 6.15 cm in length. The cut gem is a 3.22 ct unheated ruby, also from Mogok. The cut gem is courtesy of Jeffrey Bergman, Primagem. Photo by Robert Weldon/GIA.

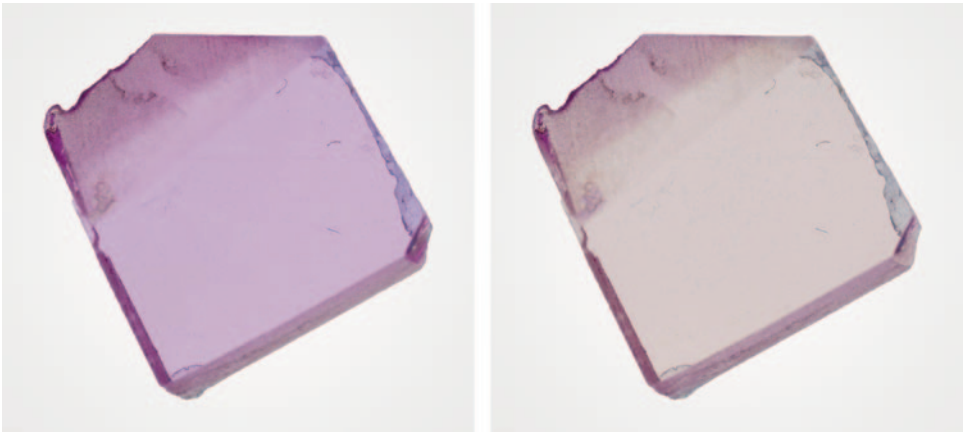

Figure 2. Images of a polished wafer of synthetic pink sapphire photographed under different polarized lighting conditions. Left: Electric field component perpendicular to the optic axis (E⊥c or o-ray). Right: Electric field component parallel to the optic axis (E||c or e-ray).

field of study that deals with quantitative descriptions of color perception. The color stimuli of transparent materials (e.g., gemstones) will depend on which wavelengths of light pass through the material in the visible range (approximately 380–780 nm). Figure 3 illustrates the absorption spectrum of a synthetic pink sapphire that shows which wavelengths of unpolarized light are selectively absorbed by the material (high values of absorbance) and which wavelengths are less absorbed (low absorbance). The term *pleochroism* is used to describe the phenomenon whereby light with different polarization directions produces distinct colors due to differences in the way polarized light is absorbed by uniaxial or biaxial minerals (Hughes, 2014). For a uniaxial mineral, there are two unique electric field oscillation directions, either perpendicular to the optic axis[1] (o-ray) or parallel to the optic axis (e-ray). (Note that in this manuscript, we make use of the o-ray and e-ray terminology, which is equivalent to the E⊥c and E||c terminology more commonly used in the mineralogical literature.) For a uniaxial material such as ruby, the absorption spectrum changes with polarization direction from the o-ray to the e-ray (figure 4).

Figure 3. For the unpolarized visible light spectrum of the synthetic pink sapphire sample (top right) taken at a specific angle of incidence, the calculated color is shown below the sample. The calculation is based upon CIE's 1931 color-matching function (CIE, 1932) and D65 lighting. The color is reproduced based on sRGB color space. The ruby wafer is 2.754 mm thick and has a chromium concentration of 111 ppma.

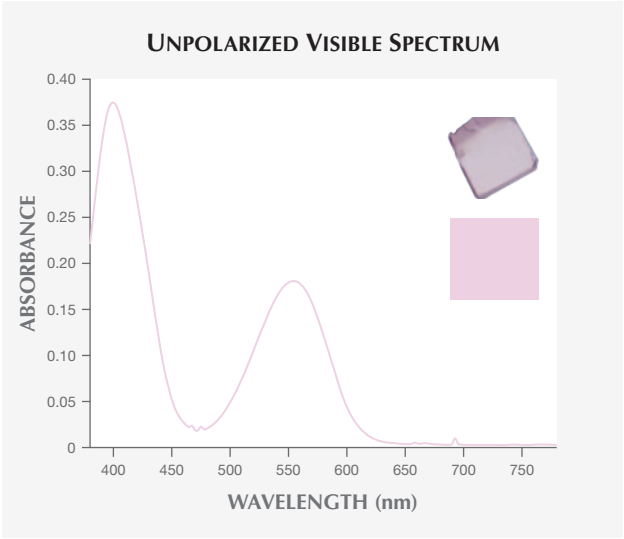

The perceived color of light after passing through a polished wafer of any uniaxial material can be calculated using transmittance spectra (both polarized and unpolarized) and the incident light angle relative to the c-axis combined with the spectral power distribution of the original lighting condition (e.g., daylight-equivalent D65 illumination or incandescent illumination), as well as the human vision responsivity functions that describe how the combination of wavelengths reaching the eye are translated into color.

In general, most light sources are unpolarized. Therefore, it is most appropriate to consider any material under unpolarized light when determining the perceived color. For uniaxial minerals, when unpolarized light is transmitted parallel to the optic axis, all of the rays are equivalent o-rays, with their electric field oscillation direction perpendicular to the optic axis. However, when unpolarized light passes through

[1]The optic axis is not a single line, but a direction (Hecht, 2001). From figure 6, the dotted line represents the direction of the optic axis. n_o represents the o-ray electric field oscillation direction while n_e represents the e-ray electric field oscillation direction. Scientific journals also use E||c, which is equal to the e-ray, and E⊥c, which is equal to the o-ray.

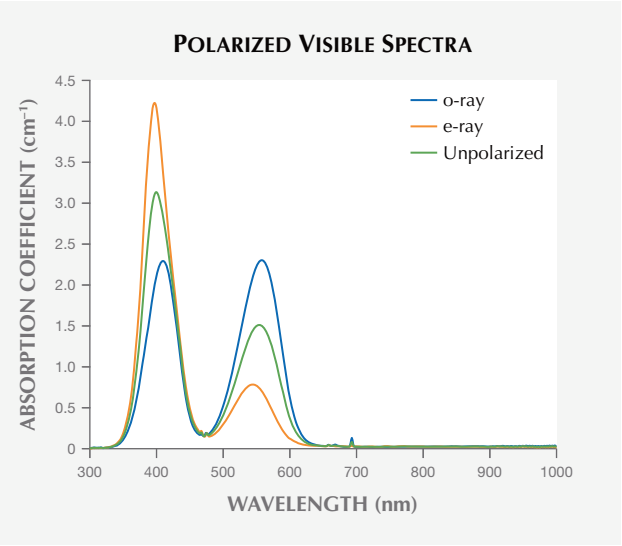

Figure 4. Polarized spectra of an optically oriented wafer of synthetic ruby (same as in figures 2 and 3) with the o-ray (blue line) and e-ray (orange line) polarized directions as well as unpolarized light (green line).

the material perpendicular to the optic axis, it splits into two different rays: an o-ray and an e-ray, vibrating perpendicular and parallel to the optic axis, respectively. When unpolarized light passes through a uniaxial material in any random direction, it will also split into two rays, with one ray constrained to vibrate along the o-ray and the other vibrating perpendicular to both the o-ray oscillation direction and the path of the light ray. Based on the authors' knowledge, however, the exact means of determining the unpolarized absorption spectrum of a uniaxial mineral in any general direction has never been clearly elucidated. As will be demonstrated in subsequent sections, the intuitive means of mixing the o-ray and e-ray *absorption* spectra weighted according to the geometry of any general direction is not correct and cannot reproduce experimentally measured spectra. In this contribution, we demonstrate that one must use weighted combinations of o-ray and e-ray *transmission* spectra in order to determine the absorption spectrum, and hence the color, of a uniaxial mineral for a given input illumination ray angle and viewing angle.

MATERIALS AND METHODS

Samples. The synthetic ruby and sapphire samples were provided by GIA's Carlsbad research laboratory. All samples were prepared as wafers with an optical-quality finish. The crystal orientation was well controlled by the biaxial crystal orienting device described by Thomas et al. (2014).

UV-Vis-NIR Spectroscopy. The polarized UV-Vis spectra were collected with a specially modified Hitachi U-2910 spectrophotometer. The spectra were collected in the 190–1100 nm range with 1 nm spectral resolution at a scan speed of 400 nm/min. The unpolarized spectra were collected with a PerkinElmer Lambda 950 UV-Vis spectrophotometer (PE 950) in the 200–1000 nm range, also with 1 nm spectral resolution. We also checked the degree of polarization of the generated unpolarized light from the PE 950. The results showed that the PE 950 can produce ideal unpolarized light (see box A), which means the unpolarized spectra are appropriate for the spectral analysis. Both polarized and unpolarized spectra were collected at GIA's Carlsbad laboratory.

RESULTS AND DISCUSSION

This research began with an accidental discovery. In 2018, the lead author (CS) worked as a research intern in GIA's Carlsbad laboratory studying chromophores in corundum. At first, all of the UV-Vis spectra for corundum were collected using the Hitachi U-2910 spectrophotometer, which is set up at GIA only to collect polarized spectra. However, the author also wanted to collect some unpolarized spectra at the same time for the purpose of calculating color seen with unpolarized light. To save time, we came up with a hypothesis that one could recreate the unpolarized absorption spectra of a corundum wafer in a general orientation with weighted versions of the o-ray and e-ray absorption spectra. For example, light traveling perpendicular to the optic axis will split into two orthogonal rays, and the unpolarized spectrum was predicted to be equal to the sum of half of the o-ray absorption spectrum and half of the e-ray absorption spectrum (see equation 1):

$$A_{unpolarized} = 0.5 \times A_{o\text{-}ray} + 0.5 \times A_{e\text{-}ray} \quad (1)$$

In order to verify this hypothesis, the PerkinElmer Lambda 950 UV-Vis spectrophotometer was used for collecting unpolarized spectra of vanadium-bearing sapphire with unpolarized light traveling perpendicular to the optic axis. The vanadium-bearing sapphire had strong pleochroism, which meant there were large differences between the o-ray and e-ray spectra. Therefore, if the predicted and measured spectra were in good agreement, we could conclude that the hypothesis is correct. The measured and predicted spectra (using weighted absorption spectra as in equation 1) are shown in figure 5. Because of the significant difference between the estimated and

BOX A: DEGREE OF POLARIZATION

Degree of polarization (DOP) is basically a quantity used to describe the portion of a beam of light that is polarized. The DOP is given by the following equation:

$$DOP = \frac{I_{max} - I_{min}}{I_{max} + I_{min}}$$

where I_{min} and I_{max} are the minimum and maximum intensities of the light in the full range of polarization directions, respectively. A perfectly polarized beam of light has a DOP of 100%, while a DOP of 0% represents perfectly unpolarized light. In this research, a PerkinElmer Lambda 950 UV-Vis spectrophotometer was used to collect unpolarized spectra. This instrument has a removable polarizer, and we collected unpolarized spectra without it. However, with most commonly used spectrophotometers, the beam reflection off the grating and other optics will render the light partially polarized. For this reason, the spectrophotometer used in this study incorporated a depolarizer after the grating. Nonetheless, any potentially slightly unpolarized light could affect the measurement results. To test our PerkinElmer Lambda 950 spectrophotometer, we chose a synthetic ruby cut as a wafer oriented 60° from the optic axis and collected unpolarized spectra with three different rotation angles relative to the cut wafer face (0°, 45°, and 90°). Any significant differences among these spectra would suggest that the "unpolarized" light is actually partially polarized. If there is no difference between the spectra, this would indicate there is no inherent polarization of the light in the spectrophotometer. Figure A-1 illustrates the unpolarized spectra of three different rotation angles, and this experiment confirmed that the light in this spectrophotometer is completely unpolarized. Hence, we can use the measured unpolarized spectra for color calculations.

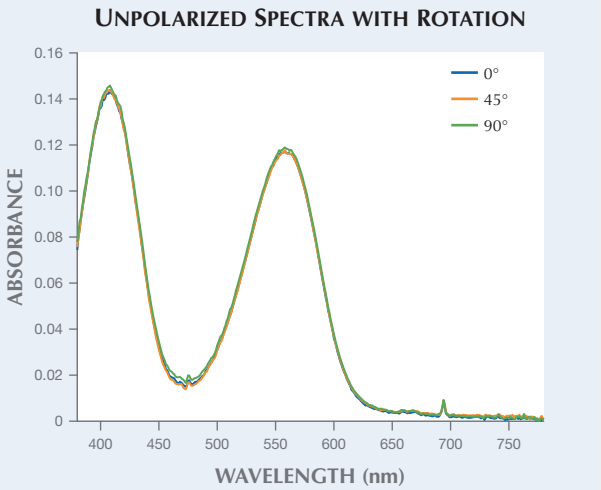

Figure A-1. Unpolarized spectra of an optically oriented synthetic ruby wafer (60° from the optic axis) with rotation angles of 0° (blue line), 45° (orange line), and 90° (green line).

measured spectra, we determined that this hypothesis is wrong and the unpolarized absorption spectrum cannot be reconstructed from appropriately weighted versions of the o-ray and e-ray absorption spectra.

At this point we realized that predicting unpolarized absorption spectra is more complicated than we initially thought. In this research, we explain why we cannot use weighted combinations of o-ray and e-ray absorption spectra to determine the unpolarized absorption spectrum. In addition, we also provide a reasonable method for predicting the absorption spectra in any general orientation. The key to this method is that all the calculations should be based on transmission spectra instead of absorption spectra. This solution can be arrived at intuitively since the addition of two different absorption spectra mathematically requires that all of the light is simultaneously absorbed by both absorption spectra. For instance, if we add together a Cr and V absorption spectrum to represent a Cr- and V-bearing material, the full light is simultaneously absorbed by Cr and V. However, when considering the splitting of light into two polarized rays in a uniaxial material, the two rays of light are independent with each ray being blind to the other. To mathematically model this, it is necessary to convert absorption to transmission to effectively split these two rays of light. See the discussion below.

Unpolarized Light Traveling Parallel to the Optic Axis. In the case of cubic crystals, the refractive indices of the incident light in any polarization direction are identical (Tilley, 2020). However, when dealing with uniaxial crystals, the refractive indices of the o-ray and e-ray are not equal. A beam of light traveling through a uniaxial crystal splits into two orthogonal beams, each with its own refractive index. When light travels parallel to the optic axis, the light will vibrate in all directions perpendicular to the light ray path. Figure 6 demonstrates this with the uniaxial material represented by an ellipsoid de-

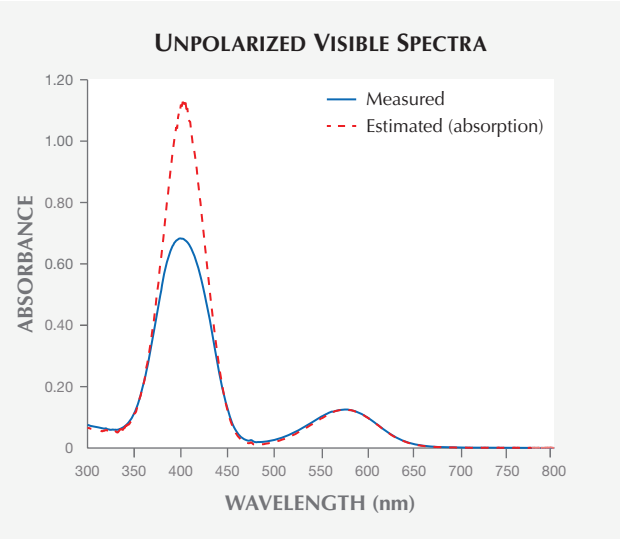

Figure 5. Measured (blue line) and estimated (red dotted line) absorption spectra. The estimated method was based on weighted combinations of o-ray and e-ray absorption spectra (which was found to be an invalid method).

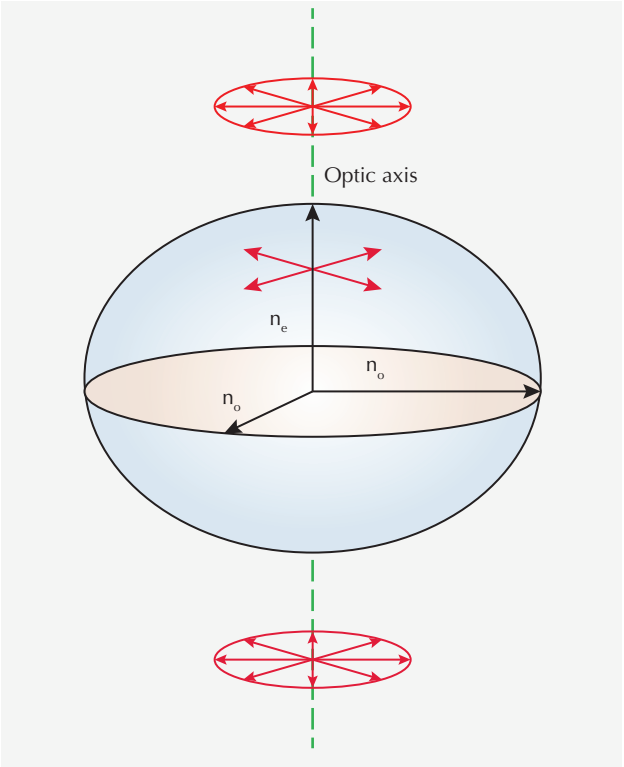

Figure 6. A beam of light incident on a uniaxial negative indicatrix (n_o>n_e) with a direction of travel parallel to the optic axis (green dotted line).

fined by the refractive indices of o-ray and e-ray light. The optic axis is vertical in this diagram, and a cross section perpendicular to the optic axis is a circle with a radius equal to the refractive index of the o-ray (n_o). Therefore, when light passes through a uniaxial material along the optic axis, it vibrates perpendicular to the optic axis.

Unpolarized Light Traveling Perpendicular to the Optic Axis. When light travels perpendicular to the optic axis, it will split into two rays with orthogonal electric field directions. In this case, for a uniaxial crystal, the cross section of the indicatrix is an ellipse rather than a circle (figure 7). One of the split rays will have its electric field oscillation direction parallel to the optic axis (an e-ray), while the other ray will vibrate perpendicular to the optic axis (an o-ray). Light traveling in this direction will be equally split into o-ray and e-ray light.

This is best thought of by considering the intensity, or radiant flux, of the incident light being split in half between an o-ray and an e-ray. The relationship between transmittance and radiant flux can be expressed as in equation 2:

$$T = \frac{\Phi^t}{\Phi^i} \quad (2)$$

where

- T is transmittance
- Φ^t is the transmitted radiant flux through the material
- Φ^i is the initial radiant flux received by the material

Because the o-ray and e-ray each receive half of the radiant flux incident on the material, equation 2 could be rewritten as:

$$T_{unpolarized} = \frac{0.5 \times \Phi^t_{o\text{-}ray} + 0.5 \times \Phi^t_{e\text{-}ray}}{\Phi^i} = 0.5 \times (T_{o\text{-}ray} + T_{e\text{-}ray}) \quad (3)$$

where

- $\Phi^t_{o\text{-ray}}$ is the transmitted radiant flux associated with the o-ray
- $\Phi^t_{e\text{-ray}}$ is the transmitted radiant flux associated with the e-ray

Equation 3 shows mathematically why simply adding absorption spectra as in equation 1 is incorrect, since there is a logarithmic relationship between transmittance and absorbance: $A = -log(T)$. To verify our formula, unpolarized light was used to measure the vanadium-bearing sapphire wafer with faces cut and polished parallel to the optic axis. Next, we compared the measured spectrum with the cal-

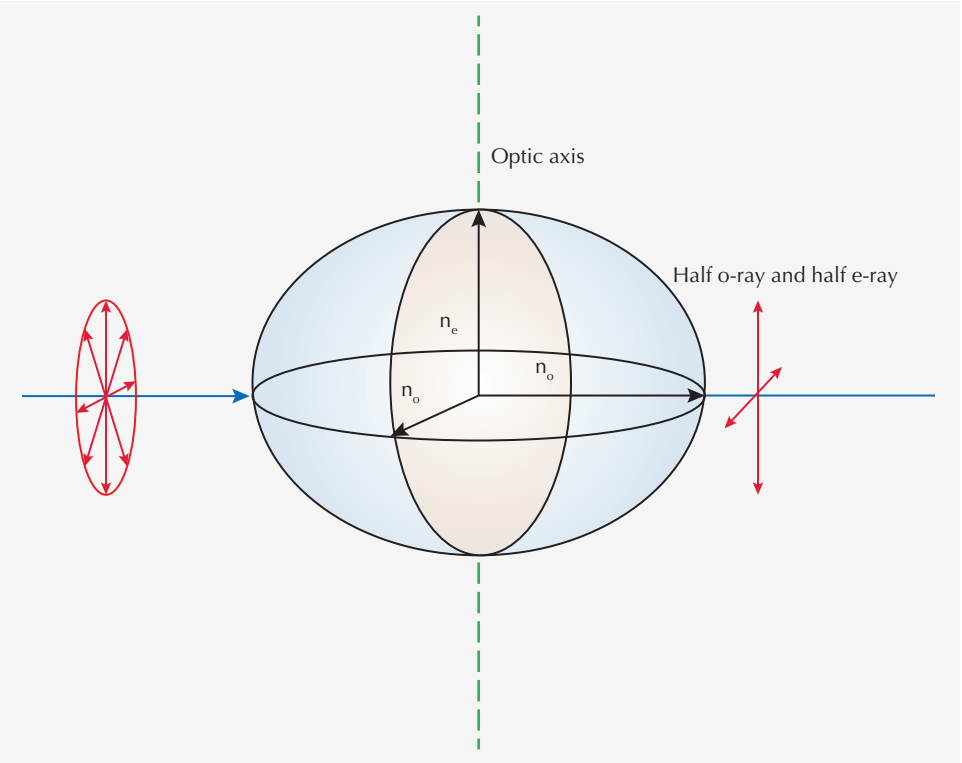

Figure 7. A beam of light incident on a uniaxial negative indicatrix (n_o>n_e) with a direction of travel perpendicular to the optic axis.

culated spectrum based on equation 3 using the measured o-ray and e-ray absorption spectra converted to transmittance. The results are shown in figure 8. We can see from figure 8 that the estimated spectrum agrees well with the measured spectrum. We can also calculate the color from the estimated spectrum and the measured spectrum as well as the spectrum estimated by the method of using weighted absorption spectra (equation 1). These three colors are reproduced in figure 9. The color difference value,

Figure 8. Transmittance spectra of an optically oriented wafer (c-axis parallel to the polished faces) of a vanadium-bearing sapphire. The estimated unpolarized spectrum (red dotted line) is calculated based on equation 3.

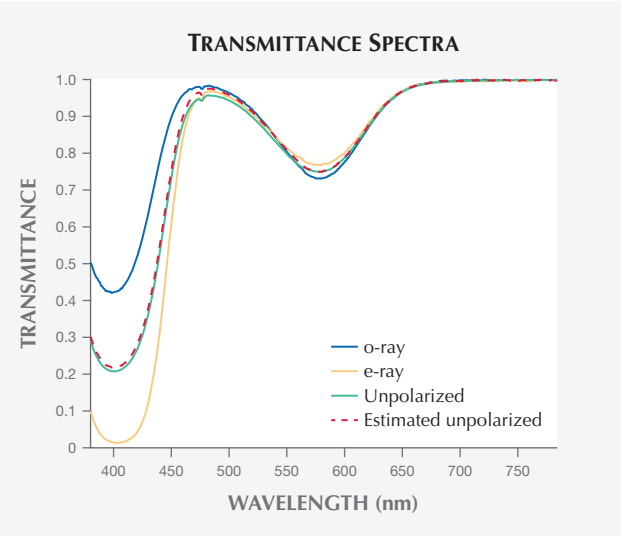

Figure 9. Generated color where the bottom third is calculated based on the measured spectrum, the left third based on the correctly estimated spectrum, and the right third based on an incorrectly estimated spectrum.

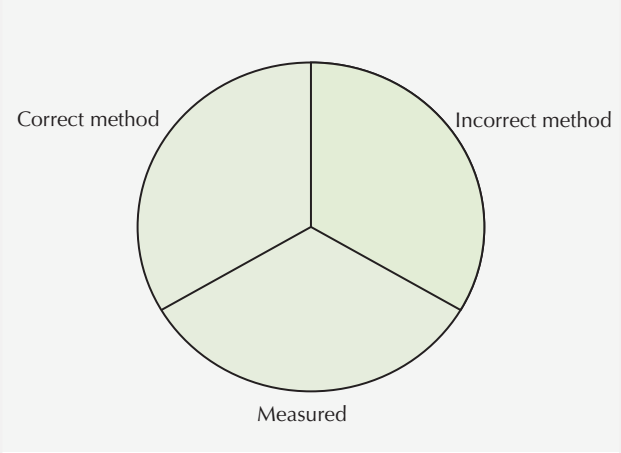

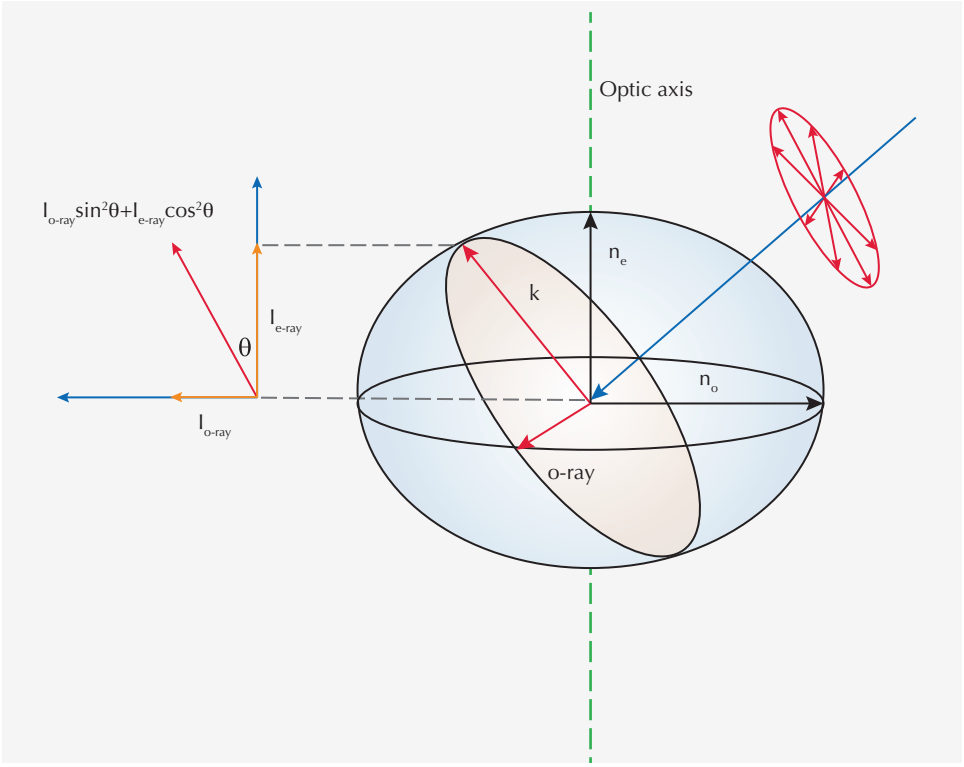

Figure 10. A beam of light incident on a uniaxial negative indicatrix ($n_o>n_e$) in any general direction, where I *represents the intensity of light and* θ *is the angle between the cross section (orange ellipse) and the optic axis. The intensity of the ray of light vibrating perpendicular to the o-ray (the k-ray in the figure) can be expressed as the square of the cosine and sine functions of* θ.

ΔE_{00} (Luo et al., 2001), between the correctly estimated and measured spectra is 0.80, while the ΔE_{00} between the incorrectly estimated and measured spectra is 1.79, demonstrating the accuracy of using transmittance spectra to predict color.

Unpolarized Light Incident in a Random Direction. When considering a beam of light traveling through a uniaxial material in any general direction relative to the c-axis, the situation is slightly more complicated. However, we can still use the framework developed in the previous sections covering samples measured with the polished face parallel and perpendicular to the optic axis using unpolarized light. From the optical indicatrix shown in figure 10, it is obvious that when light traveling through a uniaxial material in a general direction is split into two rays, one of them can be described as the o-ray while the other ray (k) is a mixture of an o-ray and an e-ray. Based on Malus's law (Collett, 2005), the component of the split light (k) along the o-ray and e-ray polarized directions can be calculated according to equation 4:

$$I_k = \sin^2\theta \times I_o + \cos^2\theta \times I_e \quad (4)$$

where

- I represents the intensity of light along the specified polarization
- θ is the angle between the cross section (see also figure 10) and the optic axis

Since transmittance is proportional to the light intensity[2], equation 4 can be rewritten as equation 5 and the final equation for calculating the unpolarized spectrum in any general direction can be expressed as equation 6:

$$T_{unpolarized(k)} = \sin^2\theta \times T_{o\text{-}ray(k)} + \cos^2\theta \times T_{e\text{-}ray(k)} \quad (5)$$

$$T_{unpolarized} = 0.5 \times T_{o\text{-}ray} + 0.5 \times (\sin^2\theta \times T_{o\text{-}ray} + \cos^2\theta \times T_{e\text{-}ray}) \quad (6)$$

When the light travels parallel to the optic axis, θ = 90°, $\sin^2\theta = 1$, $\cos^2\theta = 0$, and equation 6 is equal to $T_{o\text{-}ray}$. When the light travels perpendicular to the optic axis, θ = 0°, $\sin^2\theta = 0$, $\cos^2\theta = 1$, and equation 6 is equal to equation 3.

To verify the accuracy of equation 6, the authors selected a high-quality, homogeneous synthetic ruby and cut it into four double-sided polished wafers. These four wafers were accurately oriented using the biaxial crystal orienting device described by Thomas et al. (2014). The angles between the polished faces of the four wafers and the optic axis are 0°, 30°, 45°, and 60°, respectively. Unpolarized spectra were

[2]The total radiant flux is 4π *sr* times the radiant or light intensity when dealing with isotropic radiation. Note: *sr* represents "steradian."

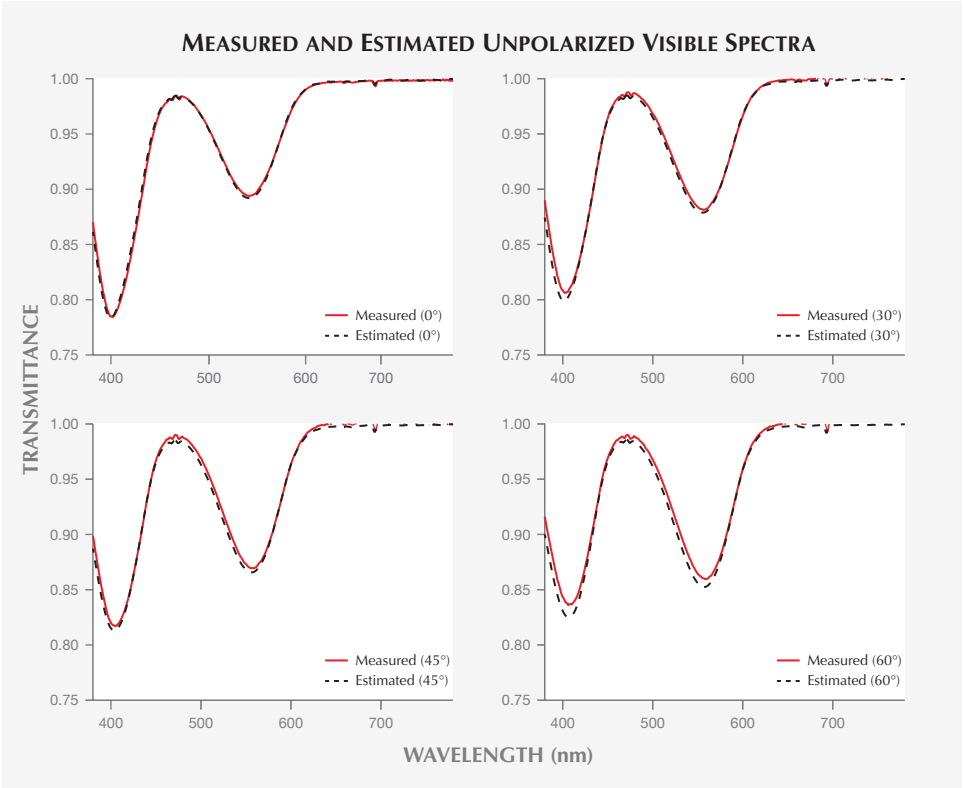

Figure 11. The measured spectra (red line) and estimated spectra (black dotted line) for the sample using 0°, 30°, 45°, and 60° angles between polished faces and the optic axis.

measured for these four samples as well as polarized spectra (o-ray and e-ray) from the 0° sample. The measured spectra and estimated spectra (based on equation 6) are shown in figure 11, illustrating that the estimated spectra agree well with the measured spectra. Therefore, equation 6 can be used to reconstruct the unpolarized spectrum of a sample of a uniaxial material at any known angle relative to the c-axis from the o-ray and e-ray spectra. In addition, the colorimetric data as well as the ΔE_{00} values are shown in table 1. The very small ΔE_{00} values for all four tested angles illustrate the high accuracy of the estimated spectra and are similar in magnitude to the expected uncertainty between two measuring instruments. To get a sense of the magnitude of ΔE_{00} values, the repeatability of an instrument for uniform samples without replacement on a single instrument is on the order of 0.05–0.10, reproducibility of measurements across different times or instruments is on the order of 0.5–1.0, and perceptibility thresholds for color differences are on the order of 1.0–2.0. The precise magnitudes depend on the uniformity of the samples, the specific instrument, the measurement geometry, and viewing conditions such as background, illumination color, and illuminance level (Berns, 2019).

TABLE 1. Colorimetric data of estimated and measured spectra.

	L*	a*	b*	ΔE00
Measured (0°)	97.39	2.58	–0.57	0.37
Estimated (0°)	97.35	2.82	–0.81	
Measured (30°)	97.13	3.05	–1.36	0.31
Estimated (30°)	97.04	3.30	–1.42	
Measured (45°)	96.88	3.48	–1.96	0.36
Estimated (45°)	96.73	3.77	–2.04	
Measured (60°)	96.65	3.86	–2.56	0.49
Estimated (60°)	96.42	4.26	–2.66	

Since the relationships between different angles and unpolarized spectra were directly measured, a 3D plot where the incident angle (θ) is plotted against transmittance spectra (o-ray, e-ray, and unpolarized) to demonstrate the variation of the contribution of each polarized ray (not full transmittance) at various angles is presented in figure 12.

CONCLUSIONS

The unpolarized spectra of uniaxial materials in any direction can be reconstructed from the square of the cosine and sine functions of o-ray and e-ray, provided the incident light angle θ relative to the c-axis (optic

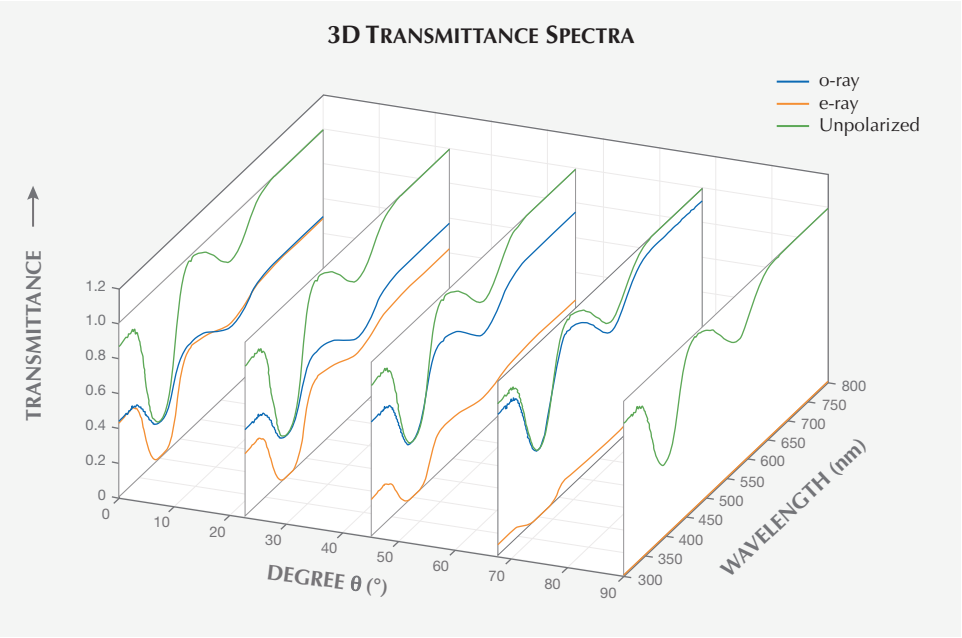

Figure 12. The unpolarized transmittance spectra (green line) of a vanadium-bearing sapphire and the contribution of each polarized ray (o-ray = blue line, e-ray = orange line) at different equally spaced angles (0.0, 22.5°, 45.0°, 67.5°, 90.0°) relative to the optic axis.

axis) is known. This calculated function, expressed in equation 6, was derived theoretically and verified experimentally. The extension of this theoretical framework from polished wafers to faceted gemstones represents a significant challenge and will be the focus of future work.

ABOUT THE AUTHORS

Mr. Shen is a PhD student in the Munsell Color Science Laboratory at the Rochester Institute of Technology (RIT), majoring in color science. Dr. Palke is senior manager of colored stone research and Mr. Sun is a research associate at GIA in Carlsbad, California. Dr. Fairchild is professor and founding head of the Integrated Sciences Academy in RIT's College of Science and director of the Program of Color Science and the Munsell Color Science Laboratory. He is a Fellow of the Society for Imaging Science and Technology (IS&T) and the Optical Society of America (OSA).

ACKNOWLEDGMENTS

The authors would like to thank three anonymous peer reviewers as well as GIA's Nathan Renfro and Troy Ardon, who provided many useful comments and suggestions. This research project is sponsored by the GIA research internship program.

REFERENCES

Berns R.S. (2019) *Billmeyer and Saltzman's Principles of Color Technology*. John Wiley & Sons, Hoboken, New Jersey.

CIE (1932) Commission internationale de l'eclairage en succession a la Commission Internationale de Photométrie Huitième Session, 1931. Cambridge University Press, Cambridge, UK.

Collett E. (2005) *Field Guide to Polarization*. SPIE, Bellingham, Washington.

Hecht E. (2001) *Optics*. Addison-Wesley, Lebanon, Indiana.

Hughes R.W. (2014) Pleochroism in faceted gems: An introduction. *G&G*, Vol. 50, No. 3, pp. 216–226, http://dx.doi.org/10.5741/GEMS.50.3.216

Luo M.R., Cui G., Rigg B. (2001) The development of the CIE 2000 colour-difference formula: CIEDE2000. *Color Research and Application*, Vol. 26, No. 5, pp. 340–350, http://dx.doi.org/10.1002/col.1049

Thomas T., Rossman G.R., Sandstrom M. (2014) Device and method of optically orienting biaxial crystals for sample preparation. *Review of Scientific Instruments*, Vol. 85, No. 9, p. 093105, http://dx.doi.org/10.1063/1.4894555

Tilley R.J.D. (2020) *Colour and the Optical Properties of Materials*. John Wiley & Sons, Ltd., Hoboken, New Jersey.

CHARTS

Micro-Features of Spinel

Nathan Renfro, John I. Koivula, Shane F. McClure, Kevin Schumacher, and James E. Shigley

Spinel has long been an underappreciated gem, often placed in the shadows of its traditionally more expensive gemstone cousin, the ruby. Historically, red spinel was visually mistaken for ruby before being acknowledged as its own mineral species, the most notable being the Black Prince's ruby which adorns the Imperial State Crown on display in London. In recent years, spinel has seen a significant rise in popularity and is recognized as one of three birthstones for August. Spinel's appeal may be due in part to its range of colors, from red to pink, purple, blue, gray, and orange (figures 1 and 2).

Spinel is an isometric mineral that often forms as a result of contact metamorphism, finding its home in magnesium-rich dolomite marbles, as is the case with spinel from Myanmar and Pakistan. Other notable spinel sources are Sri Lanka, Tanzania, and Tajikistan.

Gems & Gemology, Vol. 57, No. 1, pp. 46–49,
http://dx.doi.org/10.5741/GEMS.57.1.46
© 2021 Gemological Institute of America

Inclusions found in spinel often reflect the geologic conditions in which they form, with carbonate inclusions (such as calcite) being quite common, as well as apatite crystals. Notably, many spinels contain well-formed octahedral negative crystals that are typically filled with solid minerals, fluids, or a combination of both. Metal sulfides are occasionally present, as well as intergrowths of needle- or plate-like crystals of rutile or sphene that cause asterism.

Treatments for spinel are generally few, with reducing the visibility of fractures by filling them

Figure 1 (above). Spinel is available in a wide range of colors, as seen in this suite of round gems weighing 1.47–6.70 ct faceted by Bill Vance. Photo by Robert Weldon/GIA; courtesy of Vance Gems.

Figure 2 (opposite page). This remarkable suite of spinel gems faceted by Bill Vance shows a wonderful range of color and transparency. The 232.9 ct rough mineral specimen gives clues to the crystal's origin, with remnants of the marble host rock preserved. The faceted red spinels range from 2.47 to 5.87 ct. Photo by Robert Weldon/GIA; courtesy of Vance Gems.

with a refractive index matching material being one most likely encountered as a form of clarity enhancement. Some spinels are also heat treated to improve clarity, but those stones are generally uncommon in the trade; they are readily detectable in a gemological laboratory using photoluminescence or visible spectroscopy, but the treatment often leaves little evidence seen in the microscope. Synthetic spinels are commonly encountered, with flame-fusion material being widely available in a broad range of colors. More technologically sophisticated materials also exist, such as flux-grown spinel. However, those examples are generally available only in red or blue gems or crystals and are relatively scarce.

This latest installment in the *G&G* chart series showcases a wide range of inclusions that a gemologist might encounter in spinel. Unlike previous charts, however, the authors also chose to highlight a few examples of spinel as an inclusion in other gem materials. Though far from comprehensive, the selected images will hopefully provide the reader with a good representation of the micro-features found in spinel.

ADDITIONAL READING

Ahline N., Smith T. (2018) Micro-World: Green crystals in yellow sapphires. *G&G*, Vol. 54, No. 1, pp. 70–71.

Altobelli M., Johnson P., Moe K.S. (2013) Lab Notes: Spinel submitted as diamond. *G&G*, Vol. 49, No. 4, pp. 254–255.

Anjomani N. (2016) Lab Notes: Synthetic sapphire and synthetic spinel doublets. *G&G*, Vol. 52, No. 4, pp. 418–419.

Blauwet D. (2011) Gem News International: Spinel from northern Vietnam, including a new mine at Lang Chap. *G&G*, Vol. 47, No. 1, pp. 60–61.

Chauvire B., Rondeau B., Fritsch E., Ressigeac P., Devidal J.L. (2015) Blue spinel from the Luc Yen District of Vietnam. *G&G*, Vol. 51, No. 1, pp. 2–17.

Cooper A., Sun Z.Y. (2014) Lab Notes: Spinel inclusion in spinel. *G&G*, Vol. 50, No. 4, pp. 297–299.

Du Toit G. (2012) Lab Notes: Bicolored spinel. *G&G*, Vol. 48, No. 4, p. 304.

Fryer C. (1991) Lab Notes: Cobalt-colored synthetic spinels with unusual inclusions. *G&G*, Vol. 27, No. 2, pp. 113–114.

——— (1991) Lab Notes: Spinel with unusual green fluorescence. *G&G*, Vol. 27, No. 2, pp. 112–113.

——— (1996) Lab Notes: Imitation spinel, an unusual assemblage. *G&G*, Vol. 32, No. 4, p. 281.

Gübelin E.J., Koivula J.I. (1986) *Photoatlas of Inclusions in Gemstones*. ABC Edition, Zurich.

——— (2005) *Photoatlas of Inclusions in Gemstones, Volume 2*. Opinio Verlag, Basel, Switzerland.

Hain M., Sun Z.Y. (2019) Gem News International: Blue gahnite from Nigeria. *G&G*, Vol. 55, No. 3, pp. 434–436.

Hughes E.B. (2018) Micro-World: Star spinel with four and six rays. *G&G*, Vol. 54, No. 2, p. 230.

——— (2020) Micro-World: Actinolite in spinel. *G&G*, Vol. 56, No. 1, p. 140.

Hughes R.W. (2020) Micro-World: Fluorophlogopite in Burmese spinel. *G&G*, Vol. 56, No. 2, pp. 293–294.

——— (2020) Gem News International: Oiled spinel. *G&G*, Vol. 56, No. 3, pp. 443–444.

Huong L.T.T., Hager T., Hofmeister W., Hauzenberger C., Schwarz D., Long P.V., Wehrmeister U., Khoi N.N., Nhung N.T. (2012) Gemstones from Vietnam: An update. *G&G*, Vol. 48, No. 3, pp. 158–176.

Inns A. (2010) Lab Notes: Synthetic spinel and synthetic ruby doublet. *G&G*, Vol. 46, No. 4, p. 307.

Johnson M.L. (1995) Lab Notes: Spinel, natural with a dendritic inclusion. *G&G*, Vol. 31, No. 1, p. 58.

——— (1995) Lab Notes: Spinel, with högbomite(?) inclusions. *G&G*, Vol. 31, No. 4, p. 272.

Johnson M.L., Koivula J.I., Eds. (1996) Gem News: Another tanzanite imitation: Synthetic spinel triplets. *G&G*, Vol. 32, No. 4, pp. 289–290.

——— (1997) Gem News: New information on flux-grown red spinel from Russia. *G&G*, Vol. 33, No. 2, pp. 151–152.

——— (1998) Gem News: Spinel from Vietnam. *G&G*, Vol. 34, No. 1, pp. 53–54.

——— (1999) Gem News: Using mineralogical techniques to solve gemological problems, Part 1: Internal "Becke lines" in spinel. *G&G*, Vol. 35, No. 1, p. 58.

Kammerling R.C., Koivula J.I., Johnson M.L, Fritsch E., Eds. (1995) Gem News: Large spinel from Tajikistan. *G&G*, Vol. 31, No. 3, pp. 212–213.

Khoi N.N., Hauzenberger C.A., Sutthirat C., Tuan D.A., Hager T., Nam N.V. (2018) Corundum with spinel corona from the Tan Huong–Truc Lau area in northern Vietnam. *G&G*, Vol. 54, No. 4, pp. 404–417.

Koivula J.I., Kammerling R.C., Eds. (1991) Gem News: Tanzanian spinel. *G&G*, Vol. 27, No. 3, p. 183.

Koivula J.I., Kammerling R.C., Fritsch E., Eds. (1992) Gem News: Chinese blue spinels. *G&G*, Vol. 28, No. 1, pp. 61–62.

——— (1992) Gem News: Blue spinel from Vietnam as sapphire imitator. *G&G*, Vol. 28, No. 2, p. 138.

——— (1992) Gem News: Update from Sri Lanka. *G&G*, Vol. 28, No. 4, pp. 260–261.

——— (1993) Gem News: Synthetic spinel from eastern Germany. *G&G*, Vol. 29, No. 2, pp. 140–141.

——— (1993) Gem News: Black spinel from Mexico. *G&G*, Vol. 29, No. 3, pp. 212–213.

——— (1993) Gem News: Spinel from Vietnam. *G&G*, Vol. 29, No. 3, pp. 213–214.

——— (1994) "Teal" blue cobalt-colored spinel. *G&G*, Vol. 30, No. 4, pp. 276–277.

Koivula J.I., Kammerling R.C., Johnson M.L., Eds. (1995) Gem News: New gem deposits in Shan State, Myanmar. *G&G*, Vol. 31, No. 4, p. 277.

Kondo D., Befi R., Beaton D. (2010) Lab Notes: Heat-treated spinel. *G&G*, Vol. 46, No. 2, pp. 145–146.

Moe K. S. (2011) Gem News International: Trapiche spinel from Mogok, Myanmar. *G&G*, Vol. 47, No. 4, pp. 329–330.

Moses T., Reinitz I., McClure S.F. (1998) Lab Notes: Spinel with a darker core. *G&G*, Vol. 34, No. 4, pp. 288–289.

Muhlmeister S., Koivula J.I., Kammerling R.C., Smith C.P., Fritsch E., Shigley J.E. (1993) Flux-grown synthetic red and blue spinels from Russia. *G&G*, Vol. 29, No. 2, pp. 81–98.

Nicastro I., Renfro N., Sun Z.Y., Palke A. (2020) Micro-World: Spinel in sapphire. *G&G*, Vol. 56, No. 3, pp. 433–434.

Overton T.W., Shen A.H. (2011) Gem News International: Cobalt

blue-colored spinel from Khuoi Ngan, Vietnam. *G&G*, Vol. 47, No. 4, pp. 328–329.
Palke A.C. (2019) Gem News International: Gray spinel—A new trend in colored stones. *G&G*, Vol. 55, No. 1, p. 130.
Palke A.C., Sun Z.Y. (2018) Symposium Proceedings: What is cobalt spinel? Unraveling the causes of color in blue spinels. *G&G*, Vol. 54, No. 3, p. 262.
Pardieu V. (2014) Hunting for "Jedi" spinels in Mogok. *G&G*, Vol. 50, No. 1, pp. 46–57.
Pardieu V., Long P.V. (2010) Gem News International: Ruby, sapphire and spinel mining in Vietnam: An update. *G&G*, Vol. 46, No. 2, pp. 151–153.
Pardieu V., Sangsawong S., Vertriest W., Raynaud V. (2016) Gem News International: "Star of David" spinel twin crystal with multiphase inclusions from Mogok. *G&G*, Vol. 52, No. 1, pp. 100–101.
Pay D. (2015) Gem News International: Exceptional red spinels and fine aquamarine. *G&G*, Vol. 51, No. 1, pp. 73–74.
Pham V.L., Pardieu V., Giuliani G. (2013) Update on gemstone mining in Luc Yen, Vietnam. *G&G*, Vol. 49, No. 4, pp. 233–245.
Raynaud V., Vertriest W. (2016) Micro-World: Etch marks, negative crystals, and etch tubes in spinel from Madagascar. *G&G*, Vol. 52, No. 3, pp. 313–314.
Renfro N., Koivula J.I. (2015) Micro-World: Violetish blue spinel in yellow sapphire. *G&G*, Vol. 51, No. 4, p. 444.
——— (2019) Micro-World: Lazurite in spinel. *G&G*, Vol. 55, No. 1, pp. 112–113.
Renfro N., Laurs B.M. (2010) Gem News International: Spinel from Bawma, Myanmar. *G&G*, Vol. 46, No. 2, p. 154.
Rizzo J. (2019) Lab Notes: Large faceted gahnospinel. *G&G*, Vol. 55, No. 1, pp. 92–93.
Saeseaw S., Khowpong C. (2016) Lab Notes: Quench-crackled blue synthetic spinel. *G&G*, Vol. 52, No. 1, p. 76.
Segura O., Lulzac Y., Fritsch E. (2012) Gems News International: True red synthetic spinel grown by a pulled technique in Russia. *G&G*, Vol 48, No. 3, pp. 232–233.
Sehgal A., Girma D. (2016) Lab Notes: Unusual yellowish green spinel. *G&G*, Vol. 52, No. 2, pp. 194–195.
Stone-Sundberg J. (2019) Gem News International: A variety of colored stones from Mayer & Watt. *G&G*, Vol. 55, No. 1, p. 139.
Verma P. (2014) Gem News International: Unusual short-wave UV reaction in synthetic blue spinel. *G&G*, Vol. 50, No. 4, pp. 312–313.
Vertriest W., Pardieu V. (2016) Update on gemstone mining in northern Mozambique. *G&G*, Vol. 52, No. 4, pp. 404–409.
Vertriest W., Raynaud V. (2017) Micro-World: Complex yellow fluid inclusion in red Burmese spinel. *G&G*, Vol. 53, No. 4, pp. 468–469.

Spinel Inclusions Chart

To purchase a laminated wall chart featuring superbly detailed photomicrographs of internal features observed in natural, treated, and synthetic spinel, go to store.gia.edu or scan the QR code on the right.

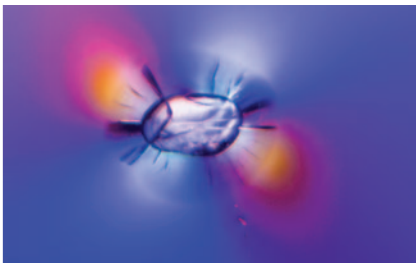

The following 25 questions are from the four 2020 issues of *G&G*. Please refer to the articles in those issues to find the single best answer for each question.

Visit gia.edu/gems-gemology to take the Challenge online. Entries must be received no later than **Monday, August 2, 2021**. All entries will be acknowledged with an e-mail.

Score 75% or better, and you will receive a certificate of completion (PDF file). Earn a perfect score, and your name also will be listed in the Fall 2021 issue of *Gems & Gemology*.

1. Which diamonds can exhibit blue luminescence after the DiamondView lamp pulse?
   - A. Natural type IIa and type Ia
   - B. HPHT laboratory-grown
   - C. CVD laboratory-grown
   - D. Natural type IIb

2. The D-to-Z color scale is applicable to diamonds that are colorless to
   - A. faint to light yellow, brown, or gray bodycolor only.
   - B. faint to light yellow or brown bodycolor only.
   - C. faint to light yellow bodycolor only.
   - D. faint to light bodycolor of any hue.

3. The Grand Mazarin diamond
   - A. is the only Mazarin diamond that has not been stolen in its history.
   - B. was sold at auction in 1887 without a correct color description.
   - C. was the largest of the Mazarin diamonds.
   - D. was sold at auction in 2017 for $4 million.

4. The absorption cross section of a chromophore is
   - A. identical for all trace elements in corundum.
   - B. inversely proportional to transmission.
   - C. the strength of the absorber.
   - D. a unitless ratio.

5. Sapphire from southern Vietnam commonly features
   - A. pyrochlore inclusions.
   - B. strong color zoning.
   - C. yellow bodycolor.
   - D. lack of silk.

6. Normal HPHT diamond growth typically produces
   - A. diamonds with less color saturation than their CVD-grown counterparts.
   - B. yellow diamonds with cape-related defects.
   - C. mostly yellow and orange diamonds.
   - D. colorless to brown diamonds.

7. The majority of D-to-Z diamonds fluoresce
   - A. blue.
   - B. green.
   - C. orange.
   - D. no discernible color.

8. C-centers in yellow diamonds
   - A. consist of aggregated pairs of nitrogen substituting for carbon.
   - B. typically show a moderate yellow reaction to long-wave UV.
   - C. are the third most common cause of color.
   - D. are stronger absorbers than cape defects.

9. Which statement about Burmese blue amber is false?
   - A. It does not display a 412 nm absorption in its UV-Vis-NIR spectra.
   - B. It sometimes shows a violet component to its fluorescence.
   - C. It generates the strongest fluorescence of the blue ambers.
   - D. It tends to have a richer yellow color.

10. If a particular corundum chromophore has a larger visible-range peak absorption cross section than the other chromophores
    A. the same ppma concentration is needed for the same depth of color.
    B. a higher ppma concentration is needed for a deeper color.
    C. a lower ppma concentration is needed for a deeper color.
    D. None of the above. The concentration level needed for a given depth of color depends on the illumination.

11. For the portion of Marie Antoinette's jewels sold in 2018 by Sotheby's, what aided in cataloging the collection?
    A. Marie Antionette's daughter Marie Thérèse preserved the original inventory.
    B. The 1907 and 1932 inventories of Marie Anne, Archduchess of Austria.
    C. An 1887 inventory from the French Ministry of Finance.
    D. Cardinal Mazarin's will.

12. For a uniaxial crystal, the E⊥c absorption spectrum corresponds to light traveling through the crystal
    A. in a direction halfway between parallel and perpendicular to the c-axis.
    B. perpendicular to the c-axis.
    C. in any direction.
    D. parallel to the c-axis.

13. Monazite in pink sapphire heated to 800°C will
    A. develop tension fractures.
    B. become near-colorless.
    C. not change at all.
    D. turn brown.

14. During Peter Rainier's oversight of Chivor, the mine was
    A. between break-even and losing money.
    B. safer than it had ever been.
    C. under no legal disputes.
    D. highly profitable.

15. Which mussel produces the most desirable beads for akoya pearl farming in Vietnam?
    A. Washboard
    B. Maple leaf
    C. Ebony
    D. Pig-toe

16. Jade carvings exhibiting very thin translucent areas
    A. have only been accomplished in the modern era.
    B. are categorized as eggshell carving.
    C. require motor-driven tools.
    D. are known as "Qiaose."

17. Rose-cut colored stones from the seventeenth century
    A. always display six-fold symmetry.
    B. were predominantly found to have drill holes.
    C. have many patterns distinct from same-era diamonds.
    D. were exclusively cut from quartz, garnet, sapphire, and peridot.

18. Turquoise with a raindrop pattern
    A. potentially owe their distinctive appearance to leaching and weathering.
    B. is the dominant pattern found in turquoise coming from Hubei, China.
    C. show less fluorapatite in the "raindrops" versus the substrate portion.
    D. had enriched levels of iron, vanadium, and nickel in the raindrops.

19. In the application of isotopes to determining the geographic origin of gems such as nephrite, the isotopic fractionation factor
    A. is independent of temperature.
    B. is dependent solely on the formation process.
    C. is a fraction of the isotopic ratios of two coexisting phases.
    D. of a measured phase is always greater than that of the IAEA standards.

20. Yellow color in beryl is attributed to
    A. a broad Fe^{2+} or Fe^{2+}-Fe^{3+} related absorption around 600 nm.
    B. the Fe^{3+} absorption edge shifting to longer wavelengths.
    C. high type II water contents.
    D. the presence of Cr^{3+}.

21. Compared to Russian emeralds, those from Swat Valley, Pakistan
    A. have higher lithium, cesium, and rubidium contents.
    B. have higher chromium, vanadium, and iron contents.
    C. have distinctly different inclusions.
    D. are much more inclusion-free.

22. The absence of the 3232 cm^{-1} peak in the FTIR spectrum of a pink sapphire
    A. indicates radiation damage.
    B. is inconclusive for determining no treatment.
    C. is conclusive of low temperature heat treatment.
    D. means that the 3309 cm^{-1} absorption coefficient peak is over 0.040 cm^{-1}.

23. What information did Francisco Restrepo most likely have in his quest to rediscover the Somondoco emerald mines?
    A. A 300-year-old description of a view of great plains to the east of the mines
    B. Maps from Pedro Fernández Valenzuela's journey to the mine in 1538
    C. A book from Joaquin Acosta's library, loaned to him by Fritz Klein
    D. The mines were never truly lost—he was taken to them by locals.

24. What results from the application of an optical brightening agent to a white pearl?
    A. The fluorescent spectrum of the pearl will shift to shorter wavelengths.
    B. The external color appearance of the pearl will remain the same.
    C. The pearl will fluoresce more red light than before.
    D. The pearl's luster will decrease.

25. Which trace element is absent from Swiss rhodonite but present in other major sources of this mineral?
    A. Manganese
    B. Titanium
    C. Calcium
    D. Iron

To take the Challenge online, please scan the QR code above.

Lab Notes

Editors
Thomas M. Moses | Shane F. McClure

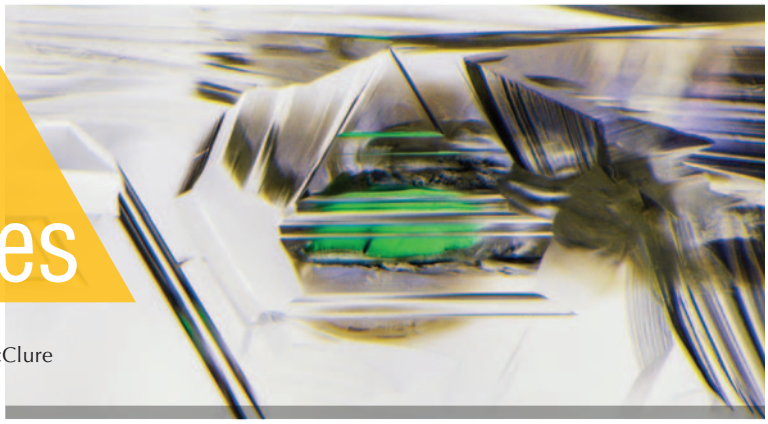

DIAMOND

Asterism in Natural Diamond Cabochons

The New York laboratory received two cabochon diamonds from Hong Kong, both displaying asterism. Gemologists initially questioned whether these stones were in fact diamond because of the cabochon cutting style and the white four-rayed "stars" observed using fiber-optic illumination. The polished cabochon is a popular cutting style in colored stones but rarely attempted with diamond due to its hardness. This cutting and polishing technique yielded two semitransparent to translucent round cabochon diamonds with a very light yellow color, weighing approximately 6.29 ct and 6.07 ct (figure 1).

Mid-infrared spectroscopy revealed strong hydrogen-related absorption bands (e.g., 3107 cm^{-1}) and those attributed to aggregated nitrogen in the one-phonon region, evidence of natural type Ia diamonds (figure 2). Microscopic observation from the base of the cabochons revealed prevalent clouds distributed throughout the diamonds. The clouds were composed of small whitish pinpoints, and when aligned linearly formed small needle-like internal inclusions (figure 3). Fluorescence images collected using the DiamondView revealed yellowish green fluorescence in the sectors with clouds. The cloud-free sectors were inert to UV radiation. Symmetrical fluorescence patterns were observed in both stones with nearly mirror images (figure 4).

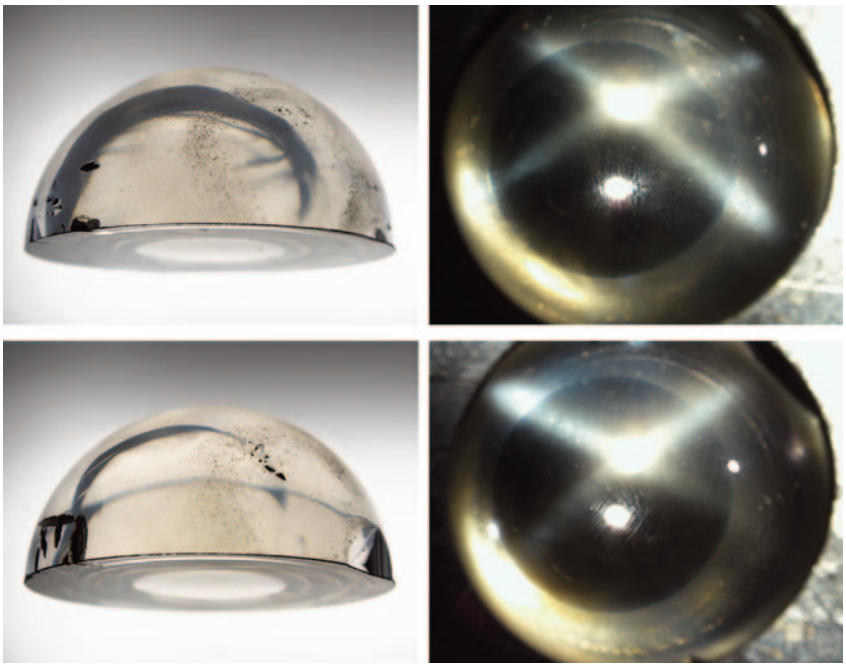

Figure 1. Photos show internal cloud inclusions in profile view (left) and asterism in top view of the polished cabochons using fiber-optic illumination (right). The diameters of the two cabochons are 11.33 mm (top) and 11.32 mm (bottom).

Natural diamonds are dominated by {111} octahedral growth sectors, but occasionally the {100} cubic sector is well developed, forming a crystal with mixed growth habits. The cubic growth sector could preferentially contain a significant amount of pinpoint cloud inclusions. This feature occurs quite often in diamonds from Zimbabwe. Unlike other diamonds with clouds, these clouds concentrated in the {100} growth sectors linearly aligned to form needle-like inclusions. The distribution of these needle-like inclusions within the {100} growth sectors generated the asterism feature seen in these gem diamonds.

Gemological and spectroscopic

Editors' note: All items were written by staff members of GIA laboratories.

Gems & Gemology, Vol. 57, No. 1, pp. 52–62.

© 2021 Gemological Institute of America

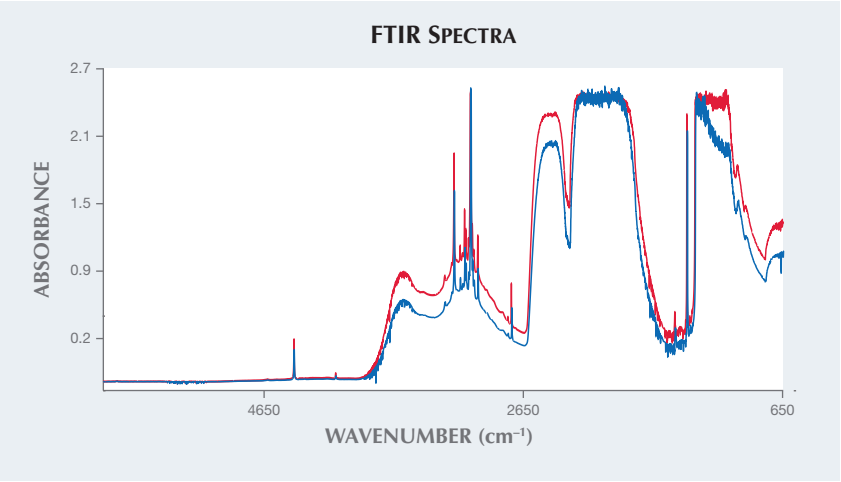

Figure 2. FTIR spectra reveal natural type Ia diamonds with strong hydrogen concentrations in the 3000–4000 cm^{-1} region and aggregated nitrogen in the one-phonon region at 1400–800 cm^{-1}. The 6.29 ct diamond cabochon spectrum is denoted in red and the 6.07 ct diamond in blue.

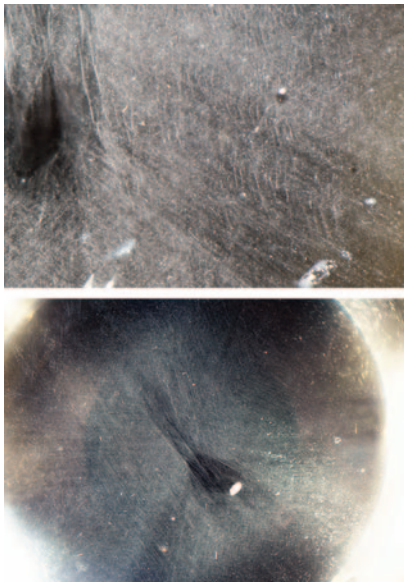

Figure 3. Cloud and needle-like inclusions observed in bottom view of the two very light yellow round cabochon diamonds: 6.29 ct (top, field of view 1.8 mm) and 6.07 ct (bottom, field of view 6.5 mm).

features strongly indicated that these diamonds were cut from the same large rough diamond crystal. The crystal was very likely cut through the center along the (100) plane and then polished into two relatively large cabochon diamonds. Taking advantage of the widespread needle-like inclusions in this otherwise well-included large diamond crystal was a clever design choice to produce two cabochons displaying the rare asterism phenomena.

Erica A. Watts

Bicolor Rough Diamond Crystals

The GIA laboratory in Antwerp regularly receives pink diamond crystals for examination as part of the Diamond Origin Report. This recent service has allowed GIA researchers to study a greater number of rough diamonds in addition to their faceted counterparts. Two crystals, weighing 1.75 and 1.44 ct and both reportedly from Australia, were among those submitted. These were considered quite interesting, as they contained colorless and pink sections with distinct boundaries (figure 5).

The color in the vast majority of naturally pink diamonds is attributed to a broad absorption band at about 550 nm within the visible absorption spectrum. This band generally results from distortion of the crystal lattice from plastic deformation due to stress after crystal growth. However, much remains unknown about the actual formation and configuration of this feature. Therefore, these two crystals provide a unique chance to study natural diamond formation and the origin of pink color in greater detail.

The pink section of both analyzed samples likely experienced great stress in order to undergo the plastic deformation necessary to impart the pink color. The colorless sections were not similarly deformed so presumably they represent a different and later growth event (figure 6).

Visible-NIR absorption spectra collected from the pink and near-colorless sections of the diamonds show differences in the 550 nm region. Observed in the spectrum for the pink

Figure 4. DiamondView images of the very light yellow round cabochon diamonds reveal the location of asterism using ultra-short-wave illumination, approximately 225 nm. The top view is shown on the left in each pair of images, the bottom view on the right.

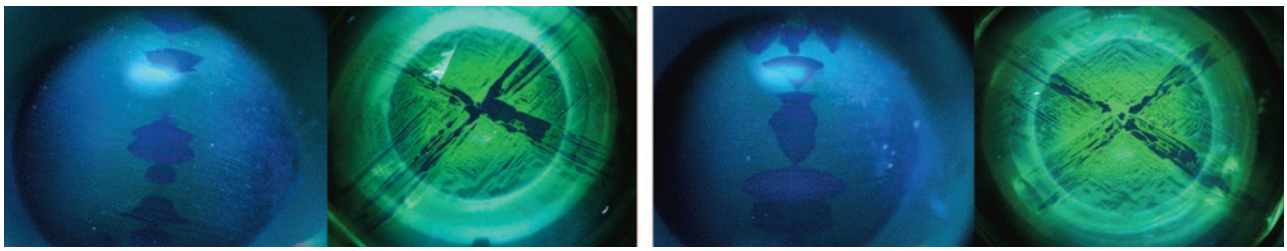

Figure 5. These two rough diamond crystals (1.75 ct on the left and 1.44 ct on the right) are rare examples of diamonds showing both pronounced pink and colorless sections. Field of view 10.8 mm (left) and 7.4 mm (right).

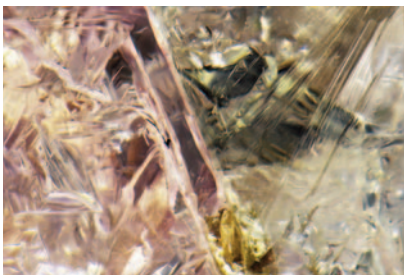

Figure 6. A close-up image of the 1.44 ct diamond crystal shows the boundary between the pink (left) and colorless (right) sections. Field of view 3.16 mm.

portion is the expected absorption at 550 nm, while the spectrum for the colorless portion shows a lack of absorption (figure 7, left).

For the 1.44 ct crystal, we also collected infrared (IR) absorption spectra and photoluminescence (PL) spectra from both the pink and the colorless sections using 455 and 532 nm laser excitation wavelengths. The IR absorption spectra for both sections indicate type Ia diamonds with saturated concentrations of nitrogen. Due to this saturation, it was not possible to determine the total nitrogen content or the ratio of the A and B nitrogen centers, which could have helped in further distinguishing these two sections.

Within the PL spectra, the peak widths for the diamond Raman peak and the H3 peak were comparable in both the pink and colorless sections. Additionally, a PL peak at 676 nm was detected in both sections; although its configuration is unknown, it was documented previously in other rough pink diamonds (E. Gaillou et al., "Spectroscopic and microscopic characterizations of color lamellae in natural pink diamonds," *Diamond and*

Figure 7. Left: Vis-NIR absorption spectra for the 1.44 ct crystal collected from the pink and colorless sections. The 550 nm absorption band is prominently visible within the pink section. The spectra are stacked for clarity. Right: PL spectra with 532 nm excitation of the 1.44 ct crystal show a ~600–730 nm emission band collected from the areas of pink banding, which was not detected from the colorless section—this luminescence band has previously been linked with the 550 nm absorption band. The diamond Raman peaks are scaled as equal.

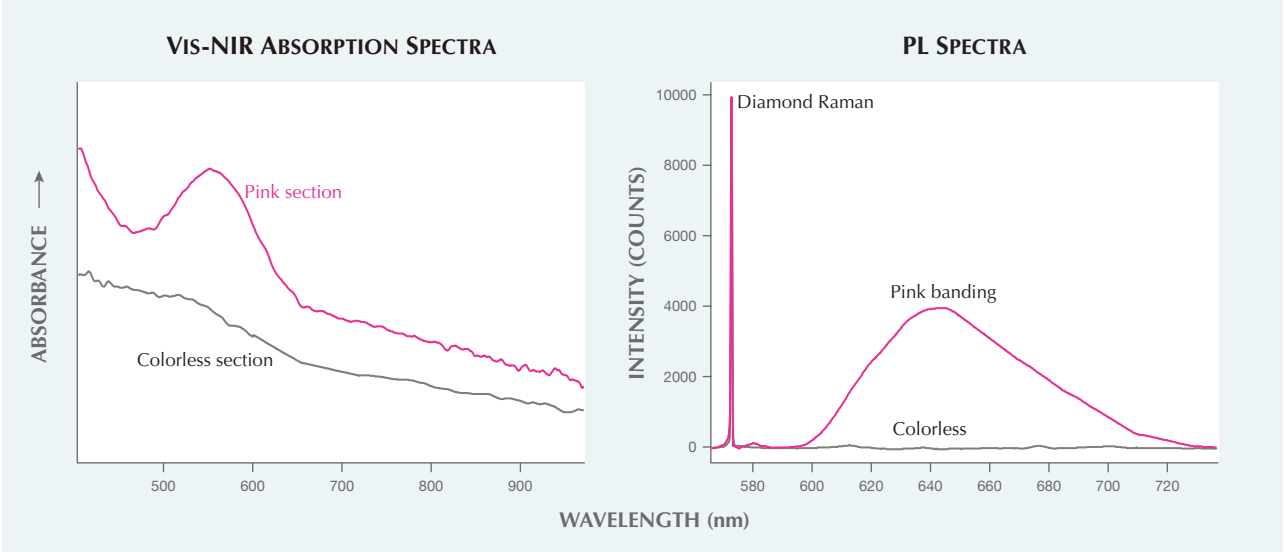

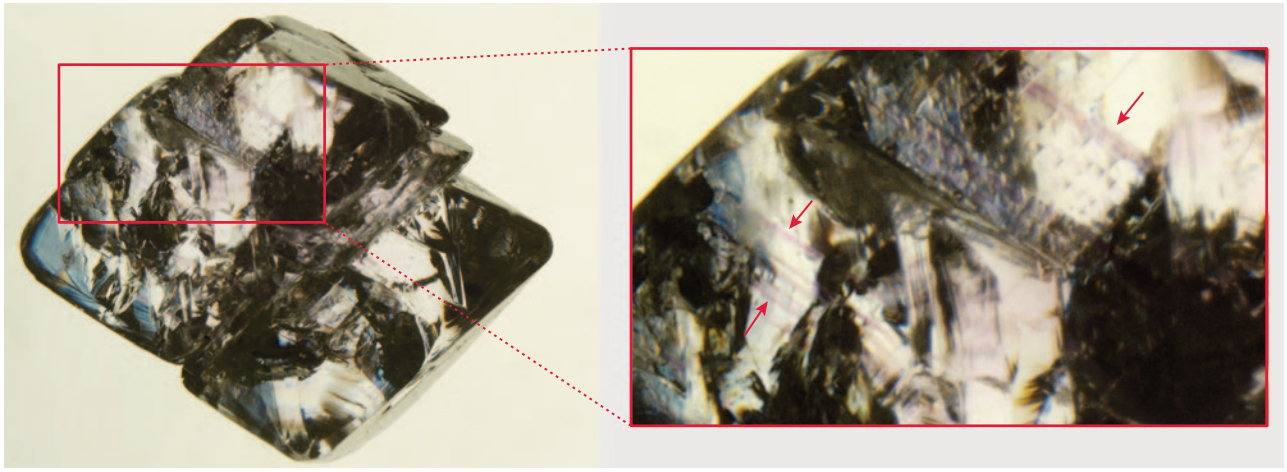

Figure 8. The 1.44 ct crystal was immersed in methylene iodide to reveal additional details. The red arrows within the inset (field of view 3.4 mm) indicate the pink banding.

Related Materials, Vol. 19, No. 10, 2010, pp. 1207–1220). The other notable feature detected by PL mapping was a broad (~600–730 nm) emission band (figure 7, right) that coincided with the pink banding revealed by immersion in methylene iodide (figure 8). Its detection is consistent with other pink diamonds and likely related to the 550 nm absorption band (e.g., S. Eaton-Magaña et al., "Comparison of gemological and spectroscopic features in type IIa and Ia natural pink diamonds," *Diamond and Related Materials*, Vol. 105, 2020, p. 107784).

As natural pink diamonds are quite rare, finding two examples of such bicolor crystals that show these distinct pink and colorless sections is an extraordinary find.

Sally Eaton-Magaña, Paul Johnson, Ellen Barrie, and Michaela Hariňová

Rare Faceted HEXAGONITE

A saturated pinkish purple hexagonite (figure 9) was recently examined at the Carlsbad laboratory. Standard gemological testing revealed a refractive index of 1.599–1.629 and a specific gravity of 2.97 obtained hydrostatically. Microscopic examination showed needle-like inclusions and iridescent cleavage cracks (figure 10). When observed with a dichroscope, pleochroic colors of pink,

Figure 9. This 3.27 ct pinkish purple hexagonite is the largest example examined by the authors. Courtesy of Vance Gems.

Figure 10. Iridescent cleavage cracks and needle-like structures were present in the faceted hexagonite. Field of view 3.50 mm.

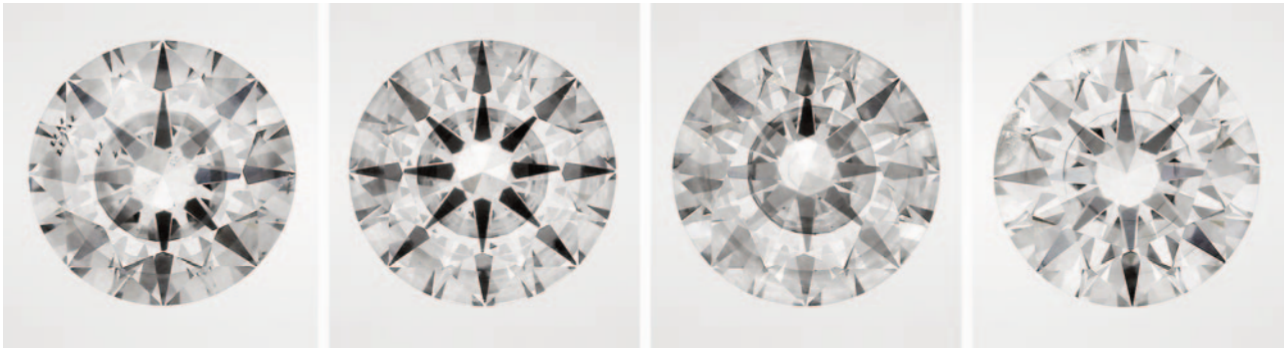

Figure 11. Face-up images of four CVD laboratory-grown diamonds with an eye-visible growth plane. These four diamonds range from 1.81 to 2.51 ct.

orangy pink, and violet were observed. These results were consistent with the mineral tremolite. The pinkish purple variety of tremolite is recognized as hexagonite, which owes its color to manganese. Hexagonite was once thought to be a hexagonal form of tremolite, which is how its name was derived, but was later confirmed to be monoclinic (Summer 1985 Gem News International, p. 110).

This particular stone was faceted by Bill Vance of Vance Gems, who sourced the rough that was reportedly from the original type locality, the Balmat-Edwards zinc mining district in St. Lawrence County, New York. Hexagonite is also found at the town of Fowler in St. Lawrence County. The saturated pinkish purple color and large size make this rare stone an exceptional example of this material. While very few faceted hexagonite gems have been tested at GIA, this 3.27 ct stone is the largest one examined by the authors.

Amy Cooper and Nathan Renfro

Prominent Growth Planes Observed in HPHT-Processed CVD LABORATORY-GROWN DIAMONDS

The laboratory-grown diamond industry is ever evolving and improving. With state-of-the-art growth and treatment technology, high-quality CVD diamonds, in terms of clarity and color, are now commonly seen on the consumer market. Laboratory-grown diamonds are occasionally submitted for natural diamond grading services, and recently GIA's Hong Kong laboratory received a total of 43 undisclosed CVD-grown diamonds treated by high pressure and high temperature (HPHT), ranging from 0.70 to 2.63 ct in weight, from the same client. Laboratory-Grown Diamond Reports were issued for these synthetics, which received E–I color grades and VVS_2–I_2 clarity grades.

Four samples had a very eye-catching feature—a dark circle or ring at the center when viewed face-up without magnification. The ring appeared to be a thick grayish layer at the culet when viewed from the pavilion (figure 11). As the extraordinary feature looked shiny and resembled the separation plane often observed in assembled stones, questions about the true identity of these samples were raised.

Figure 12. Visible planes with different textures: fine clouds (top left, field of view 3.83 mm) and wave ripples (top right, field of view approximately 3 mm). Colorless "holes" observed in a ripple-like plane under the microscope (bottom left, field of view 3.83 mm) and in immersion (bottom right). The blue color in the top left photo is due to a different white balance to emphasize the texture.

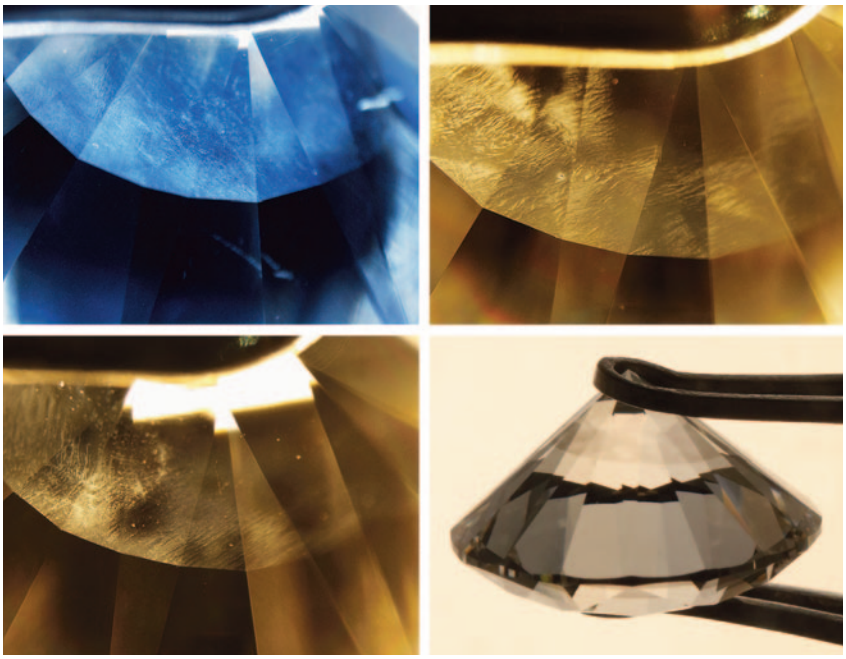

Microscopic examination of these four samples revealed some interesting findings. There was a textured plane almost parallel to the table facet, each with a different appearance (figure 12): fine clouds all the way across; ripple-like waves with some "holes" (colorless areas); a mixture of both; and a ripple-like plane that was not visible all the way around. An additional 26 samples had visible grayish/brownish planes either at the pavilion, which were much less prominent, or at the pavilion viewing through the table. Eight of these additional samples had a plane at an angle to the table facet. The plane appeared as a line with no color difference when immersed in water and viewed in a parallel direction to the growth plane. All 43 samples generally showed a banded and cross-hatched strain pattern when viewed with crossed polarizers (figure 13).

Spectroscopic analysis of the 43 samples yielded very similar results. They were either type IIa or type IIb and had a very strong silicon vacancy doublet peak (736.5 and 736.9 nm) in their photoluminescence spectra, typical of CVD-grown diamonds. PL spectra were also collected at the table and at the pavilion somewhere between the growth plane and the culet for the samples with a very prominent growth plane, but the data did not show any critical differences. The most diagnostic test was DiamondView imaging, as all 43 displayed very distinct growth layers (figure 14). It also revealed the HPHT treatment history that the CVD diamonds had experienced.

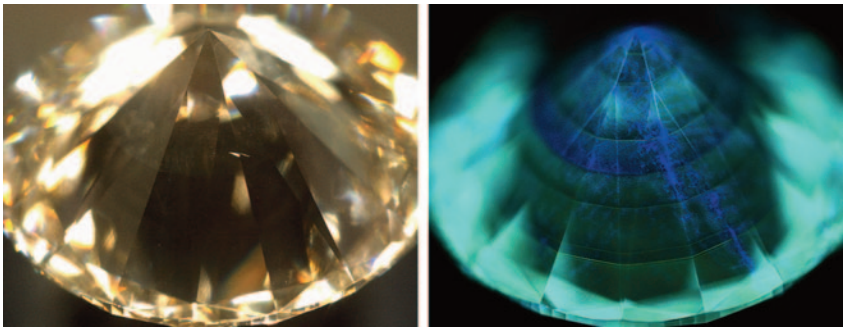

Figure 14. DiamondView imaging provided evidence of CVD growth.

The uniformity of the growth layers observed in DiamondView imaging and under crossed polarizers, together with the immersion test, showed no evidence of assembly and therefore excluded the possibility of a doublet. The color making the growth plane visible is believed to come from the non-diamond carbon deposited between two growths. It could not be removed by the post-growth HPHT treatment.

Billie Pui Lai Law, Ka Wing Tam, and Nick Ka Chun Chan

OPAL

Cat's-Eye Opal

Precious opal characteristically shows a spectacular play-of-color effect and may also display cat's-eye or star phenomena produced by the internal structure (e.g., Winter 1990 Gem News, p. 304; Spring 2003 Lab Notes, pp. 43–44; Summer 2014 Lab Notes, pp. 152–153). Chatoyancy and asterism in opal are quite rare, however, because opal is a hydrated silica and has no repeating crystal lattice (J.V. Sanders, "The structure of star opals," *Acta Crystallographica*, Vol. A32, 1976, pp. 334–338). The keys to creating and maximizing chatoyancy in opal is careful arrangement of the play-of-color patches, orienting the "brushstrokes" (stripe structure caused by misalignment of the tiny silica spheres producing play-of-color), and good cutting.

Recently, GIA's Tokyo laboratory had an opportunity to examine a transparent double cabochon measuring 12.65 × 10.06 × 5.70 mm and weighing 3.79 ct. It showed blue to green play-of-color against a gray background as well as a distinct chatoyancy (figure 15). Standard gemological testing gave a specific gravity of 2.13

Figure 13. A banded strain pattern seen across the visible plane. Field of view 11.45 mm.

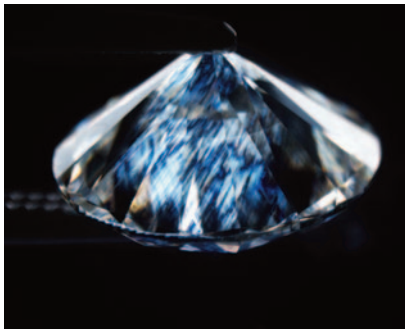

Figure 15. This 3.79 ct gray transparent opal shows dominant blue play-of-color with a distinct chatoyancy.

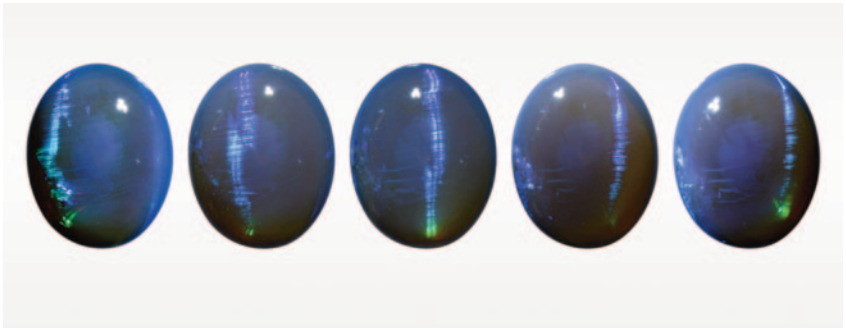

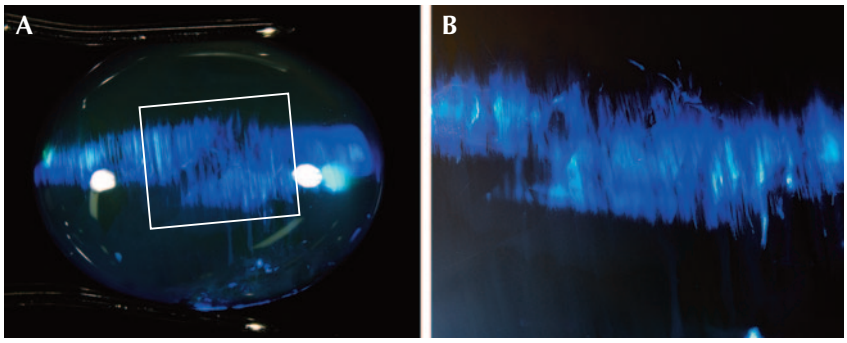

Figure 16. Chatoyant effect caused by light reflecting off parallel brushstroke patterns within play-of-color patches. A: This opal contained several large play-of-color patches with parallel brushstrokes. B: A close-up of the brushstroke pattern seen in the white square in (A). Field of view 13.3 mm (A) and 5.60 mm (B).

and a spot RI reading at 1.45, suggesting that the stone was opal. The brushstroke pattern within play-of-color patches and the strong bluish white fluorescence and phosphorescence after exposure to ultraviolet light were consistent with a natural origin. Advanced testing using Fourier-transform infrared spectroscopy (FTIR) also indicated that this was natural opal with no evidence of polymer impregnation and/or sugar treatment (G. Brown, "Treated Andamooka matrix opal," Summer 1991 *G&G*, pp. 100–106). This opal had no synthetic features such as "snake skin" and "columnar structure" in any direction. There was no evidence that this stone was assembled.

In microscopic observation, this opal contained several large blue to green play-of-color patches with parallel brushstroke patterns. The brushstrokes in each patch were mostly perpendicular to the length of the stone and parallel to each other, and the light reflection from the pattern created a distinct chatoyant effect (figure 16). Because the opal was composed of large blue dominant play-of-color patches, the parallel brushstrokes and the high-dome cabochon shape produced a distinct chatoyancy against the gray background. This was a striking example of cat's-eye precious opal.

Makoto Miura and Yusuke Katsurada

Figure 17. Opal with unusual aventurescence, seen with fiber-optic lighting.

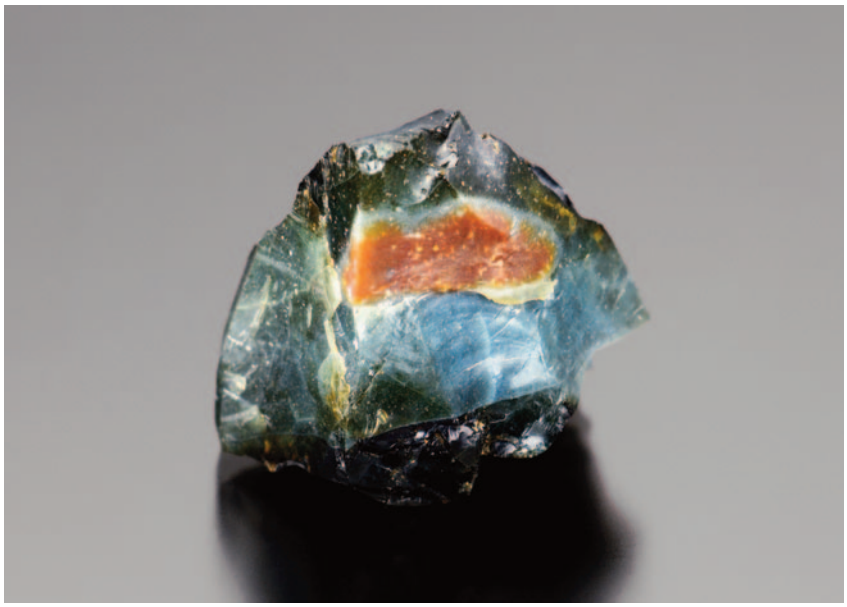

Green Opal Displaying Aventurescence

Recently the Carlsbad laboratory received a variegated dark green and blue partially polished rough stone for identification services. The stone measured 23.64 × 20.13 × 15.52 mm and weighed 23.74 ct (figure 17). A vitreous to waxy luster and bright yellow inclusions were observed.

Standard gemological testing revealed a refractive index spot reading of 1.43 and a specific gravity of 2.15 obtained hydrostatically. These properties were consistent with opal. During microscopic analysis, fine hazy clouds and turbidity were seen within the structure, as well as a reddish brown portion with iron staining. Although no play-of-color was observed, an unusual aventurescence was seen in several areas with fiber-optic lighting while rotating the stone. This unusual phenomenon was caused by the scattering of light from the small, eye-visible yellow inclusions (figure 18). These inclusions were later confirmed by Raman spectroscopy as pyrite.

Figure 18. Scattered inclusions in the green opal were identified by Raman spectroscopy as pyrite. Field of view 1.79 mm.

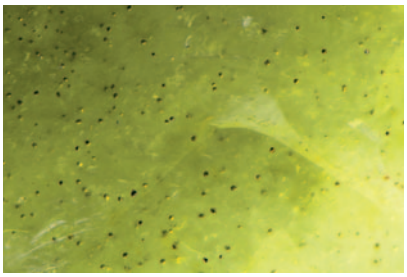

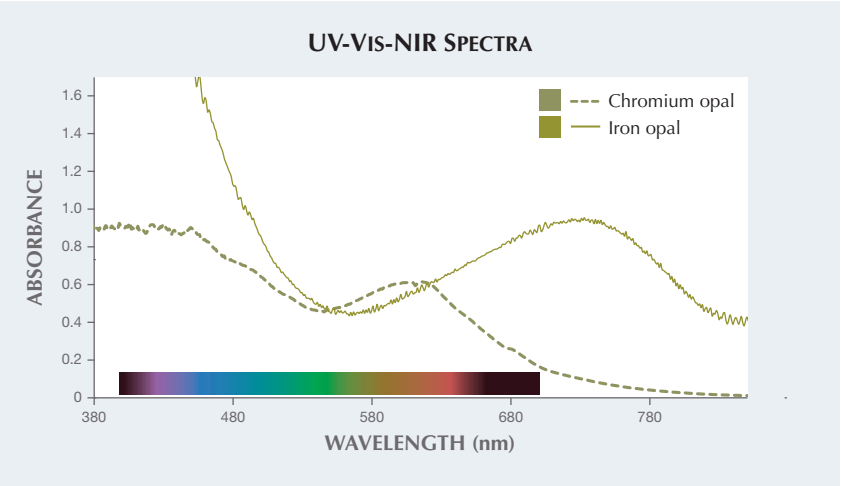

Figure 19. The spectra of the two types of opal were measured and renormalized for comparison with each other with similar lightness (see corresponding color panels in table 1). The solid line represents iron opal. The broad absorption band centered at 741 nm is likely caused by interstitial Fe^{2+}. The dashed line represents chromium opal. The smaller absorption band centered at around 600 nm is caused mainly by Cr^{3+}.

LA-ICP-MS analysis was performed on the sample to investigate which chromophore was responsible for its green color. The results showed that the stone contained approximately 3540 ppma Fe. No other chromophoric trace elements were measured in significant quantities, indicating that iron was most likely the cause of the green color. UV-Vis-NIR spectra were collected and used to quantitatively calculate the color of this material (figures 19 and 20, table 1). In figure 19, a broad absorption band centered at about 741 nm produces the green color of the opal. This absorption band is likely related to octahedral Fe^{2+}. Previous publications have shown that iron can produce green color in quartz due to an absorption band centered at 741 nm relating to interstitial Fe^{2+} (L.B. Hebert and G.R. Rossman, "Greenish quartz from the Thunder Bay amethyst mine panorama (TBAMP), Thunder Bay, Ontario, Canada," *Canadian Mineralogist*, Vol. 46, No. 1, 2008, pp. 111–124). Octahedral Fe^{2+} can strongly absorb red, orange, and some portion of yellow light of the visible spectrum to produce a transmission window in the yellowish green region. In this case, a transmission window around 570 nm results in the green color in the iron opal (solid line in figure 19). The presence of some additional Fe^{3+} cannot be ruled out and may contribute to the rise in absorption at shorter wavelengths into the UV region.

Another type of green opal colored by Cr^{3+} (Winter 2020 Lab Notes, pp. 520–521) was compared with the iron-colored opal (solid line in figure 19). Cr^{3+} produces a smaller absorption band centered at about 600 nm, leading to a transmission window in the green region around 540 nm that causes a less yellow and more pure green color (figure 19). The two color panels calculated from the two spec-

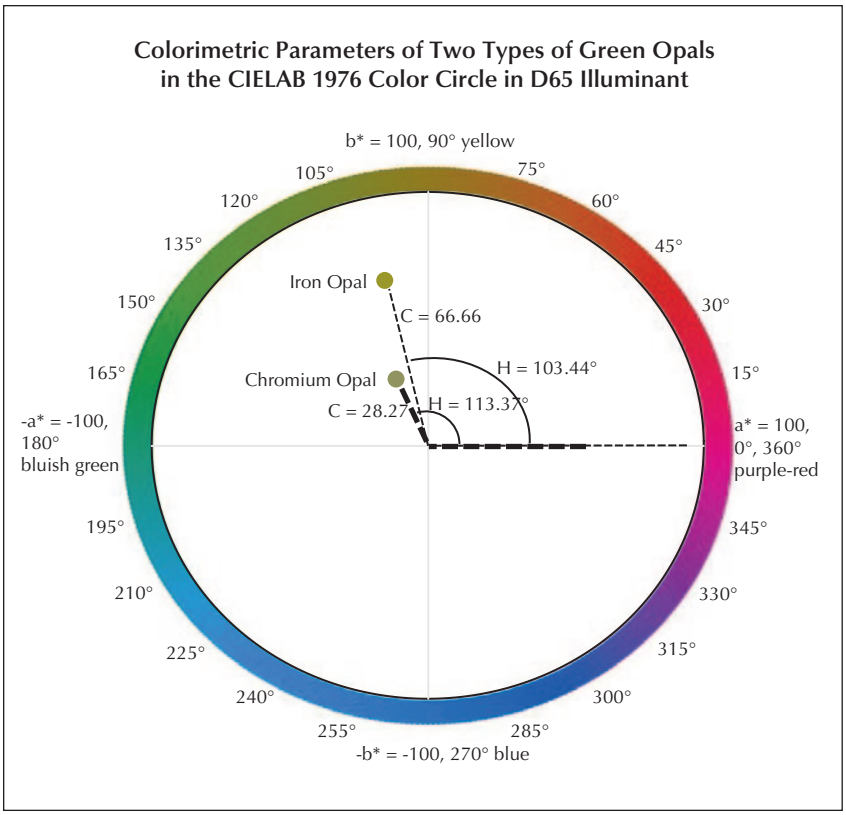

*Figure 20. Color panels corresponding to the two spectra were plotted in the CIE L*a*b* 1976 color circle. The color of the iron opal, looking more yellowish and saturated, has a smaller hue angle and larger chroma than the color of the more greenish and less saturated chromium opal. Both calculated color panels have similar lightness for comparison (table 1).*

TABLE 1. CIE and RGB color coordinates calculated from the two opal spectra in figure 19 under CIE D65 illumination.

Iron opal				Chromium opal			
D65	L*	a*	b*	D65	L*	a*	b*
	60.17	-15.49	64.84		60.90	-11.21	25.95
	L	C	H		L	C	H
	60.17	66.66	103.44		60.90	28.27	113.37
	X	Y	Z		X	Y	Z
	0.23	0.28	0.04		0.25	0.29	0.17
	R	G	B		R	G	B
	148.68	150.50	0.00		144.05	151.41	100.55

tra were also plotted in the CIE L*a*b* 1976 color circle seen in figure 20. This allows for a more accurate comparison between the two color panels using quantitative colorimetric data. In the plot, the hue angle of the iron opal is smaller than chromium opal, resulting in a more yellowish green hue. The chroma of the iron opal is larger than that of a chromium opal with similar lightness, resulting in a more saturated color.

This green common opal is a clear example of iron contributing to the yellowish green color, in contrast to the more pure green color due to the chromium in the opal previously documented with a slightly grayish green color. Both the yellowish green color and pyrite inclusions are consistent with an iron-rich environment. The pyrite inclusions also add a unique display of aventurescence not typically seen in common opal.

Amy Cooper, Ziyin Sun, Philip York, and Aaron Palke

Natural Fossil PEARLS and Shell Blister from the Coast of Florida

Fossilized shells and pearls represent a unique group of specimens that are occasionally submitted to GIA, as reported in *G&G* previously (Winter 2015 Lab Notes, pp. 432–434; Spring 2020 Lab Notes, pp. 136–138). Those fossil samples were usually brownish in color and fully petrified, lacking any surface structures and associated luster or overtones that once belonged to them. However, two cream-colored fossil pearls (along with a fossil shell containing a shell blister; figure 21) recently submitted to GIA's New York laboratory completely changed our earlier impressions.

The two semi-baroque-shaped pearls measuring approximately 12.64 × 11.50 × 10.00 mm (weighing 8.64 ct) and 13.08 × 11.45 × 10.18 mm (weighing 9.48 ct) exhibited a dry, chalky appearance that would be expected for such old samples, with cracks and parasite holes (figure 22, right) detectable by visual observation. More remarkably, some surface areas had delicate nacre layers showing fine nacre platelet structures and displaying subtle iridescence effect, which could be considered as orient in nacreous pearls (figure 22). EDXRF analysis detected low concentrations of manganese and high concentrations of strontium, typical for marine mollusks. Raman spectroscopy identified the composition of the materials as aragonite. Microradiography revealed internal concentric and arc growth features, which confirmed their natural origin. Out of curiosity and due to the very good condition of the two pearls, we

Figure 21. Three fossilized specimens recently submitted to GIA's New York laboratory: two fossil pearls (12.64 × 11.50 × 10.00 mm and 13.08 × 11.45 × 10.18 mm, left and right, respectively) and a fossil shell (45.97 × 32.03 × 10.90 mm) containing a shell blister. Courtesy of Kathryn Malatino and Aaron Brown.

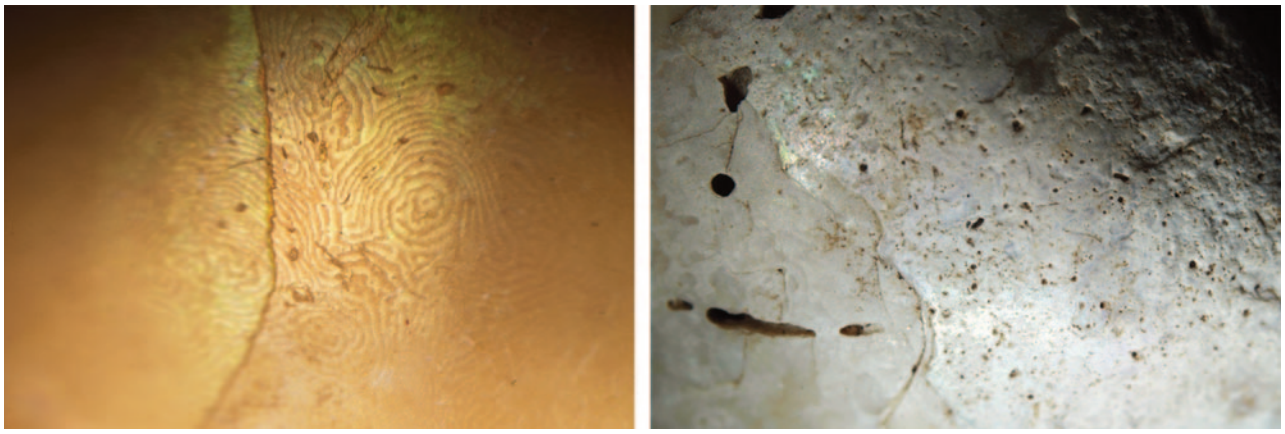

Figure 22. Nacreous spiral platy structures, parasite tunnels, and orient effects were observed on the surfaces of the two fossil pearls. Field of view 1.5 mm (left) and 5.9 mm (right).

further extracted a small amount of powder from the surface of one pearl and sent it to the Accelerator Mass Spectrometry Lab at the University of Arizona for radiocarbon dating analysis. The dating work resulted in a $\delta^{13}C$ value of –0.8 ‰, proving the sample to be very old. The fraction of modern carbon is less than 0.0024, indicating that the age of the sample was beyond the limit of radiocarbon dating (>48,500 years), though the actual age is unknown. This result proved that the sample could be categorized as fossilized material.

The shell that was submitted along with the two fossil pearls looked more petrified but also remained relatively intact, with obvious ridges (or scutes) on the back of the shell and a shallow cream-colored "bump" on the inner side that could best be described as a shell blister. According to the owner, these fascinating specimens were found off of the west coast of Florida near St. Petersburg, approximately 25–50 feet below the sediment during dredging, along with many more shells of various kinds and even fossilized shark teeth.

The two natural fossil pearls and the shell blister created by Mother Nature have been well preserved. They provided unique insights into ancient mollusks and their associated pearls or related materials.

Chunhui Zhou

Lead Glass–Filled LABORATORY-GROWN RUBY

The GIA lab in Carlsbad received for identification a lead glass–filled laboratory-grown ruby (figure 23). We commonly see glass-filled natural rubies, but to our knowledge only one other laboratory-grown example has ever been submitted.

This transparent to semi-transparent oval mixed cut weighed 3.53 ct and showed gemological properties of ruby: a refractive index of 1.761–1.769, a birefringence of 0.008, a specific gravity of 4.01, a uniaxial optic figure, and a characteristic ruby spectrum using a handheld spectroscope.

Examination of the stone under magnification showed a network of interconnected fractures. A pronounced blue and orange flash effect was observed throughout, proving the fractures were filled with lead glass. Also present in the fractures were dendritic patterns and coarse flattened gas bubbles (figure 24). No inclusions

Figure 23. This 3.53 ct laboratory-grown ruby was treated with lead-glass filling.

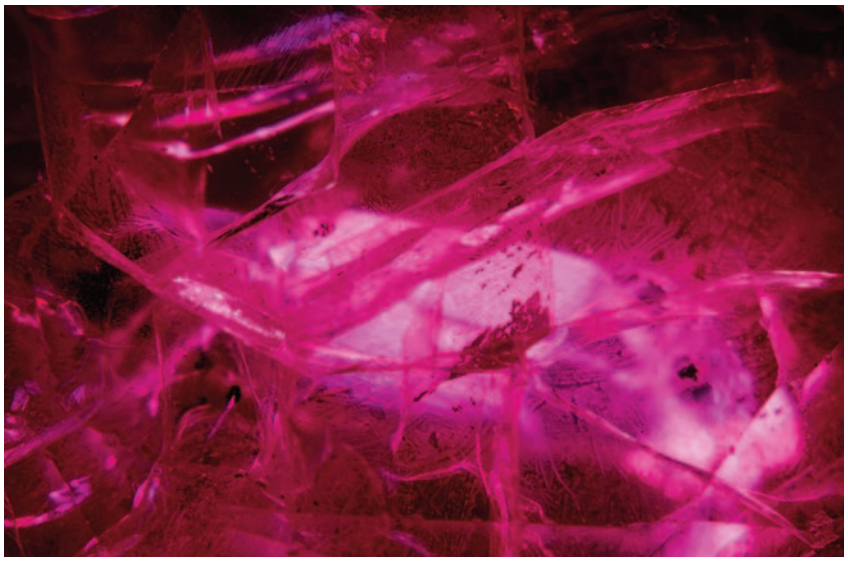

Figure 24. Magnification of the internal structure of the synthetic ruby; both high-relief trapped gas bubbles and blue and orange flash effects were observed in the stone. Field of view 7.19 mm.

were observed to indicate the natural or synthetic origin of the corundum. However, this stone exhibited strong red fluorescence to long-wave ultraviolet and medium chalky (bluish white) red short-wave ultraviolet fluorescence. Chalky SWUV is typical of heated ruby and sapphire. But when viewed in synthetic pink sapphire and synthetic ruby, it generally makes it more difficult to observe diagnostic curved striae in the stone. In our sample it was much harder, since that effect was combined with interference from filled fractures.

In these cases, a stronger SWUV light source may prove helpful. The curved growth lines were seen as chalky luminescent bands in the DiamondView, proof of its laboratory-grown origin (figure 25).

Lead-glass filling of corundum is based on the same principle applied to emerald and diamond: the use of a filling material with an RI very close to that of the host material, to minimize the appearance of fractures. The treatment is very effective, and the clarity of very low-quality material can be improved, rendering it usable in jewelry. This makes it possible to market a great deal of previously unsalable material. Fortunately, this treatment is easily detected with magnification. The identifying characteristics are very low-relief fractures, flattened and rounded gas bubbles and voids (unfilled areas) in fractures, and a blue and orange flash effect (S.F. McClure et al., "Identification and durability of lead glass–filled rubies," Spring 2006 *G&G*, pp. 22–33). This stone displayed an orange and blue flash effect (again, see figure 24) as well as gas bubbles trapped in fractures that were conclusive evidence for lead-glass filling of the fractures in this synthetic ruby. While it is unclear why anyone would go to the trouble to treat a synthetic ruby with lead-glass filling, gemologists should be aware that such material does exist in the trade.

Forozan Zandi

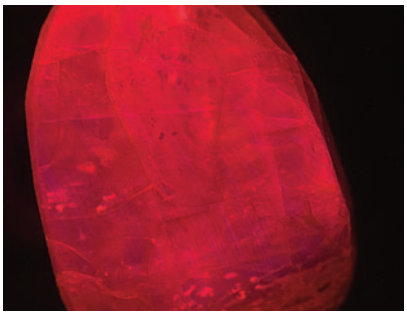

Figure 25. Curved growth striations were observed in the stone using the DiamondView, conclusively proving the synthetic origin of this ruby.

PHOTO CREDITS
Christopher Vendrell—1, 3, 4; Kyaw Soe Moe—4; Michaela Hariňová—5 (left); Nathan Renfro—5 (right), 6, 10, 18; Troy Ardon—8; Robert Weldon—9; Johnny Leung—11, 12 (bottom right); Tony Leung—11; Billie Law—12, 13, 14; Shunsuke Nagai—15; Makoto Miura—16; Diego Sanchez—17, 23, 24; Sood Oil (Judy) Chia—21; Joyce Wing Yan Ho—22 (left); Emiko Yazawa—22 (right); Forozan Zandi—25

The Dr. Edward J. Gübelin Most Valuable Article AWARD

First Place

A Quantitative Description of the Causes of Color in Corundum

Spring 2020

Emily V. Dubinsky, Jennifer Stone-Sundberg, and John L. Emmett


Emily V. Dubinsky


Jennifer Stone-Sundberg


John L. Emmett

Emily V. Dubinsky is a gemologist and jewelry designer based in San Francisco and New York City. She runs Emily Emmett Inc., a custom jewelry design firm named in honor of her longtime research collaborator and mentor Dr. John Emmett. She and her coauthors are currently working on various research projects studying causes of color in corundum in more detail. **Jennifer Stone-Sundberg** received a PhD in inorganic chemistry from Oregon State University. Dr. Stone-Sundberg has worked in the synthetic oxide crystal growth industry for 20 years, specializing in growing and characterizing materials such as sapphire, spinel, and garnet. She is a technical advisor for GIA and a technical editor for *Gems & Gemology*. **John L. Emmett** received his PhD in physics from Stanford University. For the majority of his career he was an associate director of the Lawrence Livermore Laboratory, responsible for all laser research and development. He is currently a technical consultant to GIA.

Second Place

History of the Chivor Emerald Mine, Part I (1880–1925): From Rediscovery to Early Production

Spring 2020

Karl Schmetzer, Gérard Martayan, and Jose Guillermo Ortiz


Karl Schmetzer


Gérard Martayan


Jose Guillermo Ortiz

Karl Schmetzer is a scientist living near Munich. He holds a PhD in mineralogy and crystallography from the University of Heidelberg. His principal areas of interest and research include: characterization of natural and synthetic gem materials and their properties, description of new gemstones and/or new gem localities, investigation of causes of color and color changes, detection of treatments, historical sources and history of gem deposits, and historical background of significant jewelry pieces. **Gérard Martayan** is an independent researcher with a focus on historical emerald mines. He obtained a master's degree in geophysics from the Institut de Physique du Globe engineering school in Strasbourg, France. **Jose Guillermo Ortiz** is president of the Colombian Emerald Co. He holds a master's degree in mechanical engineering from the National University of Colombia.

Third Place

Naturally Colored Yellow and Orange Gem Diamonds: The Nitrogen Factor

Summer 2020

Christopher M. Breeding, Sally Eaton-Magaña, and James E. Shigley


Christopher M. Breeding


Sally Eaton-Magaña


James E. Shigley

Christopher M. Breeding is a senior manager of analytics at GIA in Carlsbad, where he investigates origin of color in diamond and other gems. Dr. Breeding, who is a co-editor of *G&G*'s Gem News International section, holds a PhD in geology from Yale University. **Sally Eaton-Magaña** is a senior manager of diamond identification at GIA in Carlsbad, where she investigates the physics of natural, treated, and laboratory-grown diamonds. Dr. Eaton-Magaña received her PhD in chemical engineering from Case Western Reserve University in Cleveland, Ohio. **James E. Shigley** is distinguished research fellow at GIA in Carlsbad. He is the author of numerous articles on diamonds and colored gemstones. Dr. Shigley holds a PhD from Stanford University.

Many thanks to the members of G&G's Editorial Review Board for voting this year.

Thin-Film Fluid Inclusions in Aquamarine

The author recently examined a faceted aquamarine from Brazil that showed two-phase (liquid and gas) thin-film inclusions of different sizes and shapes. When observed using oblique fiber-optic illumination, the inclusions revealed a kaleidoscopic play of interference colors). The most diagnostic beryl inclusions, yet barely noticeable in brightfield illumination are ultra-thin-film fluid inclusions. The planar surface of these inclusions is oriented parallel to the basal pinacoid of their host (E.J. Gübelin and J.I. Koivula, *Photoatlas of Inclusions in Gemstones*, Volume 2, Opinio Publishers, Basel, Switzerland, 2005, pp. 312–314). The presence of the bright iridescent thin-film fluid inclusions resembles colorful rainbow sprinkles.

Muzdareefah Thudsanapbunya
Bangkok

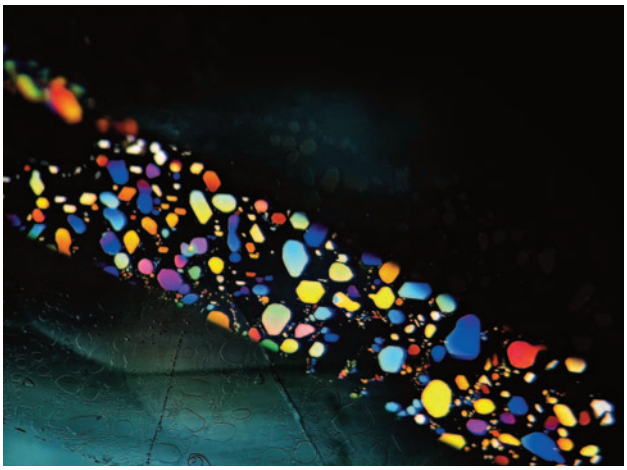

Figure 1. Thin-film fluid inclusions oriented perpendicular to the c-axis of this aquamarine display interference colors when viewed using oblique fiber-optic illumination. Photomicrograph by Muzdareefah Thudsanapbunya; field of view 2.79 mm.

Chromite in Emerald

The beryl species is known for its different colored varieties, such as pink morganite and blue aquamarine, which are directly influenced by the chemical composition of the stone. The emerald variety is colored green by the trace elements chromium and/or vanadium. Beryl, a beryllium aluminum cyclosilicate, has a crystal structure that readily integrates foreign elements. When an elevated amount of chromium is present in the growth environment, a beryl crystal has a chance of becoming an emerald. One inclusion that has been well documented in emeralds is the mineral chromite, an iron chromium oxide. Specifically, this mineral is a source of chromium for some Brazilian emeralds.

The author recently examined a matching jewelry set consisting of a bracelet and ring that were decorated with emeralds from Brazil. Each stone exhibited a unique concentration of color when viewed through diffused lighting. Compared to the angular or linear color zoning generally seen in emeralds, each of these stones displayed an irregular, circular green zone with strong graining. The color zoning correlated with crystallites of chromite (figure 2). During the emerald's crystallization, chromite from the growth environment was incorporated into the stone as an inclusion. A chemical alteration along the interface of the chromite and the beryl occurred due to the presence of chromium from the crystallites. The altered chemistry of the beryl led to the green bodycolor adjacent to the

About the banner: A blue color filter using transmitted light provides high contrast to the golden yellow rutile needles in this rock crystal quartz. Photomicrograph by Nathan Renfro; field of view 7.61 mm.

Gems & Gemology, Vol. 57, No. 1, pp. 64–69.

© 2021 Gemological Institute of America

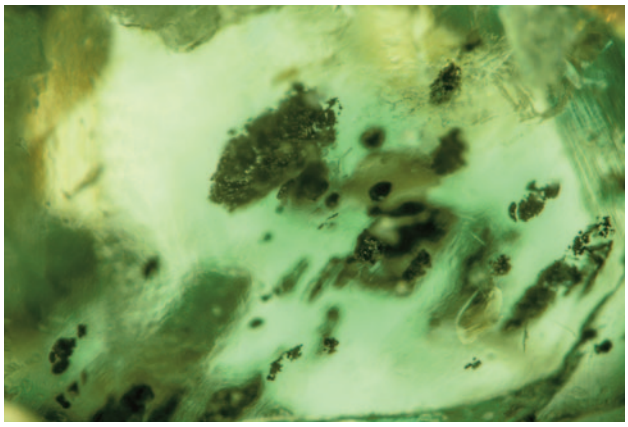

Figure 2. A Brazilian emerald with green color zoning and strong graining surrounding clusters of chromite. Photomicrograph by Nicole Ahline; field of view 1.58 mm.

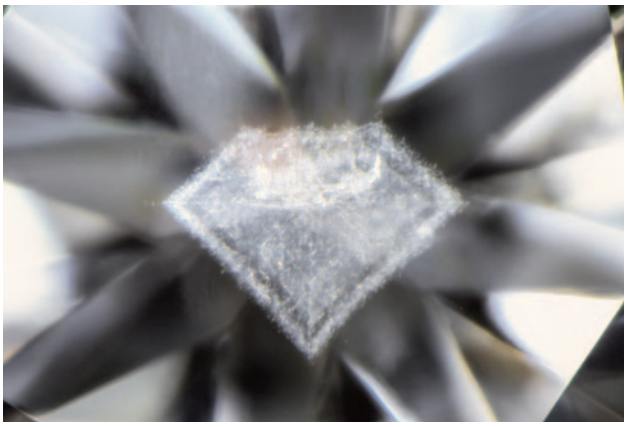

Figure 3. This 0.53 ct round brilliant diamond contained a unique cloud that resembled the profile view of a diamond. Photomicrograph by Nathan Renfro; field of view 2.60 mm.

chromite crystals. The strong graining is the result of the difference in refractive index in the green-colored area from the elevated chromium in contrast to the host beryl.

While chromite is regularly seen in emeralds from Brazil, it is not common to see such a strong correlation of color with the mineral inclusion.

Nicole Ahline
GIA, Carlsbad

Diamond-Shaped Cloud in Diamond

Diamonds can show some interesting surprises when examined by microscopy. Recently, the authors examined a D-color, 0.53 ct round brilliant diamond with an intriguing cloud inclusion that bore a remarkable resemblance to the profile view of a faceted round brilliant (figure 3). Due to the prominent diamond-shaped cloud under the table, the clarity grade of the stone was SI_2 (figure 4).

Photomicrography was used to chronicle the depth of the cloud, which indicated that it was three-dimensional and part of its center reached the diamond's surface. When focusing through the inclusion beginning at the surface of the table facet, the cloud spanned ~320 microns of focal distance. This is not the first instance of a faceted diamond showing a cloud inclusion with diamond-related geometry. Gemologists have shown other natural diamonds with clouds resembling diamond octahedra (Winter 2015 Lab Notes, pp. 428–429; Renfro et al., Winter 2018 *G&G*, pp. 428–429). However, this is the first cloud with such a shape the authors have encountered.

The infrared absorption spectra showed a type Ia diamond with saturated concentrations of nitrogen. Photoluminescence maps were collected with 532 nm and 455 nm excitation. A false-color map corresponding with the normalized intensity of a peak at 700 nm (figure 5A) was detected almost solely within the cloud. This peak at 700 nm has been ascribed to nickel and can be seen in hydrogen-rich diamonds, particularly within hydrogen-rich clouds (e.g., Fall 2020 Lab Notes, pp. 416–419).

In the 455 nm PL map, we detected the H3 center at 503.2 nm (figure 5B), which is identified as an A-aggregate decorated with a vacancy. The especially dense area along the "girdle" showed a distinct chemistry as that portion of the cloud had an elevated 700 nm peak intensity (figure 5A) and an elevated H3 concentration (figure 5B). Figure 5C shows the intensity of the diamond Raman peak. The Raman signal detected within the cloud shows decreased intensity; additionally, the diamond outline in this map corresponds well with the image in figure 3 (as the presence

Figure 4. The D-color, 0.53 ct round brilliant diamond has SI_2 clarity due to a distinctive cloud inclusion under the table facet. Photo by Marco Martinez.

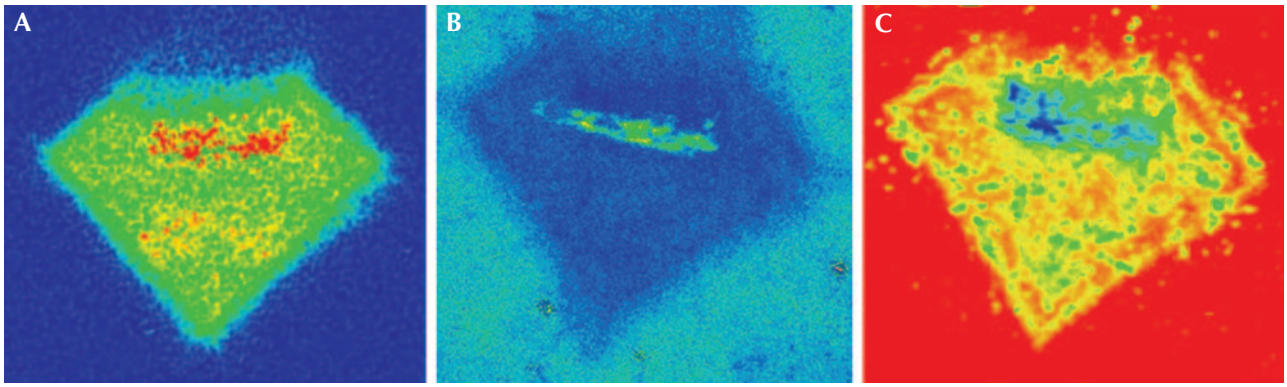

Figure 5. Photoluminescence maps were compiled from thousands of spectra (each pixel is 10 microns in size). A: Intensity of a peak centered at 700 nm (associated with nickel and often seen in hydrogen clouds). This peak intensity is normalized by ratioing to the diamond Raman peak. B: Intensity of the normalized H3 center at 503.2 nm; much of the cloud has a lower intensity than the surrounding diamond, but a portion of the "girdle" section of the cloud shows a higher H3 intensity. C: The map of the diamond Raman intensity corresponds well with the visual image, including the cloud resembling a diamond outline seen in figure 3.

of the cloud reduces the Raman signal reaching the detector). Prior research has shown that oftentimes such clouds form preferentially within the {100} growth sectors (W. Wang and W. Mayerson, "Symmetrical clouds in diamond – the hydrogen connection," *Journal of Gemmology*, Vol. 28, No. 3, 2002, pp. 143–152).

While this diamond-shaped cloud formation may cause some concern over the natural origin of such an inclusion (see an example of a 3D subsurface laser engraving in quartz in Fall 2020 Micro-World, pp. 427–430), the cloud in this diamond appeared to be completely natural when examined in the microscope. Generally, the absence of inclusions or clarity characteristics increases the beauty and value of a diamond, but not always. In this diamond, the cloud's presence adds beauty, value, and distinction. Thanks to an observant and skillful polisher, we get to see another "brilliant" example of an intriguing cloud inclusion in diamond.

Sally Eaton-Magaña and Nathan Renfro
GIA, Carlsbad

Alpesh Vavadiya
GIA, Mumbai

Expanded Diamond Surface Due to Radiation Staining

The author examined a 0.56 ct Fancy grayish bluish green diamond with prominent green radiation stains. Studies have shown that radiation can cause staining that expands

Figure 6. Dark green radiation stains on a natural diamond surface. This is a partially faceted diamond with some of its natural surface bounded by laser markings, seen as dark lines in the image. Photomicrograph by Nathan Renfro; field of view 2.24 mm.

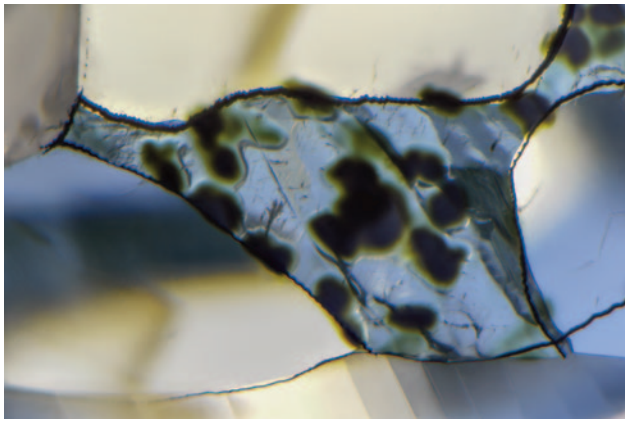

Figure 7. The radiation stains on a natural surface in reflected light, which highlights the smooth texture of the stained and expanded areas. Photomicrograph by Nathan Renfro; field of view 2.24 mm.

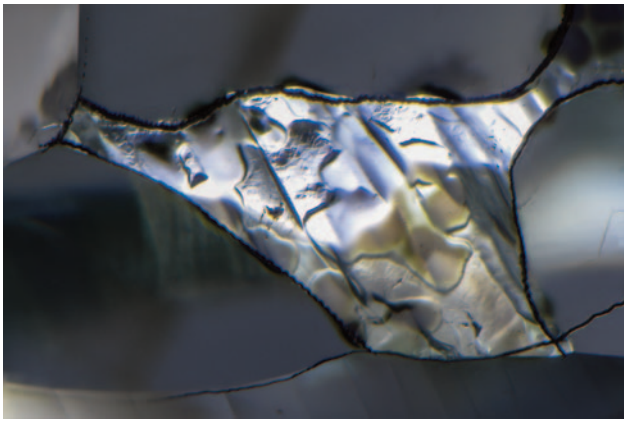

the surface of a diamond (L. Nasdala et al., "Radio-colouration of diamond: A spectroscopic study," *Contributions to Mineralogy and Petrology*, Vol. 165, 2013, pp. 843–861; S.C. Eaton-Magaña and K.S. Moe, "Temperature effects on radiation stains in natural diamonds," *Diamond and Related Materials*, Vol. 64, 2016, pp. 130–142). This can create a noticeable bump that is visible in the microscope. The effect in this diamond is so pronounced that the radiation stains appear encased in a protective plastic bubble. This expansion effect is believed to be caused by the radiation damage creating an expansion in the diamond lattice (Nasdala et al., 2013).

When viewed with transmitted light (figure 6), the raised lattice can be seen extending beyond the dimensions of the stain itself. The green-colored stains are very dark. Using reflected light (figure 7), the difference between surface textures is apparent. The surface that has been damaged and expanded by the radiation staining has a much smoother texture than the unaltered diamond surface. It is unknown why this diamond lattice was so distorted compared to typical radiation stains; they showed no unusual spectroscopic features that might provide a clue as to their formation.

Troy Ardon
GIA, Carlsbad

Unusual Fibrous Inclusions in Blue Opal

The authors recently encountered an opal with a grayish blue bodycolor and weak play-of-color. The gem also contained some interesting fibrous inclusions (figure 8). The inclusions were generally scattered throughout a planar zone as curled bundles of chatoyant fibers. This type of opal appeared to be naturally colored and consistent in appearance and physical properties with opal from Sinaloa, Mexico (Fall 2011 Gem News International, p. 243). Raman analysis was unable to identify the inclusions, but a strong cristobalite signal was measured in areas with the fibers and without them, suggesting a volcanic origin (E. Fritsch et al., "Green-luminescing hyalite opal from Zacatecas, Mexico," *Journal of Gemmology*, Vol. 34, No. 6, 2015, pp. 490–508). While the exact nature of these inclusions remains a mystery, this is the first time the authors have encountered this type of unusual coiled fibrous inclusion in blue opal.

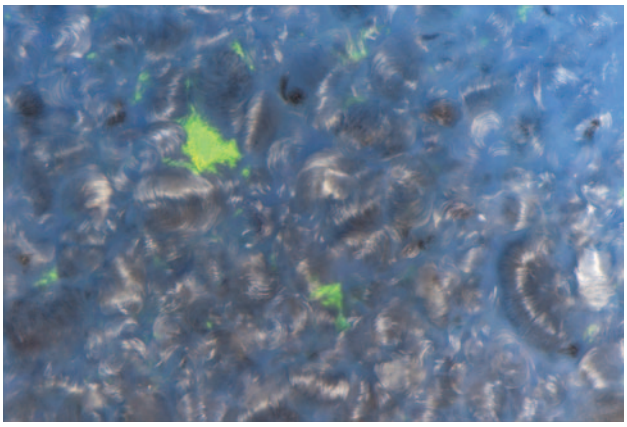

Figure 8. These unusual clusters of curled fibers were seen in a blue opal. Photomicrograph by Nathan Renfro; field of view 3.58 mm.

Nathan Renfro and Nicole Ahline
GIA, Carlsbad

Opal with Fluid Inclusion and Mobile Bubble

A Mexican opal was recently examined at the GIA laboratory in Carlsbad. The inclusion shows a euhedral void with a mobile gas bubble (figure 9). The void mimics the shape of a barite crystal that might have once been present in the opal. The barite crystal was likely dissolved during a dissolution phase during the growth of the opal, leaving behind only a fluid-filled void. Toward the end of the opal's

Figure 9. A Mexican opal containing a mobile gas bubble in the lower edge of the void (left). Tilting the stone causes the bubble to change position within the cavity (right). Photomicrographs by Jessa Rizzo; field of view 3.57 mm.

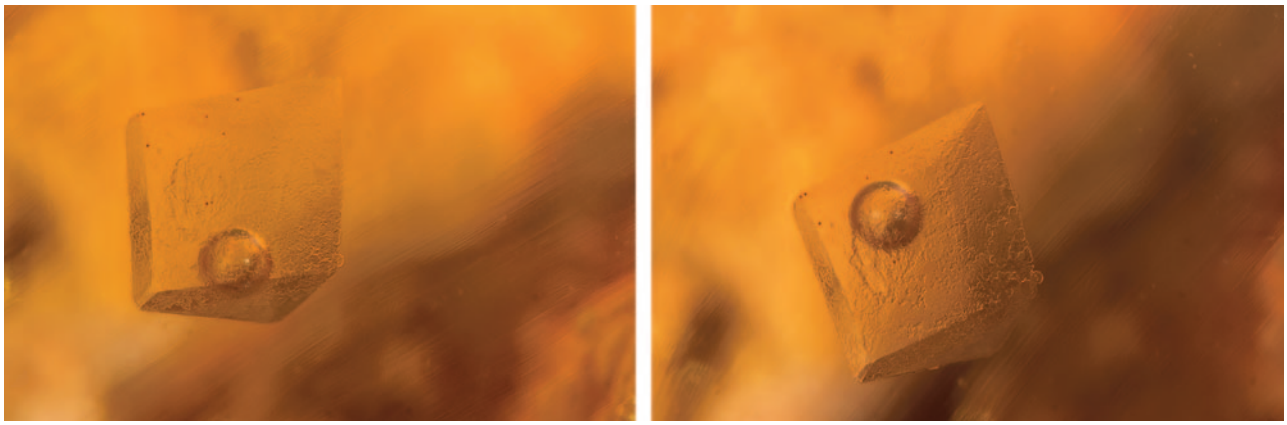

Figure 10. Large iridescent healed fissures in an oval mixed-cut sapphire. Photo by Shunsuke Nagai; field of view 12.20 mm.

formation, the temperature decreased, causing the trapped fluid to separate into liquid and gas phases. Because of the small size of the bubble relative to the void, rocking and tilting causes it to move about. Fluid inclusions in opal are generally quite rare, and one with a mobile bubble is exceptional.

Jessa Rizzo
GIA, Carlsbad

Remarkably Large Iridescent Healed Fissures Resembling Play-of-Color in Sapphire

An interesting iridescent pattern was recently observed in a blue sapphire. Gemological properties and inclusions indicated a natural sapphire, and the UV-Vis-NIR spectrum suggested basalt-related origin (e.g., A.A. Levinson and F.A. Cook, "Gem corundum in alkali basalt: Origin and occurrence," Winter 1994 *G&G*, pp. 253–262). The characteristic inclusions of blue color concentrations surrounding exsolution particles of rutile and numerous partially dissolved needles provide evidence of heat treatment (J.I. Koivula, "Internal diffusion," *Journal of Gemmology*, Vol. 20, No. 7/8, 1987, pp. 474–477).

Notably, this sapphire included unique large partially healed fissures showing attractive iridescence (figure 10). Similar iridescent healed fissures in sapphires and rubies from basaltic deposits have been previously documented (e.g., E.J. Gübelin and J.I. Koivula, *Photoatlas of Inclusions in Gemstones*, Vol. 3, Opinio Verlag, Basel, Switzerland, 2008, pp. 110 and 216–220); however, the healed fissures in this sapphire were remarkably large and visible to the unaided eye (figure 10). The fissures nearly parallel to the table facet showed variously colored iridescence with dendritic patterns (figure 11). Trapped air in a cemented plane of a doublet can also show such patterns (see Spring 2019 Lab Notes, p. 92), but this stone has no assembly feature. These attractive iridescent colors, resembling the "play-of-color" of precious opal, result from thin-film interference. This is a unique visual effect created by internal features in heat-treated corundum.

Makoto Miura and Yusuke Katsurada
GIA, Tokyo

Quarterly Crystal: Topaz with Phlogopite

This issue's quarterly crystal is a gem-quality very light pinkish brown topaz (figure 12) from the Dusso mine in Pakistan. The transparent singly terminated topaz crystal measures 30.52 × 29.84 × 27.89 mm and weighs 216.56 ct. It hosts a prominent 6 mm long dark brownish orange

Figure 11. Iridescent dendritic healed fissures in sapphire. Photomicrographs by Makoto Miura; field of view 2.10 mm (left) and 1.30 mm (right).

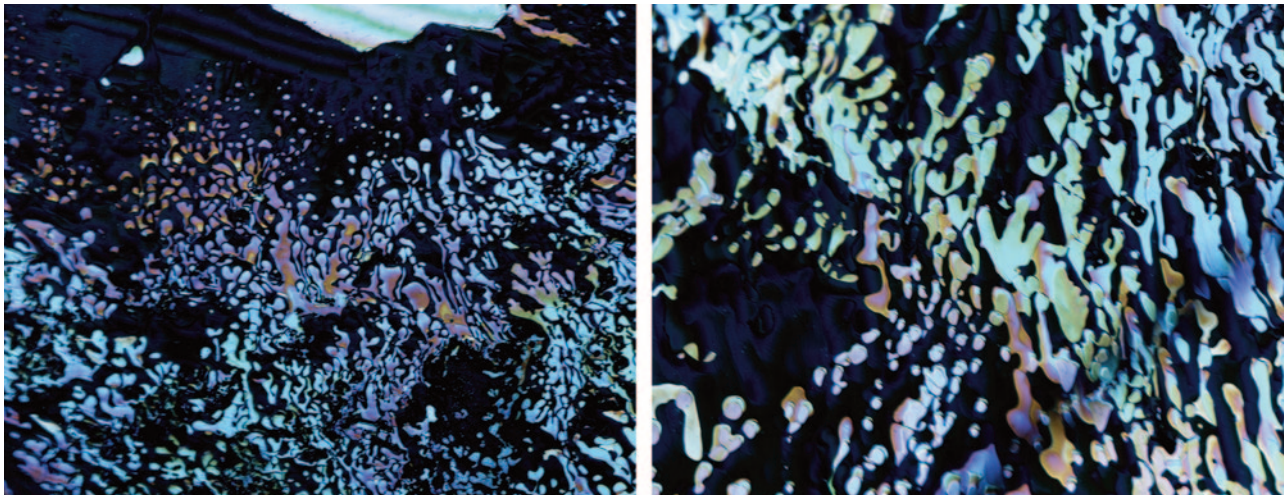

Figure 12. This 216.56 ct topaz crystal is from Dusso, Pakistan. Photo by Diego Sanchez.

phlogopite mica booklet that shows strong brownish orange and yellow dichroism as well as lamellar cleavage planes (figure 13). A tiny cluster of dark brownish red manganotantalite and colorless albite inclusions are also present. Small near-colorless and transparent mica and feldspar inclusions are randomly scattered throughout the crystal. This suite of inclusions strongly suggests that a complex granitic pegmatite was the parent rock type of this topaz.

John I. Koivula
GIA, Carlsbad

Figure 13. This prominent 6 mm crystal of phlogopite mica is hosted by the Pakistani topaz. Photomicrograph by Nathan Renfro; field of view 9.09 mm.

Gem News International

Contributing Editors
Emmanuel Fritsch, *University of Nantes, CNRS, Team 6502, Institut des Matériaux Jean Rouxel (IMN), Nantes, France* (fritsch@cnrs-imn.fr)
Gagan Choudhary, *Gem Testing Laboratory, Jaipur, India* (gagan@gjepcindia.com)
Christopher M. Breeding, *GIA, Carlsbad* (christopher.breeding@gia.edu)

VIRTUAL REPORT ON THE INDUSTRY IN 2021

As the major Tucson gem and mineral shows were all canceled in 2021 due to the pandemic, we decided to use our annual Tucson report space a bit differently this year. We wanted to capture how some of the vendors we normally visit have been weathering the situation and their thoughts about the impact on the trade along the entire supply chain. We wanted to find out how the pandemic has shaped their businesses over the past year and if they foresee permanent changes to the way business will be conducted in the future.

From our understanding going into these interviews, fine jewelry has actually been doing quite well during this time, as consumers who would normally spend money on travel have opted to spend those discretionary funds on luxury items, including jewelry. With the initial onset of the pandemic creating a full disruption to in-person sales, retail jewelry was hit hard in the spring. By summertime, however, sales had increased for many compared to the same period in 2019. This trend reemerged during the end-of-the-year holiday season. As discretionary travel is a strong competitor to fine jewelry, having people stuck at home benefited retail jewelry sales. Online jewelry sales appear to have benefited the most, increasing by about 50% over pre-pandemic times. To what extent these patterns will hold is uncertain. Another trend was the popularity of "Zoom-worthy" jewelry such as earrings and necklaces as online interactions with colleagues, friends, and family increased. To read more about some of the pandemic-related retail jewelry trends, see Victoria Gomelsky, "Even in a pandemic, fine jewelry is selling," *New York Times*, December 3, 2020, https://www.nytimes.com/2020/12/03/fashion/jewelry-rising-sales-pandemic-.html.

Starting at the mines, activity was clearly affected by work stoppages and the inability of foreign buyers and traders to travel internationally. These situations were highly dependent on local restrictions, which were often different in neighboring countries. In East Africa and Asia, many mines temporarily stopped production to comply with regulations to avoid gatherings of people, while others produced plenty of material but initially had no foreign buyers to sell it to. Much rough trading went online, allowing the continued flow of some materials between miners and buyers with established relationships. This online presence also brought forth completely new relationships for miners and local traders who started dealing directly with downstream buyers, such as cutters and jewelers, who normally would have made purchases through other channels.

In many instances, cutting and jewelry manufacturing workshops were significantly impacted by the pandemic on three fronts: the disruption in the supply of new raw materials, the inability to work together in factories in light of social distancing policies, and (in some cases) difficulty in shipping goods across borders. However, some rough dealers and jewelers have been opening the vaults to work with gems saved for a rainy day such as this.

Gem markets have been significantly impacted, as here too social distancing policies and travel restrictions greatly

Editors' note: Interested contributors should send information and illustrations to Stuart Overlin at soverlin@gia.edu or GIA, The Robert Mouawad Campus, 5345 Armada Drive, Carlsbad, CA 92008.

Gems & Gemology, Vol. 57, No. 1, pp. 70–100.

© 2021 Gemological Institute of America

Figure 1. Snapshots of an industry dealing with a global pandemic. A starkly quiet Jewelry Trade Center in Bangkok (top row) and Chan Gems Building in Chanthaburi (middle right); temperature screening outside a Pranda facility on the outskirts of Bangkok (bottom left); and two glimpses of activity at the Hainan Expo in China. Photos by Jinting Yu, Shen Chen, and Sunny Jiang.


ITC
FASHION OUTLET
GEMSTONE JEWELRY
JEWELRY TRADE CENTER / BANGKOK FASHION OUTLET


ITC 4TH FLOOR
NOW OPEN!!


LOVEONLY

Figure 2. Local business owner Jianying Ma in China's Hebei Province is shown livestreaming to connect with clients while stores were shut down. Courtesy of Han Dan Zhao Du Gold and Jewelry Co. Ltd.

reduced or eliminated the ability to gather and kept the international buyers who supply the cash necessary to keep trade moving away from these sites. Similarly, virtually all of the major trade shows globally were forced to cancel for the same reasons. Political unrest has also been impacting the movement of goods across borders, something we heard from several sources.

Stone dealers and jewelers in general reported a challenging time last spring, but reasonable to good sales from summer 2020 on. Many of them had to adapt to virtual interactions with suppliers and clients, some for the first time. However, several had already started building online presences, which were put to the test and rapidly expanded to accommodate this unusual year. Communication through WhatsApp and Zoom proved essential for many in continuing business both upstream and downstream. Vendors reported using social media such as Facebook and Instagram to keep clients updated on their activities. Even though it was clear that these vendors look forward to the return to big trade shows, they believe that the way business is conducted along the supply chain has likely been changed in some permanent ways by the recent forced reliance on doing business virtually.

We hope you enjoy our report showing the mixture of positive and negative trends over this unprecedented past year. We look forward to seeing everyone in person in Tucson next year. The 2022 Tucson shows will also bring us the opportunity to visit the Alfie Norville Gem and Mineral Museum, scheduled to reopen in 2021, and its Somewhere in the Rainbow collection. These are also featured in our report.

Jennifer Stone-Sundberg, Tao Hsu, Wim Vertriest, Aaron Palke, and Robert Weldon

The Chinese gem and jewelry industry reacts to COVID-19. When COVID-19 struck at the end of January 2020, the Chinese jewelry industry was caught off guard. The whole country was locked down—travel halted and businesses closed.

As the country gradually reopened at the end of March 2020, business remained very slow. But China has one of the most advanced digital ecosystems in the world. Mobile technology leapfrogged laptops and credit cards, while cheap, reliable, and efficient delivery companies made it easier for consumers to spend. Local businesses turned to the internet to reach old and new clients during the pandemic (figure 2). With fewer clients visiting stores, sales often started by livestreaming products, followed by sending photos and videos through WeChat, and then utilizing WeChat Pay or Alipay to complete the transaction. Chinese digital infrastructure made a big difference in helping the jewelry business bounce back so quickly.

Figure 3. To maintain social distance, Van Cleef & Arpels limited the number of clients in stores. Here, clients wait outside the store in the Shanghai IFC Mall. Photo by Chen Shen.

During these difficult times, relationships with suppliers and clients are the key to keeping business moving. Trust built over years is extremely important when buying or selling valuable gemstones and jewelry online without actually seeing the items in person. Major jewelry chain stores, which rely more on foot traffic, experienced a dramatic double-digit decline in business in the first half of 2020, while small jewelry stores that rely more on personal contact and relationships felt little to no impact.

Due to travel restrictions, we did see certain product shortages on the market, as it was initially difficult for some goods to enter China. Some Chinese dealers took a risk and broke quarantine to visit Sri Lanka or India to source products. On the other hand, some international businesses even came to China for products and services when jewelry and diamond cutting factories closed in the U.S. and India.

In general, jewelry sales had negative growth for the first half of the year. Sales started to pick up in July. Sales from October, November, and December were up 16.70%, 24.80%, and 11.60%, respectively, compared to the same months in 2019.

International jewelry brands such as Cartier, Tiffany, and Van Cleef & Arpels (figure 3) did exceptionally well in 2020 since Chinese consumers could not travel for overseas shopping trips. With social distancing and a mandatory mask policy in stores, these luxury brands saw an immediate business jump in China by April 2020. Plaza 66 Shanghai, owned by Hang Lung Properties, is the country's top luxury shopping mall. Its reported retail sales were up 60% in a year with COVID-19, demonstrating an amazing year for luxury brands in China.

Chen Shen
Gembridge, Shanghai
International Colored Gemstone Association

Constantin Wild (Constantin Wild GmbH & Co. KG). Constantin Wild and his team started 2020 with a strong Tucson show and orders to fulfill from 2019. Upon returning to Germany, the severity of the COVID situation became apparent, and on March 14 they were forced to temporarily shut down the business. Mr. Wild was fortunate to keep his staff, though they did have to cut back work initially to only one day a week. Since August, they have been able to work at 80% of full-time. The second half of 2020 saw business levels basically return to normal, and overall the year was pretty good. Tucson was the company's only trade show in 2020, and they do not expect to attend any shows in 2021. The biggest disadvantage of not going to trade shows has been missing out on new opportunities.

To keep in touch with clients and partners, Zoom and WhatsApp became essential for video calls. Mr. Wild has also been inviting clients to their facility in Idar-Oberstein for relaxed face-to-face visits. The business has been sharpening its brand image and plans to relaunch its website and blog as well as provide regular Facebook and Instagram feeds.

Figure 4. A lively 24.07 ct yellowish green cushion-cut tourmaline from new fields in the Democratic Republic of the Congo. Photo © Constantin Wild.

Without being able to travel, the team has taken the time to sort and recut stock in their inventory. They have also been cutting rough from their vaults, as the new rough supply has been restricted during the pandemic.

When asked about pandemic sales, Mr. Wild noted that gemstones suitable for high jewelry have been in demand, in addition to a new trend for high-value gems as standalone pieces. During the past year, sales have been particularly good for Paraíba tourmaline, green tourmaline (figure 4), aquamarine, and Imperial topaz (figure 5). Mr. Wild also noticed strong demand for gray spinel, whether atonal or modified by blue or purple. He has done well selling color suites of stones, such as his "Rhapsody in Blue," which features a diverse array of blues provided by tanzan-

Figure 5. This 4.06 ct red pear-shaped Imperial topaz is from Ouro Preto, Brazil. Photo © Constantin Wild.

Figure 6. The "Rhapsody in Blue" suite (145.2 carats total) is composed of 17 gems: nine greenish blue cushion-cut aquamarines from Brazil, four oval-cut tanzanites, and four intense blue oval-cut Mozambique aquamarines. Photo © Constantin Wild.

ite and both greenish blue and intense blue aquamarine from Brazil and Mozambique (figure 6).

During this time, Mr. Wild has been able to work on a book commemorating the firm's 175th anniversary next year. Titled *Gems, Colours, and Wild Stories… 175 Years of Constantin Wild*, the book will explore the history of the company and provide many entertaining stories and high-quality images to capture the unique emotions associated with colored gems.

Mr. Wild looks forward to returning to Tucson in 2022 and predicts that demand will focus on vibrant colors to celebrate the end of the pandemic.

Jennifer Stone-Sundberg
GIA, Carlsbad

Dudley Blauwet (Dudley Blauwet Gems). In February, colored stone dealer Dudley Blauwet attended the only 2021 Tucson "show," held at Mineral City and the adjoining Sun Gems building. The Mineral City hub consists of several steel unit buildings that are classified as permanent business storefronts and therefore were not subject to the same COVID-19 requirements as events. In the 18 days Mr. Blauwet was there, he estimated that fewer than 500 people attended, including those associated with the 20–25 vendors. Beyond these vendors, another 6–10 gem- and mineral-related businesses that own warehouses in Tucson were open. Mr. Blauwet and one other vendor were the only ones carrying cut gems, while everyone else was offering minerals exclusively. A lack of fossils and meteorites was noticed.

Since summer, business has been fine for Dudley Blauwet Gems, as many of his online customers have been doing well and are looking to fill specific orders or rebuild stock. Using WhatsApp, he has been able to continue communicating with and purchasing material from suppliers such as a Sri Lankan family the business has worked with for nearly 40 years. This has included viewing sapphires from photos or videos almost daily. He has also been working with Russian contacts to purchase unoiled emeralds (figure 7), alexandrite, phenakite, and some demantoid. A source in Southeast Asia has also been supplying gray spinel.

Figure 7. Unoiled Russian emeralds (a 1.29 ct emerald cut and a 1.14 ct pear shape) from Malyshevo, Ural Mountains, with intense bluish green color reminiscent of Paraíba tourmaline. Photo by Aria Agarwal; courtesy of Dudley Blauwet Gems.

Sales have been predominantly natural sapphire, unoiled emerald, gray spinel, and Vietnamese cobalt spinel. He noted that other stones such as aquamarine, green beryl, and morganite have been popular. The persistent demand for sapphire has been dominated by requests for teal, green to icy green, peach to apricot, "padparadscha," periwinkle, purple-blue, and light to icy pink sapphire, as well as for traditional blue colors. Recently, he has received numerous calls for Mandarin garnet from Loliondo, Tanzania; heated blue zircon from Cambodia; and to a lesser extent Malaya garnet from Mahenge, Tanzania. Mr. Blauwet's business mainly offers untreated natural sapphire, but they have had steady demand for heated blue rounds and matched pairs.

With the 2021 Pantone colors of the year being "Ultimate Gray" and "Illuminating" (a medium gray and butter yellow, respectively), Mr. Blauwet has seen a bit more interest in yellow sapphire over last year and steady interest in gray spinel (figure 8). They have also developed a good market for unoiled Russian emerald, with some vendors regularly restocking.

Mr. Blauwet was able to provide some insight into the movement of material coming from mines around the world and the rough supply situation. With the political upheaval in Myanmar, Burmese gem production is expected to slow if not outright end for a while. Madagascar is opening up for travelers, but with a lack of express mail service, very little rough has left the island since last March. Some of the biggest gem mining operations in Sri Lanka are currently down. These combined supply slowdowns and stoppages have resulted in serious challenges—a very limited supply of rough worldwide and reduced movement of rough and gems to trading centers such as Bangkok or Hong Kong. As a result, the available supply of gems has been significantly dampened.

Mr. Blauwet mentioned that most of their trade shows for this year have been canceled, so they are handling increasingly larger orders and shipping 20 to 100 stones at a time to their manufacturing customers. Also, for the first time in Mr. Blauwet's life, he has started a website to sell gems wholesale. His business is struggling to supply enough rough to its cutting factories to keep all of the cutters busy. Occasionally, they have been able to buy small rough to cut precision diamond melee in calibrated sizes, still a very popular product.

Finally, Mr. Blauwet shared with us some blue spodumene he has been storing in the vault. For decades he has been buying Afghan spodumene crystals, which have a strong blue color on the c-axis and a green color on the a- and b-axes. To avoid any exposure to daylight, these stones were wrapped in paper at the mines in Afghanistan. He has kept them in closed boxes to sell to customers specifically wanting spodumenes that have not been exposed to UV. As a test, he exposed several of them to Colorado sunlight in June and was able to literally watch them change to a full purple color down the c-axis and a pink color down the a- and b-axes within 40 minutes. Mr. Blauwet currently has several clean faceted stones in sizes up to approximately 300 carats (figure 9). He has seen some dealers buy these crystals and take them to a show and watch in horror as they change over the course of three to five days from exposure to the various wavelengths of light present in the showroom—often the transition color before pink has

Figure 8. Yellow sapphire, gray spinel, and gray moonstone represent popular gems matching the 2021 Pantone colors of the year. Gray moonstone: 3.94 ct cabochon from India. Yellow sapphire: 2.39 ct oval from Dela, Sri Lanka, and 2.90 ct long cushion from Gilamale, Sri Lanka. Gray spinel: 0.93 ct cushion, 2.81 ct pear shape, and 1.16 ct round, all from Mogok, Myanmar. Photo by Aria Agarwal; courtesy of Dudley Blauwet Gems.

Figure 9. A 166.25 ct blue spodumene removed from storage. The stone is from Parun, a few kilometers from Paprok in Kamdesh District, Nuristan Province, Afghanistan. It was cut in Peshawar, Afghanistan, with the table perpendicular to the c-axis to achieve a blue color rather than green. Photo by Dudley Blauwet; courtesy of Dudley Blauwet Gems.

Figure 10. Popular sapphire colors, including bicolor stones from Montana. These heated stones from the Gem Mountain, Missouri River, and Dry Cottonwood Creek areas are 4.0 mm in diameter. Photo by Dillon Sprague; courtesy of Columbia Gem House.

strong unattractive gray tones. He reports that there are plenty of irradiated Afghan spodumenes on the market in Peshawar with a very strong emerald green color, including on the c-axis. The color is very unstable and with exposure to UV or daylight will change rather quickly, often turning an undesirable yellow-gray color. Mr. Blauwet described once making the mistake of buying a faceted example of these treated stones at a gem show in Peshawar from a dealer he did not know. When he unwrapped it years later, it had changed to an unattractive gray color with no exposure to UV or sunlight.

Jennifer Stone-Sundberg

Eric Braunwart (Columbia Gem House). Eric Braunwart, founder of this gemstone mining, cutting, and wholesale marketing company, reported that they have stayed busy during the pandemic after the initial shock to business with the hard shutdown last spring. Columbia Gem House had already started transitioning three years ago to doing more business electronically. When the pandemic hit, they were well positioned to experience a less dramatic shift in how they interact with clients than some more traditionally run gem dealers. Mr. Braunwart sees the pandemic as having universally pushed people involved in all stages of the gem trade to do more of their business online.

Overall, Mr. Braunwart is happy with the way business is going but thinks that much of what he is experiencing has more to do with the clientele he has attracted and his move toward a strong digital platform. Currently, his customer base is part of what he considers the "new industry," composed almost exclusively of women under 35 years old with independent stores, galleries, or studios. These buyers have grown up with smartphones and had already been doing business online but were pushed even further online with COVID-19. Columbia Gem House's fair trade and responsibly sourced position in the marketplace resonates with this "new industry," where these factors are an important part of the business models and branding and their clients' lifestyles. Additionally, these buyers tend to purchase more unusual items with respect to color, cut, shape, and presence of inclusions.

Mr. Braunwart noted that the biggest disruption to the supply chain with COVID-19 has been at the mines, where mining has slowed with less travel and demand—greatly restricting the supply to wholesalers. This has particularly been the case with small miners who have not had travelers coming out to purchase at the traditional venues. This has pushed some small miners to explore selling online to reach some of the market and realize some of the markup that traditional cutters and wholesalers see. Gem cutting has also slowed significantly, with less rough coming out of the mines and restricted flow of goods crossing borders, due both to the pandemic and political issues. On a very somber note, COVID-19 has personally hit many small businesses along the supply chain, with some longtime miners, cutters, and traders dying from the disease.

When asked what has been in high demand this past year, Mr. Braunwart stated that sapphire is still the king in terms of volume and dollars. A variety of North American stones are still doing well and sales continue to increase. The recent increase in the desire to buy American continues, and now these products are more recognized in the marketplace. Demand for teal and other nontraditional sapphire hues remains very strong (figure 10). About half of the customers pursuing these nontraditional colors popularized by the sapphire mines in Montana want American sapphire, but the other half are concerned only about obtaining the desired colors and are buying material coming from Africa and Asia.

A notable trend mentioned was the continued and increasing popularity of melee and smaller stones (baguettes, briolettes, trillions, kites, and hexagons; see figure 11). Both

Figure 11. A variety of popular small-stone shapes such as kites, hexagons, trillions, and briolettes. All are heated Missouri River sapphires. The kites are either 6.0 × 4.0 mm or 5.0 × 3.0 mm, the hexagons are 3.5 mm in diameter, the trillions are 4.0 mm wide, and the briolettes are 4.0 × 3.0 mm and side-drilled. Photo by Dillon Sprague; courtesy of Columbia Gem House.

saturated and pastel hues of these smaller stones are in strong demand (figure 12). They are being used not only as accent stones but also as the main stones in many jewelry pieces. This reflects a growing fashion direction where more affordable pieces can be made using both precious gemstones and precious metals. Mr. Braunwart mentioned a shortage in 1.0–1.3 mm melee, as this size is very difficult to cut and mines traditionally do not collect the small rough that would produce these sizes. This means that melee in these sizes are coming from larger rough and scraps.

Jennifer Stone-Sundberg

Gem Shopping Network: An online jewelry business during the pandemic. The COVID-19 pandemic has forced many sectors to adopt new work routines and move their commerce online. This is also true for the gem and jewelry industry. However, some businesses have been on-air and online for quite a long time. One of the veterans is the Gem Shopping Network (GSN), headquartered near Atlanta.

Since 1997, GSN has grown from a weekend show to a network that reaches over 60 million U.S. households. From television to the web and more recently the mobile app, the network can livestream its gem and jewelry shows through all available channels. At the beginning of the pandemic early in 2020, GSN immediately adopted proper social distancing and regulations to keep its employees safe, which allowed the crew to operate without a pause. Show hosts continued livestreaming from the studios, entertaining and educating their audience (figure 13).

Because GSN carries a vast array of goods—from mineral specimens, faceted gemstones, and finished jewelry all

Figure 12. Melee and small sizes of fire opal and neon green beryl. The fire opals are from Mexico and range from 0.10 to 0.20 ct. The neon green beryl material is from Nigeria—the rounds are 3.0 mm in diameter and the baguettes are 4.0 × 2.0 mm. Photo by Dillon Sprague; courtesy of Columbia Gem House.

Figure 13. GSN show host Marvin Pierschbacher presents finished jewelry. Live shows are entertaining and educational, and therefore very well accepted by the audience. Courtesy of GSN.

the way to collectibles and estate jewelry—supply has been a critical component since its earliest days (figure 14). While some in-person sourcing was prohibited by the situation, the supply side of the business was not negatively impacted overall. Some suppliers who would normally provide goods through outlets such as the cruise ship industry were able to transfer them to online jewelry traders such as GSN.

The majority of GSN's customers are women ages 50 to 65, a demographic that has been quite stable over the past two decades. This customer base proved advantageous when "staying at home" became the new normal as more time was available to watch the shows and purchase goods. Although international transportation was impacted by COVID-19, U.S. domestic shipping and delivery remained quite efficient. Steady supply, a stable customer base, and on-time delivery combined to make 2020 one of GSN's strongest years financially.

As both a seller and an educator, GSN has its own gemology content production team. The pandemic unexpectedly allowed more time for the team to produce content, which is shared over the multiple streaming channels. High-quality content is one of the key pillars for any online seller as it is the tool to attract and maintain customers. As the world gradually recovers from the pandemic, online jewelry trading is expected to see strong growth in the future.

Tao Hsu
GIA, Carlsbad

Jeff Hapeman (Earth's Treasury). How does one prepare for a global pandemic on a scale unlike anything seen in recent history? While it would have taken an extraordinary act of foresight to predict how significantly the world has changed since March 2020, one trend was set in motion several years ago. Increased online presence, especially with social media, proved enormously beneficial to many in the gem and jewelry industry. Jeff Hapeman of Earth's Treasury in Westtown, Pennsylvania, was at the forefront of this social media trend and shared his views on its impact on the trade since the pandemic and beyond. Mr. Hapeman got his start faceting gemstones (figure 15). However, he has grown his business over the last few years by hiring several designers and bench jewelers and

Figure 14. Finished jewelry featuring a broad range of colored gemstones, including some exotic varieties, is one pillar product carried by GSN. Courtesy of GSN.

Figure 15. A 2.04 ct blue brilliant-cut unheated Rock Creek sapphire. Photo by Jeff Hapeman.

Figure 16. A ring sourced, designed, and manufactured by Earth's Treasury displaying a 2.14 ct heated Rock Creek sapphire alongside melee-sized unheated sapphires from Rock Creek. Photo by Jeff Hapeman.

developing what he calls his "mine to finger" approach. By building close relationships with the people producing rough material at gem mines around the world and moving the jewelry-making process in-house, he is able to capture more of the value-added chain in getting rough stones to the end consumer (figure 16).

In March, when Pennsylvania went into strict lockdown, all employees of Earth's Treasury were sent home and asked to continue working on any projects they could. His bench jeweler sorted and graded melee stones, while his designer created new stock pieces. Fortunately, given Mr. Hapeman's heavy online involvement, Earth's Treasury was classified as an e-commerce retailer and allowed to open again after only about a month. Of course, there was an immediate plunge in sales in March and into April, but by May sales were picking up. In June, everything took off and business was much stronger than usual. This uptick in gem and jewelry sales is likely related to delayed purchases. As the uncertainty of the early days of the pandemic began to recede and the economy started coming out of the hard lockdown seen in much of the country, consumers had discretionary funds for jewelry purchases that would have ordinarily been set aside for travel or other luxuries. E-commerce jewelers did especially well last summer as the country slowly reopened with new safety restrictions that made in-person shopping at traditional brick-and-mortar shops more difficult.

Of course, this move to online jewelry sales did not happen in a vacuum. As social media continues to take an expanding role in our lives, modern consumers have become increasingly comfortable buying gemstones online at higher price points. Since the pandemic, Mr. Hapeman has noticed that customers are becoming more comfortable with the online purchasing process. Because Earth's Treasury offers free returns for gems and jewelry by FedEx or UPS, customers are willing to purchase and try something before settling on exactly what they want. In fact, he has stopped private showings at his offices for now and is moving more toward video consultations with potential clients.

The pandemic has dramatically affected not only the way we buy and sell gems but also the supply chains for the colored stone industry. While Mr. Hapeman deals a lot in domestically sourced Montana sapphire, it has become increasingly difficult to source gem rough internationally. In particular, rough exports from Africa have apparently dried up recently, given difficulties in exporting this material to locations such as Bangkok where it could be further distributed around the world. Some major gem cutting centers have also seen a decline in business as their international buyers can no longer visit. As a result, it has become much easier to purchase Sri Lankan stones for recutting. Interestingly, he has seen an enormous amount of tanzanite become available recently, which he speculates may be related to the material being rerouted from the badly stricken cruise industry.

The biggest potential impact of the COVID-19 pandemic on the industry concerns trade shows. While the rise of online sales had been felt by global gem and jewelry shows such as Tucson for several years, the ability of the industry to survive, and perhaps even thrive, for more than a year without a major gem show may cause many to question whether the events are crucial for their business. As we pull out of this pandemic world, it remains to be seen how major international gem shows will react and adapt.

Aaron Palke
GIA, Carlsbad

Josh Hyman (Philadelphia Jewelry Appraisers). Just over a block from Liberty Bell and Independence Hall, between 7th and 8th on Sansom Street, lies Philadelphia's bustling

Figure 17. A 19.56 ct boulder opal is surrounded by Montana sapphire and California spessartine garnet in this brooch commissioned by Josh Hyman. Photo by Laurie Seniuk.

Jewelers' Row. While other American jewelry districts like New York's Diamond District are more well-known, Philadelphia's Jewelers' Row carries the distinction of being the nation's oldest. It is home to many fourth- and fifth-generation jewelry families who took up business in converted row houses built in 1805. Those in need of valuation services can walk into the shop of Philadelphia Jewelry Appraisers and speak to Josh Hyman, the city's only full-time jewelry appraiser.

The Hyman family's jewelry tradition in Philadelphia began with his great grandfather Ruben Littman, a curb merchant who went door to door buying precious metals. Mr. Littman got to know the jewelers on Sansom Street, who purchased precious metals from him. Several generations later, Josh Hyman found himself working in his family's retail shop on Jewelers' Row. After pursuing his gemological education in Idar-Oberstein and then at GIA in Santa Monica, he worked in retail in Aruba before settling back in Philadelphia. There he found his niche as an appraiser serving the vibrant gem and jewelry industry on Jewelers' Row. One of the most rewarding aspects of his work as an appraiser is studying the gemstones submitted to him, which pushes him to tirelessly continue his gemological education. In fact, Mr. Hyman has become quite active in the gemological community online by creating the popular "Gemology Worldwide" Facebook page and podcast series. He admits to having a somewhat ulterior motive, as he wanted to create an educational forum to not only inform others but also advance his own gemological knowledge.

At the beginning of the pandemic in March of 2020, Philadelphia Jewelry Appraisers was shut down for three months. Despite the dismal outlook at the onset, as soon as he reopened in June, demand came back at full strength. While reduced foot traffic on Jewelers' Row may have led to fewer walk-ins, Mr. Hyman had already been driving demand for his services through heavy online advertising, especially Google Reviews. As an appraiser, Mr. Hyman has his finger on the pulse of the trade and offered some insights on the jewelry industry's response to the pandemic crisis. The few months after reopening were a huge boon for the jewelry industry globally as well as in Philadelphia. He attributes this, in part, to the fact that people largely stopped spending discretionary money on experiences such as travel and eating out. Consumers realized that purchasing and gifting gems and jewelry could also become an experience, so the discretionary spending typically allocated to travel was diverted to jewelry. Throughout the pandemic, Mr. Hyman has seen increasing demand for sapphires over rubies and emeralds. In particular, the demand for pastel and teal sapphires has grown, especially for sapphires from Montana (figure 17). Although sales slowed into September and through the end of the year, the outlook is positive. However, it remains to be seen how this might change as the world navigates its way to some form of normalcy and people resume traveling again.

According to Mr. Hyman, one of the main factors keeping the gem and jewelry industry strong, despite the cancellation of major gem shows, is the consumer's increasing confidence in buying online over the last few years. Rough and cut gems and jewelry that would have ordinarily changed hands in Tucson or Hong Kong made their way to the end consumer anyway by being sold online. The next few years will show us how the major gem shows like Tucson will adapt to this drive toward online sales.

Aaron Palke

Adapting to the changes with Paula Crevoshay. With the cancellation of the 2021 Tucson AGTA show, this author's annual meeting with jewelry designer Paula Crevoshay went virtual. The conversation started with her 2020 AGTA Spectrum Award–winning piece, followed by how her business adapted to the new norm under the circumstances brought by the pandemic.

Ms. Crevoshay's "Brown-Eyed Susan" won the Gem DIVA Award for classical wear (figure 18). This bespoke 18K yellow gold pendant features a 5.30 ct orange Montana sapphire from the Rock Creek deposit, operated by Potentate Mining. Although this stone is heated, the color saturation and size still make it a significant sapphire from this location, according to the mine owner. The center stone is

Figure 18. This award-winning pendant featuring a 5.30 ct heated orange sapphire from Montana depicts a blooming brown-eyed Susan. Wildflowers are one of Paula Crevoshay's favorite themes. Courtesy of Paula Crevoshay.

accented with yellow and orange sapphires (8.69 carats total) in addition to black and cognac diamonds (1.98 carats total).

While Ms. Crevoshay has always blended the nature of the stones with her art, she also tells stories through her jewelry creations. This piece is no exception. It continues the story from her first-ever flower themed piece, inspired by the bitterroot wildflower, which thrives on the hillsides of the Rock Creek sapphire mine. By early June, the slopes are covered by bitterroot and brown-eyed Susans. Upon seeing this orange sapphire, she immediately thought to place it at the center of a brown-eyed Susan pendant. Creating these beautiful floral jewelry pieces is never easy because of the time it takes to find so many stones in specific colors. This is also why she has never reproduced any of her jewelry, unless as a replacement for a lost piece.

As a business owner, Ms. Crevoshay also felt the impact of the pandemic. With careful planning and quick adaptation, she was able to keep her employees safe so that they could continue to work. In fact, 2020 was a good year financially for her company due to the relationships built with the stone supply chain over the past several decades and the customer base she has carefully maintained. To help manufacturers downstream survive, she also intentionally diverted her work to different jewelry-making studios, most of them located in Asia.

Being able to talk face-to-face with customers and provide fashion suggestions even beyond jewelry wear is an asset; connecting with them virtually during the pandemic is also critical. Ms. Crevoshay hosts regular online gatherings with her clients, which have been quite successful in keeping people in the loop. During the 2020 holiday season, she created a digital flipbook for customers to explore at their convenience (https://online.flipbuilder.com/dznx/qrub; see figure 19). Ms. Crevoshay advises that staying connected at all times and adapting to unexpected circumstances are key for both industry veterans and newcomers.

Tao Hsu

Prida Tiasuwan (Pranda Jewelry Group). Thailand enjoys a strong reputation for jewelry manufacturing, employing a highly skilled workforce in its many factories. Although it was the second nation with confirmed COVID-19 cases, Thailand remained relatively unaffected by the virus. The government quickly imposed strong measures such as remote work, curfews, and closure of places where people gather in great numbers. The action that arguably had the greatest impact was the closure of its international borders. The government tightly controlled travel to the country and enforced a strict 14-day quarantine for everyone who

Figure 19. Paula Crevoshay's digital flipbook for the 2020 holiday season featured more than 50 jewelry creations. Courtesy of Paula Crevoshay.

Figure 20. COVID-19 safety measures in place at this Pranda facility include a disinfection tunnel at the entrance. Photo courtesy of Pranda Jewelry Public Company Limited.

entered. Today, more people are allowed to enter, but the two-week quarantine is still mandatory.

The travel ban had a devastating impact on the region, which relies heavily on tourism and business travel, but it also left its mark on the local jewelry manufacturing scene. We spoke with Prida Tiasuwan, chairman of the Pranda Jewelry Group, about the situation in Thailand. He confirmed that the proactive measures taken by the government affected business in the first months of COVID, but this period did not last very long. By June 2020, business was returning, and a few months later demand was high, most likely because of the upcoming holiday season. This positive outlook continued with the arrival of vaccines in early 2021.

The Pranda facilities operated at reduced capacity during the Thai lockdown, which allowed the company to save costs due to reduced salaries for all staff and selected furloughs in April and May. Mr. Tiasuwan personally headed a task force consisting of department managers to ensure that all 2,200 staff remained safe and production could return to a normal pace as soon as possible.

By temporarily reducing capacity, they were able to improve working conditions for staff, including social distancing measures. Employees quickly adopted these new principles, and many of them were able to work from home. Since August 2020, the facilities have been back at full capacity with all required precautions, including a "Safe and Clean" campaign to remind everyone of the simple steps they can take to prevent the spread of the virus (figure 20).

Still, Pranda encountered issues with the supply of raw materials such as diamonds and certain colored stones. These are typically sourced or cut in countries such as India and China, where the impact on businesses was more severe during the first months of the pandemic. On the other end of the chain, physical retail was heavily impacted but was compensated by an increase in e-commerce.

The economic impact of the pandemic is also reflected in the demand for jewelry, according to Mr. Tiasuwan. The focus is on simple pieces in smaller sizes, with very few set stones or none at all. Customers have not been looking for fancy, colorful jewels during the pandemic, but Pranda expects this to change once the economic situation stabilizes.

Wim Vertriest
GIA, Bangkok

Rock Creek sapphire mining and marketing update. Sapphires were discovered in Montana on the West Fork of Rock Creek in 1892. The shiny pebbles were later identified as sapphire and featured at the Paris Exposition in 1900. Four deposits, one primary and three secondary, were discovered and developed across the western portion of the state. Among them, the secondary deposit at Rock Creek has always been the richest and the most productive. It is estimated that this deposit produced about 65.8 tons of rough sapphire until 2014, which is about 90% of the total sapphire production of all four deposits.

Since 2011, Potentate Mining has been gradually developing and expanding its sapphire mining concession in the Rock Creek area through a series of land purchases. With the latest deal done in 2020, the company now possesses more than 3,500 acres of private property over the sapphire-bearing land. Even with this large acreage, the mining operation works under a Small Miners Exclusion permit,

Figure 21. The newly equipped water clarifier at the West Fork property can nearly fully recycle the water used for mining. Courtesy of Potentate Mining.

which allows the miners to disturb no more than five acres of land at a time and requires them to rehabilitate the land right after mining is done.

In addition to the expansion, in 2019, the washing plant moved from Eureka Gulch to a new location at the West Fork property, where mining is done on the top of the hill (T. Hsu et al., "Big Sky Country sapphire: Visiting Montana's alluvial deposits," Summer 2017 *G&G*, pp. 215–227). This new washing plant includes a water clarifier that, although not required by state mining regulations, can recycle nearly 80–90% of the water used for mining (figure 21). Before the wastewater reaches the clarifier, it goes through a centrifugal concentrator to recover fine gold and very small sapphires (figure 22). This washing plant is also extremely close to the mining site, which dramatically increases the efficiency of ore processing.

Figure 22. Left: Potentate Mining marketing director Warren Boyd (on the right), mine geologist and manager John Rae (in the back), and a client gather around the centrifugal concentrator. Right: The concentrator extracts fine gold and very small sapphire crystals from the water coming out of the jig before it enters the clarifier. Courtesy of Potentate Mining.

Figure 23. Gemstone trader Peter Ngumbi examines rough at the sapphire mining area near Garba Tula in northern Kenya. Photo courtesy of Vter Young.

Potentate Mining sells rough and faceted sapphire at the Tucson and JCK shows to retailers and jewelry designers. Since 2016, it also offers natural, heat-treated rough sapphire by lots to clients in North America, India, Sri Lanka, and Thailand. Most of these clients are cutting operations. The COVID-19 pandemic reduced the number of staff working onsite at the mine in 2020, but the production was not dramatically affected. Due to travel restrictions, stone viewing became extremely difficult. According to marketing director Warren Boyd, lots have been shipped to clients since the start of the pandemic. While viewing ahead of receiving lots was impossible, the company expected and has accommodated a certain amount of returns from clients. With Potentate adapting to the unexpected, 2020 sales were about the same as the year before.

Tao Hsu

Peter Ngumbi (Vter Young). The pandemic has been felt throughout the entire jewelry industry, from the miners who are the first to see gems come out of the ground to the local traders and the end consumers. To get a better understanding of the situation in East Africa, we spoke to Peter Ngumbi, a third-generation Kenyan gemstone trader who sources rough from local markets and directly from the miners (figure 23). Mr. Ngumbi sells stones from his offices in Nairobi and Voi to visiting international merchants, as well as directly to consumers and hobby cutters via social media. The main focus of his business is garnet, primarily tsavorite. His broad perspective allows us to gain some insights into the East African gemstone scene during 2020.

The Kenyan government was quick to impose actions to contain the virus, such as a ban on interprovincial travel, which allowed for strong control of local outbreaks, and closed its borders to avoid importing cases while implementing a strict curfew. Mask wearing and contact tracing quickly became routine. While these measures affected daily life, they kept COVID-19 rates relatively low. Similar measures were enforced in Rwanda and Uganda with positive results.

The situation is vastly different in the neighboring country of Tanzania, where the existence of COVID-19 is officially denied and many people are losing friends and relatives. This has significantly impacted local production, which fluctuates heavily. Areas like Mahenge produce almost no material, while material is abundant in other areas because foreign buyers are no longer present.

Even though the local Kenyan restrictions were strong, Mr. Ngumbi notes some positive aspects. Most foreign buyers were forced to leave the country, and many of the local buyers were hesitant to invest large sums in the gem trade during these economically uncertain times. Suddenly he had access to larger volumes of stones with only a fraction of the usual buying public. On top of that, he returned from the 2020 Tucson shows and saw some exceptional tsavorite production, which allowed him to replenish depleted stock.

Normally, Mr. Ngumbi travels regularly to other countries in the region such as Rwanda, Malawi, Mozambique, and Tanzania to source rough. Since he has done this for many years, he has a strong network in these countries, which he relied on heavily during times of limited travel.

He feels that many traders have dramatically expanded their network into source countries over the last decade and are now relying on these established, trusted connections to supply them with rough remotely.

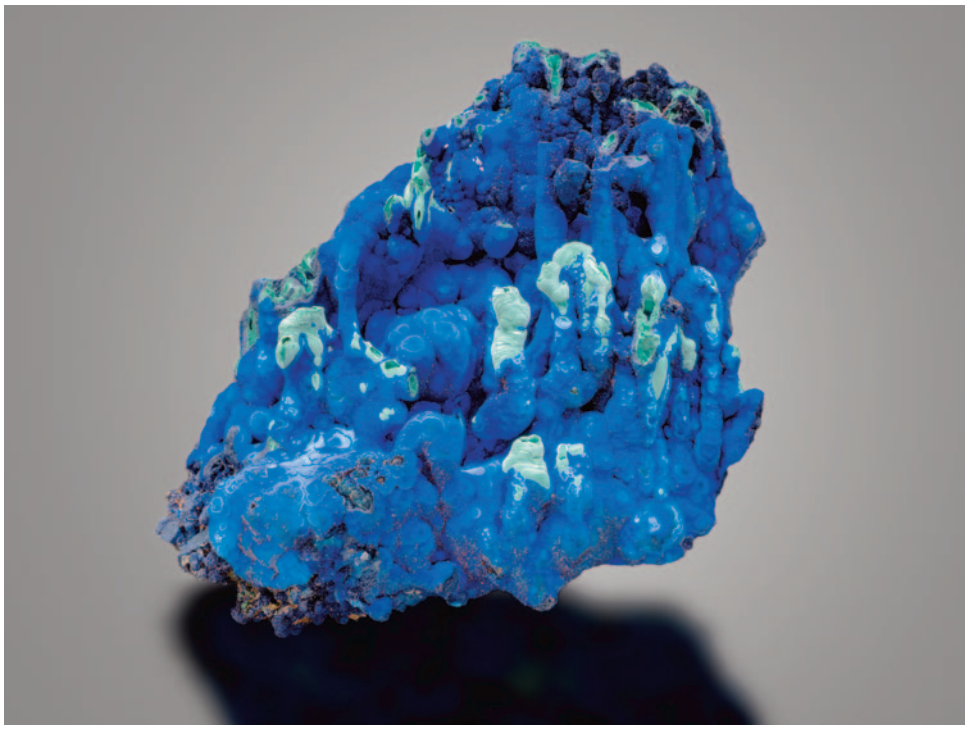

Figure 24. This 203 × 254 mm azurite mineral specimen from Bisbee, Arizona, is emblematic of the strong mineral representation of the Southwest at the Alfie Norville Gem and Mineral Museum. Photo by Jeff Scovil; courtesy of the Alfie Norville Gem and Mineral Museum.

While this was an excellent opportunity for African traders to buy rough, selling was not so rose-colored. No foreign traders came to the continent to source rough. Luckily, many of the African rough traders had established an online presence, which compensated for the decreased in-person sales. Mr. Ngumbi estimates that he sold more than three times the value he usually sells through social media, adding that the public has fully accepted this method of buying. In fact, customers in the United States were so hungry for rough that he could not keep up with orders. This includes some regular customers he sees at trade shows or in his Nairobi office, but a significant portion are unknown buyers he has never met in person. A growing number of online customers are independent jewelers who source their rough as close to the mine as possible and have it cut by contracted cutters.

Artisanal mining was also impacted by COVID-19. Kenyan authorities suspended mining operations where more than 20 people were working to avoid large gatherings. This only lasted for a few months, although it was strictly enforced by officials. These temporary suspensions affected the amount of material available in the market, but keep in mind that the number of buyers was also significantly reduced due to the absence of foreigners. Once the mining restrictions were lifted, there was an influx of artisanal miners trying their luck. This resulted in increased availability of rough in the local markets compared to other years. Availability was balanced out toward the end of the year by the reopening of international borders and the return of foreign buyers with a strong desire for rough.

In summary, the pandemic has had varying effects on the trading situation in East Africa, with local regulations having a major impact on the local supply and access to that material. The absence of foreign buyers has augmented the supply of available rough in the markets, while COVID-19 has locally disrupted production by artisanal and small-scale miners. The combined effect of this could turn out positive in some regions, while other areas are adversely affected.

Wim Vertriest

Somewhere in the Rainbow finds a home at the Alfie Norville Gem and Mineral Museum. A decade ago, a private gemstone collection was established to celebrate their beauty and stimulate curiosity and gemological education. Today, the Somewhere in the Rainbow collection has found a prominent new home.

Somewhere in the Rainbow joins the University of Arizona's renowned mineral collection consisting of 20,000 global specimens, which is also noted for its strength in minerals from the southwestern United States and Mexico. Together with the Somewhere in the Rainbow collection (a large part of it exhibited under a five-year agreement), 6,000 of the finest mineral specimens will be on exhibit (figure 24) at the new Alfie Norville Gem and Mineral Museum, located at the historic Pima County Courthouse in downtown Tucson (figure 25). The museum is on the verge of reopening in 2021, says manager Eric Fritz. Its location in Tucson is apt, given that the city is a global destination for gemstones, minerals, and the visitors who trade in them.

The museum is named after the wife of noted Tucson real estate developer Allan Norville. In the 1990s, the

couple founded the Gem and Jewelry Exchange (GJX), which remains a major force among the many shows that come to Tucson every year. To date, more than 40 gem and mineral shows exhibit across the town every January and February. The Norvilles are major patrons of the new museum.

At 1,600 pieces and counting, the Somewhere in the Rainbow collection consists mainly of finished gem mate-

Figure 25. The Alfie Norville Gem and Mineral Museum will be housed at Tucson's recently refurbished Pima County Courthouse. The building renovation cost over US$30 million. Courtesy of the Alfie Norville Gem and Mineral Museum.

Figure 26. An architectural rendering of the gem gallery at the museum includes build-out cases and exhibits costing almost US$12 million. Courtesy of the Alfie Norville Gem and Mineral Museum.

rial complementing the mineral displays (figure 26). Its strength lies in gem carvings, loose gemstones, and jewelry. This collection has traveled across the United States in recent years, visiting AGS Guild stores and other high-end retailers. Its mission is "to bring hands-on education and enjoyment of fine colored gems to museums, galleries, gemologists, and facilities dedicated to preserving the rarity, history, and beauty of the gems and articles of jewelry."

Shelly Sergent, the Somewhere in the Rainbow collection's manager, is credited with building it at the behest of unnamed patrons. She says that it offers the public, students, scientists, and educators a distinct snapshot of the gemstone supply chain. "Mother Nature gives us rocks. Cutters and carvers give us gemstones, and jewelry designers give us heirlooms," Sergent explains.

The collection provides enthusiasts with a better understanding of the beauty and rarity—as well as the unique collaboration between nature and artists. "I realize truly that our mission is not only about education—it's about community," says Ms. Sergent. "In that regard, we have brought together more than 127 different people that have worked with us in some capacity on this collection, whether that be miners, stone chasers, lapidary artists, designers, jewelers, and the heads of different laboratories."

Ahead of the Alfie Norville Gem and Mineral Museum's 2021 reopening, GIA had the opportunity to visit with Sergent to examine, handle, and photograph some of the collection's significant pieces. The accompanying photo gallery offers just some of the highlights.

Robert Weldon
GIA, Carlsbad

Photo Gallery: The Alfie Norville Gem and Mineral Museum

A: A rendering of the gem gallery at the Alfie Norville Gem and Mineral Museum in Tucson. B: A rare 1.92 ct cobalt blue spinel from Vietnam. C: This ring features a fine 5.17 ct ruby from Myanmar flanked by two yellow sapphires.

Photos by Robert Weldon/GIA; courtesy of Somewhere in the Rainbow.

D: "Da Vinci," a 177.8 mm tall green beryl from the Ural Mountains, carved by Alfred Zimmerman of Idar-Oberstein, Germany. The goldwork was crafted by American designer Henry Dunay. E: American gem carver and goldsmith Darryl Alexander fashioned this carved agate pen set in 18K gold and accented with sunstone and diamonds. The agate is approximately 203 mm long. F: A classic necklace featuring a 13.57 ct tsavorite garnet from Tanzania, including 4.27 carats of diamonds, designed by Shelly Sergent, Harry Tutunjian, and Evelyn Crommet.

G: A 34.34 ct Imperial topaz from the Ouro Preto region of Brazil is the centerpiece of this stunning pendant featuring 10.50 carats of diamonds and set in 18K gold and platinum by designer Eddie Sakamoto.

H: The "Buddha Blue," a 15 ct sapphire purportedly fashioned between 1400 and 1500 CE in Ceylon. I: An 18.55 ct Tanzanian red spinel. J: A bracelet by Megan Schmitt featuring a 20.06 ct blue Sri Lankan sapphire, with pink and yellow sapphires. K: A pair of grossular garnets: the 21.56 ct "Heart of Merelani" (left) from Tanzania and the 20.20 ct "Scorpion King" (right), mined by Campbell Bridges in Kenya. L: Pendant with a 15 ct pear-shaped Paraíba tourmaline from the original Brazilian mine. M: Necklace by Vlad Yavorskyy with 129.93 carats of spinel from Myanmar, Sri Lanka, Afghanistan, and Madagascar.

REGULAR FEATURES

COLORED STONES AND ORGANIC MATERIALS

"C" is for cookie and "G" is for geode. Gemstones are well known for their ability to mimic familiar themes, but the rock that recently launched a thousand online posts resembled one of the most recognizable children's characters, the Muppet known as the Cookie Monster (figure 27). The uncanny likeness set the internet ablaze with reports from news sources around the globe. A video of the geode featuring Cookie Monster's signature tune, "C is for Cookie," was uploaded to Facebook by its owner, gem collector Mike Bowers, on January 16, 2021. The viral clip reached more than one million views just a week later. All the attention left many wondering, "How could a rock like this form?"

The discovery of the Cookie Monster geode, reportedly from Brazil, is a combination of geologic design and pure luck. It is composed of banded layers of microcrystalline quartz, commonly known as agate. The scientific processes required are complex but can be simplified into some general steps (J.D. Winter, *Principles of Igneous and Metamorphic Petrology*, Pearson Prentice Hall, Upper Saddle River, New Jersey, 2013). This type of geode occurs as a secondary formation when gas bubbles trapped in volcanic rocks, known as vesicles, are filled with silica-rich fluids. Over time, the fluids deposit concentric layers of microcrystalline quartz along the interior of the vesicle. The accumulation of these layers reflects the variation in chemistry and changing conditions of the silica-rich fluid. These fluctuating conditions can result in a banded formation of the microcrystalline quartz, thus giving rise to an agate. The final siliceous fluid in the last stage of formation allowed for a large central druzy quartz–lined cavity that represents the "mouth" of the Cookie Monster (figure 28, top).

Cutting the rock at the perfect angle to reveal such a startling semblance was a matter of sheer chance, for the internal structure of a geode is not known until it is split open (https://www.gia.edu/gems-gemology/spring-2021-gemnews-cookie-monster). Any slight change in cutting direction might have resulted in viewers not experiencing the phenomenon of *pareidolia*, the tendency to assign familiar shapes or faces to abstract forms (Winter 2007 Lab Notes, pp. 363–364).

Figure 27. A Brazilian geode shows a striking resemblance to the legendary Cookie Monster character. The intact geode measures 61 mm in length and 40 mm in diameter. Photo by Robert Weldon; courtesy of Mike Bowers.

Figure 28. This geode was serendipitously cut at a perfect angle, resulting in halves resembling the famous Cookie Monster (top). Coincidentally, the geode also showed blue fluorescence under long-wave ultraviolet light, reminiscent of the character's blue fur (bottom). Photos by Robert Weldon; courtesy of Mike Bowers.

Figure 29. A small impurity of yellow limonite resembling a cookie crumb was found under the "mouth" of the Cookie Monster. Photomicrograph by Nathan Renfro; field of view 4.70 mm.

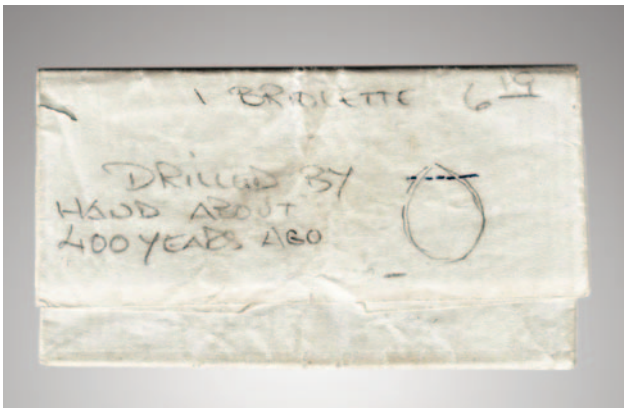

Figure 30. The diamond paper that held the 6.19 ct briolette diamond. Photo by Nathan Renfro.

The color in blue agate is created by scattering of light; when the particles of silica are smaller than 400 nm, blue light is reflected back (G. Rossman, "Cause of color in agate and chalcedony," Seventeenth Annual Sinkankas Symposium, April 24, 2021). When the rock was exposed to long-wave ultraviolet light, it revealed strong blue fluorescence (figure 28, bottom) consistent with the fur color of the famous Muppet. Also of gemological interest was a microscopic feature: Below the quartz-lined "mouth" was a small inclusion of yellowish limonite, a hydrous iron oxide, resembling a cookie crumb (figure 29).

While geodes can be millions of years old, the Cookie Monster character only emerged within the last century. The Cookie Monster, originally created as a prototype in 1966 by Jim Henson, debuted on the American educational children's television series *Sesame Street* in 1969. The name was taken from his incessant obsession with the baked goods. With *Sesame Street* still on the air today, after 51 seasons, Cookie Monster's fame is sealed in pop culture.

It was a fortuitous circumstance that the formation of the geode resulted in such a remarkable specimen. As GIA analytical microscopist John Koivula likes to say, "Mother Nature cooks in a dirty kitchen." Who knows what she will cook up next, but one can hope it has us all cracking open a smile once more.

Britni LeCroy and Nicole Ahline
GIA, Carlsbad

DIAMONDS

Hole drilled by hand in briolette. Recently, a 6.19 ct briolette diamond was submitted to GIA's Antwerp laboratory for examination. It had been in the family of Belgian diamond cleaver and Auschwitz survivor Philip Isidoor Frank, who died in 1982. Mr. Frank is known for his work on many important diamonds, such as the 69.42 ct D-color Internally Flawless pear-shaped Taylor-Burton diamond. The diamond paper containing the briolette had a note, presumably written by Mr. Frank: "drilled by hand about 400 years ago" (figure 30). Sadly, this cannot be substantiated, and Mr. Frank left no other record. It raises the question as to whether this age is theoretically possible.

The diamond (figure 31) loosely fits the briolette definition since the hole is at the very tip rather than through the central portion. In reference to Mr. Frank's note on the diamond paper, this description seems appropriate, even though the stone lacks the appealing teardrop shape we think of with modern briolettes. The style of faceting for this diamond is reminiscent of early cutting from India (1550–1900), but it could have been cut at any time (figure 32). By the 1700s, Europeans were already moving toward

Figure 31. The facet arrangement of the 6.19 ct briolette. The horizontal drill hole is at the top. Photo by Jian Xin (Jae) Liao.

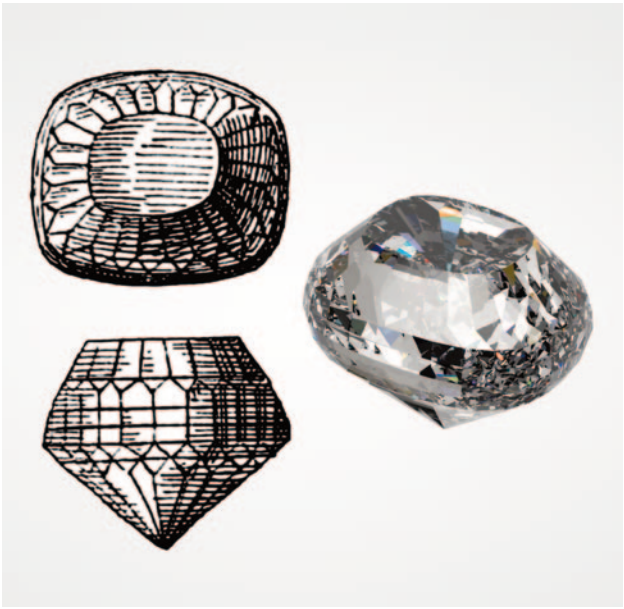

Figure 32. Early Indian cutting styles (ca. 1550–1900) feature a very thick girdle area with multiple facets, similar to the briolette's plane that wraps around the stone. From Ogden (2018), p. 320.

variations of brilliant styles with good symmetry, thin girdles, and specific ratios of crown and pavilion. They did not typically care for the quality of Indian diamond cutting, and many stones were recut.

The briolette cutting style has a remarkably long history. Seventeenth-century French gem merchant Jean Baptiste Tavernier (1676, p. 336) sold four briolettes to the French king Louis XIV. The invoice described two stones as "round pendant with little facets" and "cut with facets on all sides" (Bapst, 1889, p. 404), respectively, and included illustrations. Two others, not illustrated, were "cut as round pendants with facets on all sides." Tavernier's drawings depict a briolette style, although that term was not used much before the nineteenth century.

However, Tavernier's gems are not the earliest recorded briolettes. One had arrived in the royal court in England almost 20 years before his first voyage to India. On February 17, 1612, payment was arranged to the Flemish goldsmith Stephen le Gouche for a piece of jewelry with "one fair large pendant diamond, cut with fancies [facets] on all sides, and pierced at the top" that had been delivered to Queen Anne of Denmark (Green, 1858, p. 121), who was married to James VI and I (r. 1603–1625). The court accounts further describe the piercing at the top as lateral.

Noël-Antoine Pluche's extensive multivolume work on natural history, *Le Spectacle de la Nature*, features an illustrated briolette described as a pear-shaped diamond cut in the "*taille à l'Indienne*" or Indian style (1748, pp. 349–352). The comments by Pluche, along with the Indian examples traded by Tavernier, point to the briolette form as being associated with India. Several later books specifically state this association and even mention lateral piercing. A French encyclopedia from 1859 (Guillaumin, pp. 980–981) explains that "In India, where the briolettes formerly came from, it was customary to pierce them with a very small hole in the upper part. Today a few lapidaries in Amsterdam cut briolettes very well, but they haven't yet managed to pierce them."

By 1600, Italian, German, Flemish, and Belgian cutters worked in India (Everaert, 2000, 2005), bringing along their techniques and cutting styles to higher-quality rough. These faceted stones would then be sent to Europe (Ogden, 2018, pp. 297–305). For example, the briolette shown in Tavernier's book may have been cut by a European living in India rather than by a local Indian diamond cutter (there is no mention of a hole in the briolettes sold by Tavernier). Indian diamond cutters continued to follow their own styles, often cutting the lesser-quality rough destined for the Indian market. Short of documentation showing early briolettes with this specific facet arrangement by Indian cutters, dating the 6.19 ct briolette from Mr. Frank is impossible.

The drill hole at the tip of this briolette (figure 33) is consistent with sawing techniques used to make holes in diamonds from the seventeenth century through the 1970s. By the mid-1500s, iron wires coated with diamond dust and oil were used to saw through a diamond. By the early 1600s, lapidaries rotated a diamond-tipped iron point or iron drill with diamond powder to create a hole from each side. Once these two holes met and the opening was large enough, the wire was inserted and drawn back and forth, the apparent method used for this diamond.

In 1811, Napoleon Bonaparte presented a 263 ct diamond briolette necklace to his empress consort, Marie Louise. It featured 19 oval- and pear-shaped briolette-cut

Figure 33. The drill hole at the tip of the stone. Note the unique surface, a remnant of the process of drawing a wire coated with diamond dust and oil back and forth. Photomicrograph by Nathan Renfro; field of view 4.02 mm.

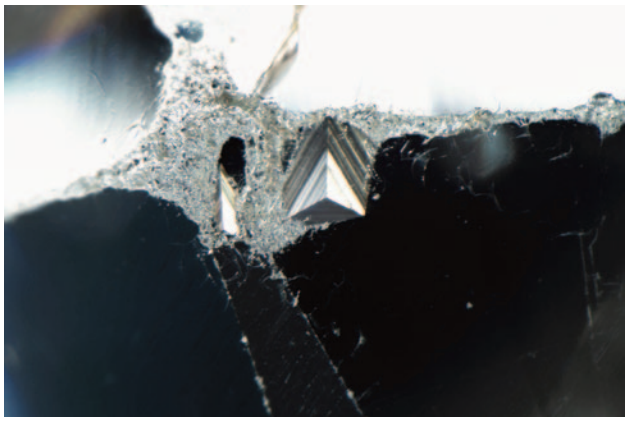

Figure 34. The trigon is a remnant of the original crystal's surface. Photomicrograph by Christopher Vendrell; field of view ~1.99 mm.

diamonds (probably of Indian origin but faceted by European cutters in India) with drill holes. The facet arrangements of the stones in the necklace are more symmetrical and quite different from the 6.19 ct briolette.

It is unclear when laser drilling for larger holes began, but General Electric researchers used a laser to drill 0.02-inch-diameter holes into an industrial diamond in the early 1960s (Overton, 2008, p. 46). As early as 1970, GIA's Robert Crowningshield reported that lasers were being used as part of a process to bleach or dissolve dark inclusions, and soon this treatment was widely available to members of the trade (Overton, 2008, p. 46). This means that sometime after the 1970s, lasers would have been employed for the process of drilling holes for beads and such. Older briolettes that came into GIA's laboratory would still have holes drilled by hand, but by the 1980s, this hand drilling process was mostly abandoned. Has GIA seen a handmade drill hole in diamonds in the past, and if so, how many? Uncovering records of hand-drilled diamonds submitted to the laboratory is quite difficult since records prior to the 1990s are not computerized for searching and briolettes are rarely seen. Notations about the surface of the drill hole are also uncommon in reports. Our research into past submissions did not yield any useful results.

From the above, it is impossible to date this diamond, although it was probably cut before 1920 in India, possibly much earlier, but not by highly skilled cutters.

The briolette is heavily abraded. One possible reason is that it was kept in a diamond parcel rubbing against other diamonds for a long time, though this seems unlikely. Why would any diamond merchant allow a diamond in their stock to become so excessively abraded? It was more likely worn in an item of jewelry, repeatedly wearing against other diamonds and being casually stored by the owner, suggesting an extended period of use.

Of final note, there are several naturals on the surface of the briolette, including a trigon (figure 34).

References

Bapst G. (1889) *Histoire des Joyaux de la Couronne de France d'Après des Documents Inédits*. Hachette, Paris.

Everaert J. (2000) Soldiers, diamonds and Jesuits: Flemings and Dutchmen in Portuguese India, 1505–90. In A. Disney and E. Booth, *Vasco Da Gama and the Linking of Europe and Asia*, Oxford University Press, Oxford, UK, pp. 84–104.

Everaert J. (2005) Shifting the 'diamond connection': Antwerp and the gem trade with Portuguese India (1590–1635). In F. da Silva Gracias et al., Eds., *Indo-Portuguese History: Global Trends. Proceedings of XI International Seminar on Indo-Portuguese History, Silver Jubilee Session, Dona Paula, Goa, 21st-25th Septembre, 2003*, pp. 315–335.

Green M.A.E., Ed. (1858) *Calendar of State Papers, Domestic Series, of the Reign of James I: 1611-1618, Preserved in the State Paper Department of Her Majesty's Public Record Office*. London.

Guillaumin M. (1859) *Dictionnaire universel théorique et pratique du commerce et de la navigation*. Guillaumin, Paris.

Ogden J. (2018) *Diamonds: An Early History of the King of Gems*. Yale University Press, New Haven, Connecticut, 403 pp.

Overton T. (2008) A history of diamond treatments. *G&G*, Vol. 44, No. 1, pp. 32–55.

Pluche N.A. (1748) *Le spectacle de la nature, ou Entretiens sur les particularités de l'histoire naturelle* ... Vol. 3, Part 2. Estienne, Paris.

Tavernier J.B. (1676) *Les Six Voyages de Jean Baptiste Tavernier (…) en Turquie, en Perse, et aux Indes* (…). Gervais Clouzier et Claude Barbin, Paris.

Marc Verboven
GIA, Antwerp

Al Gilbertson
GIA, Carlsbad

Jack Ogden
London

SYNTHETICS AND SIMULANTS

Phenakite as a diamond imitation. In my gemological laboratory, I see some interesting imitations from time to time. The latest was quite unusual: a set of 12 loose stones submitted as diamond (figure 35) for certification. Testing their thermal conductivity with a Presidium Gem Tester and their electrical conductivity with a Ceres Secure II device indicated diamond and ruled out synthetic moissanite. The next property examined was fluorescence, and all the stones were completely inert to both short-wave and long-wave UV. It would be unusual for a group of 12 natural diamonds to all be inert, so the next step was determining whether they might be laboratory-grown diamonds. Working under the assumption that they were indeed diamonds as submitted, the stones were tested for short-wave UV transparency and all were very transparent, suggesting they could be type IIa (which would be consistent with laboratory-grown near-colorless diamonds). Finally, I performed Raman analysis; instead of a sharp diamond peak at 1332 cm^{-1}, it showed only a small peak at 878 cm^{-1}, indicating that these stones were not diamonds.

Only then did I remember a natural crystal of phenakite, sold as diamond, that I tested a few years ago. It was very similar to natural rough diamond, but instead

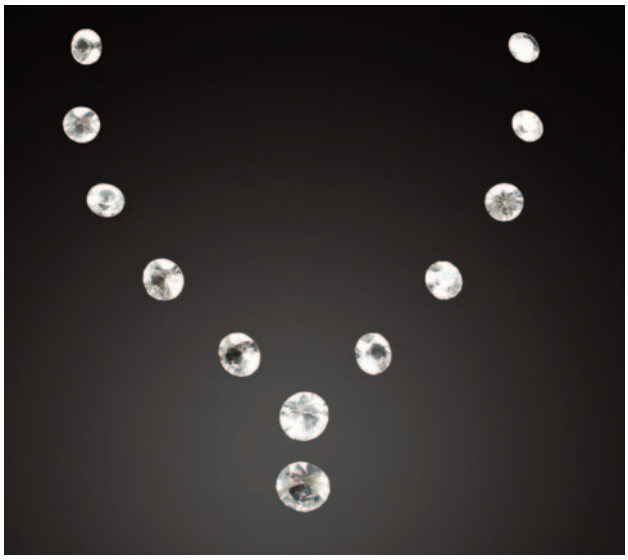

Figure 35. A set of phenakite gems ranging from 0.20 to 0.98 ct, with a total weight of 5.85 carats, sold as diamonds. Photo by J. Hyršl.

of typical trigons, it had a surface covered by many rhombs. But its thermal conductivity was the same as diamond's, and therefore it was a plausible diamond imitation for a mineral or gem dealer without knowledge of crystallography. When I remembered this, the identification was easy—the refractive index of the loose cut stones was 1.655–1.670, and the Raman line matched very well with phenakite. And upon further examination, the stones appeared doubly refractive in the microscope and polariscope.

Phenakite is trigonal Be_2SiO_4, colorless, and similar to beryl. Normally it forms hexagonal prismatic crystals that look very different from diamond. Nevertheless, some crystals from Nigeria are irregularly developed (figure 36) and could be mistaken for a rough diamond without careful examination, especially if mixed with real diamonds. Cut stones are quite rare and well known only to collectors of rare gemstones. Distinguishing a cut phenakite from diamond is quite easy when one can measure refractive index, see a double refraction in the polariscope or microscope, or calculate weight from measurements. Much more difficult would be phenakite set in jewelry, where it can be very difficult to measure RI. Cut phenakite has much lower brilliance than diamond, of course, but can resemble low-quality cut diamonds.

Figure 36. Natural phenakite crystal from Nigeria, width 38 mm. Photo by J. Hyršl.

Jaroslav Hyršl (hyrsl@hotmail.com)
Prague

TREATMENTS

An unusual treated agate presented as "Shi Zi Hong" agate from Liangshan. "Nanhong" agate, an attractive form of agate, mainly ranges from orange-red to purplish red, and is colored by the presence of fine-grained hematite inclusions. *Nan* and *hong* mean "south" and "red," respectively. The material has gained great popularity in China's domestic gem market in recent years. "Shi Zi Hong" agate, one of the most famous color varieties of "Nanhong" agate (Lin Li, "Analysis of gemological and petrological characteristics of Nanhong agate from Liangshan," Chengdu University of Technology, China, pp. 17–18), usually has a more vibrant saturated orange-red color and fine texture, so its price is higher. *Shi zi* and *hong* mean "persimmon" and

Figure 37. This 5.74 ct treated agate sample (left) submitted to the lab resembled "Shi Zi Hong" agate (right). Photo by Su Xu.

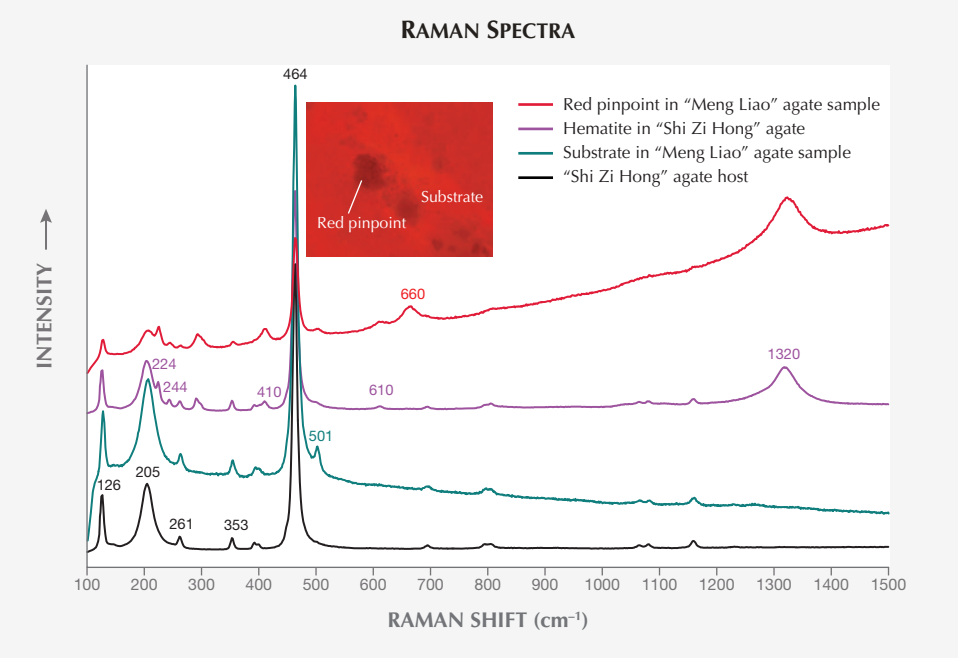

Figure 38. Under magnification and using fiber-optic illumination, some fine pinpoints were distributed as hazy clouds in the rough agate. Raman spectroscopy identified the main constituent of substrate in the sample as quartz (green trace) and red pinpoint as hematite (red trace), both consistent with "Shi Zi Hong" agate (indicated by the purple trace and the black trace). The sample also showed a sharp peak at 501 cm^{-1} and a broad band at 660 cm^{-1}, neither of which are seen in genuine "Shi Zi Hong" agate. Photomicrograph by Su Xu; field of view 0.22 mm. Spectra offset for clarity.

"red." The majority of fine-quality Shi Zi Hong agate on the market has come from Liangshan Yi Autonomous Prefecture in Sichuan Province, China.

In October 2020, an orange-red cabochon sample was presented to the National Gold-Silver Gem & Jewelry Quality Supervision & Inspection Center (Sichuan) by a client who claimed it was a new type of Shi Zi Hong agate. The trader referred to it as "Meng Liao" agate (figure 37, left).

The sample weighed 5.74 ct, and the appearance was similar to Shi Zi Hong agate (example shown in figure 37, right). The spot RI reading was around 1.54, and the sample was inert to UV radiation. Microscopic examination showed cryptocrystalline texture with red pinpoint-like inclusions scattered throughout, most of which were sufficiently fine to appear as hazy clouds under 40× magnification.

Raman spectra of the substrate and red pinpoints were obtained using 532 nm laser excitation. According to the RRUFF online database, peaks at 126, 205, 261, 353, and 464 cm^{-1} indicated that the main constituent of the substrate was quartz, while the red pinpoints matched that of hematite, with peaks at 224, 244, 291, 410, 610, and 1320 cm^{-1} (figure 38). Both were consistent with Shi Zi Hong agate. A sharp peak at 501 cm^{-1}, seldom observed in Shi Zi Hong agate, appeared in the spectra of the sample. This significant peak was assigned to stretching vibrations of $(SiO_4)^{4-}$ in the moganite structure. Based on a negative correlation between the relative content of moganite and the crystallinity of agate (Zhou Dan-yi et al., "Study on the relationship between the relative content of moganite and the crystallinity of quartzite jade by Raman scattering spectroscopy, infrared absorption spectroscopy and X-ray diffraction techniques," *Rock and Mineral Analysis*, Vol. 3-4, No. 6, 2016, pp. 652–658), we concluded that the crystallinity of natural Shi Zi Hong agate was much higher than that of the sample. Another obvious anomaly was the broad band at 660 cm^{-1}, which was found in the spectrum of the sample but was seldom observed in Shi Zi Hong agate, and this deserved further investigation.

The client admitted that the "Meng Liao" agate was actually a normal brownish yellow agate heated by a low-temperature process. Meanwhile, he loaned us an untreated rough stone (figure 39) for Raman analysis of its body and very fine yellow pinpoint inclusions.

The substrate of the untreated rough stone and the "Meng Liao" agate sample submitted to the lab showed almost the same peaks in the region of 1000–100 cm^{-1}, suggesting that they might be homologous with each

Figure 39. The untreated brownish yellow rough stone, approximately 17.0 × 22.0 × 1.5 mm, loaned by the client for analysis. Photo by Xiaoping Shi.

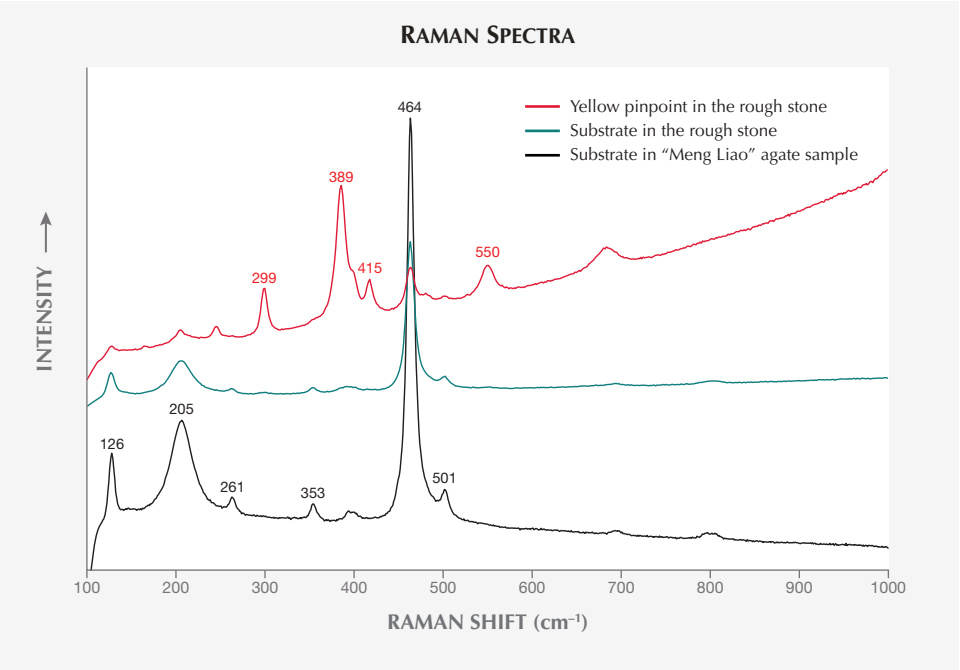

Figure 40. Raman spectra of the brownish yellow rough stone: Peaks at 299, 389, 415, and 550 cm^{-1} indicated goethite. Peaks at 126, 205, 261, 353, 464, and 501 cm^{-1} were consistent with the treated agate sample submitted to the lab. Spectra are offset for clarity.

other. The spectrum of the yellow pinpoint, exhibiting peaks at 299, 389, 415, and 550 cm^{-1} and lacking a 660 cm^{-1} band, matched the Raman spectrum for goethite and was related to the formation of color in the rough, as shown in figure 40. According to a previous report (D.L.A.de Faria and F.N. Lopes, "Heated goethite and natural hematite: Can Raman spectroscopy be used to differentiate them?" *Vibrational Spectroscopy*, Vol. 45, No. 2, 2007, pp. 117–121), the disordered hematite structure was initially formed by dehydration and caused the relative intense band at 660 cm^{-1} by heating goethite at a low temperature (~140°C to 360°C). The natural hematite in Shi Zi Hong agate, by contrast, has features including a very weak 660 cm^{-1} band and a high degree of order, by which genuine Shi Zi Hong agate can be distinguished from the brownish yellow agate that acquired an orange-red color by artificially heating goethite. These results show that the agate submitted by the trader as "Meng Liao" agate, resembling Shi Zi Hong agate, can be readily detected by its unique Raman spectrum displaying an obvious broad band at 660 cm^{-1} and a sharp peak at 501 cm^{-1}. Consumers in the market for Shi Zi Hong agate should watch out for this treated material.

Su Xu and Dapeng Chen
National Gold-Silver Gem & Jewelry Quality Supervision & Inspection Center (Sichuan)

Xiaoping Shi
Sichuan Provincial Coal Design & Research Institute
Chengdu, China

Unusual fluorescence of a color-enhanced amber bracelet. Heat treatment is commonly applied to amber, mainly to improve its color or transparency. The method of heat treatment to enhance the color of amber is informally called a "baking process," which refers to the process of heating while applying pressure and adding oxygen (Y. Wang et al., "Experimental studies on the heat treatment of Baltic amber," Summer 2014 *G&G*, pp. 142–150). Usually, the light yellow amber will be darkened and turned brownish yellow or brownish red by such a process to increase its market value. Amber may also be heated to produce sun spangles and sold as "flower amber" for its popular demand in the market.

A bracelet recently sent to Taiwan Union Lab of Gem Research (TULAB) for identification services contained amber that was pale brownish yellow, transparent, and slightly included (figure 41). Raman spectroscopy and microscopy confirmed the gems to be natural amber with an abundance of sun spangles, which were discoidal fractures caused by heat treatment.

Color enhancement of amber is generally not detectable unless the amber itself has cracks or pores extending to the surface during the baking process, in which case the color usually concentrates in these cracks and pores. Apart from that, amber that is color-enhanced by the baking process mostly shows inert or faint yellow fluorescence under long-wave ultraviolet light; however, such fluorescence may also occur in natural untreated amber.

Microscopic observation of the amber bracelet revealed that the dark brown color was concentrated in all the surface-reaching fractures or sun spangles, but the sun spangles wrapped inside all appeared in a lighter tone of yellow (figure 42). Thus, it was suspected that this amber bracelet had been baked to enhance color.

In addition to the inclusion evidence, the amber bracelet's long-wave ultraviolet fluorescence reaction unexpectedly presented a relatively bright blue along the

Figure 41. This bracelet contained amber (approximately 10 mm each) that was color-enhanced by a baking process. Photo by Yu-Shan Chou.

ridgelines and inert to faint yellow on the rest of the stone (figure 43). This abnormal fluorescence strongly indicated that the amber had indeed been baked to enhance its color and that the ridgelines were worn due to grinding or wearing, which removed the brown surface layer. This case is worthy of attention because a series of similar items have subsequently been submitted for identification. Traditionally, the color enhancement of amber has been confirmed only by inclusion evidence; however, the abnormal fluorescence of this object offered supporting evidence.

Shu-Hong Lin
Institute of Earth Sciences,
National Taiwan Ocean University
Taiwan Union Lab of Gem Research, Taipei
Yu-Shan Chou and Kai-Yun Huang
Taiwan Union Lab of Gem Research, Taipei

Figure 42. Magnification revealed that the dark brown color was concentrated in the surface-reaching fractures or sun spangles, yet the sun spangles or fractures wrapped inside the amber were all yellow. Photomicrograph by Shu-Hong Lin.

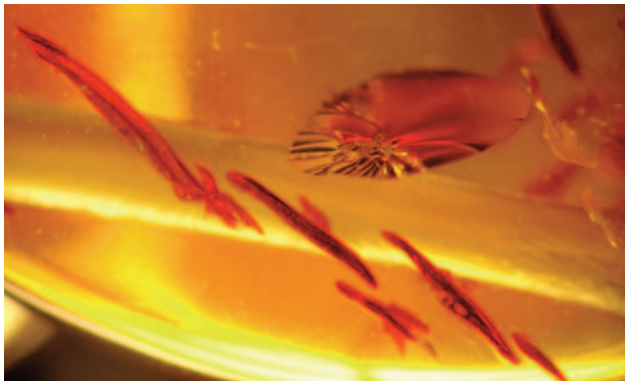

Figure 43. Under long-wave ultraviolet light, the amber bracelet presented a surprising bright blue fluorescence on the ridgelines and inert or faint yellow fluorescence on the other parts. Photo by Kai-Yun Huang.

ANNOUNCEMENTS

Fourth annual Gianmaria Buccellati Foundation Award. Belle Sin Ting Wong, a graduate of GIA's Jewelry Design program in Hong Kong, received the fourth annual Gianmaria Buccellati Foundation Award for Excellence in Jewelry Design. This year, the prestigious award was announced virtually due to the global pandemic shuttering the Tucson gem shows. Sin Ting Wong (figure 44) was one of nine finalists selected from a competing group of more than 100 students from GIA's seven campuses. Her winning design was inspired by the Siamese fighting fish and features diamond, sapphire, pearl, jadeite, and enamel set in 18K yellow and white gold.

Sin Ting Wong hopes to raise environmental awareness through this brooch design and advocates the use of sustainable products or "we might be very close to losing these beautiful creatures and quicken the pace of global warming."

She will travel to Italy, where she will have the opportunity to meet Rosa Maria Bresciani Buccellati, the president of the foundation.

Laurie Bailyn, GIA senior manager of jewelry manufacturing arts, said, "It is incredible that so many students managed to complete their Jewelry Design studies in 2020, despite the challenges of the global pandemic. Many of the beautiful, original designs that students created this year were inspired by themes of connection and community."

The 2021 Gianmaria Buccellati Foundation Award for Excellence in Jewelry Design competition is currently open to GIA Jewelry Design students who meet the eligibility requirements. For more information on entering the competition, visit gia.edu/buccellati-foundation-award-jewelry-design

Figure 44. Belle Sin Ting Wong received the Gianmaria Buccellati Foundation Award for Excellence in Jewelry Design for her diamond, sapphire, pearl, jadeite, and enamel brooch, inspired by the Siamese fighting fish. Photo by Johnny Leung and Tony Leung.

IN MEMORIAM

Jean Claude Michelou. The colored stone industry lost one of its true leaders with the passing of Jean Claude Michelou (figure 45) on May 3 at the age of 72. Mr. Michelou graduated from the London School of International Business and began selling emeralds in Colombia in 1977. The business he later established, Imperial Colors Ltd., specializes in rough buying, grading, and cutting of emerald, tourmaline, beryl, and sapphire. He relocated the company to Bangkok in 2018.

Mr. Michelou was active with the International Colored Gemstone Association (ICA), serving as a board member for 18 years and as vice president for 10 years. In 2004, he founded ICA's quarterly magazine, *InColor*, and was its editor-in-chief until his retirement earlier this year. He was also a consultant for the United States Agency for International Development (USAID), the World Bank, and other agencies on developing standards for the colored stone industry. In addition, he served on the advisory board for the University of Delaware's Gemstones and Sustainable Development Knowledge Hub and organized the World Emerald Symposiums held in Bogotá since 2015.

For more than a decade before his passing, Mr. Michelou had been deeply involved in several beneficiation projects in source countries, including the Swat Valley emerald deposits of Pakistan and a Nigerian sapphire mining venture. He shared his insights on supply chain transparency and beneficiation with *G&G* in the Spring 2018 issue (Gem News International, pp. 93–94). Over the years, Mr. Michelou was a valuable source of knowledge for this journal and a mentor to many young industry professionals. We extend our condolences to his family and friends.

ERRATUM

In the Winter 2020 article by Sudarat Saeseaw et al. ("Low-temperature heat treatment of pink sapphires from Ilakaka, Madagascar," pp. 448–457), the photo of sample PS11 after heating was incorrectly presented in table 1. The correct photo is shown in the online version of the article, available at https://www.gia.edu/gems-gemology/winter-2020-ilakaka-pink-sapphires-heat-treatment

Figure 45. Colored stone industry veteran Jean Claude Michelou was founder and longtime editor-in-chief of ICA's quarterly, InColor. *Photo by Vincent Pardieu.*

Micro-Features of Spinel

Synthetic or Treated

This Russian flux-grown spinel contains a brownish net-like inclusion of flux. Field of view 1.43 mm.

Larval-shaped elongate gas bubbles are characteristic of Verneuil (flame-fusion) laboratory-grown spinel, as seen in this cobalt-colored example. Field of view 1.79 mm.

Verneuil (flame-fusion) spinel with a red color is relatively uncommon, but curved striae are diagnostic of its laboratory-grown origin. Field of view 3.52 mm.

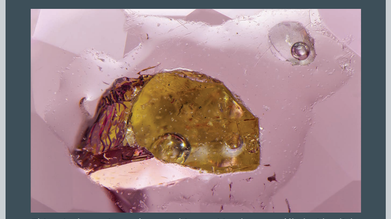

This spinel contains surface-reaching cavities that were filled with a light yellow resin. Trapped gas bubbles are also present in the filler. Field of view 4.91 mm.

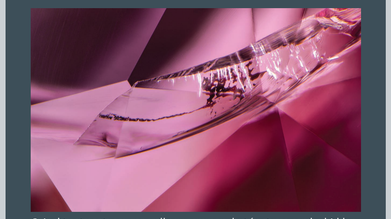

Spinel treatments are generally uncommon, but fractures can be hidden from view by clarity enhancement with oil or resin. Trapped high-relief gas bubbles are diagnostic of clarity enhancement in this pink spinel. Field of view 4.02 mm.

Natural

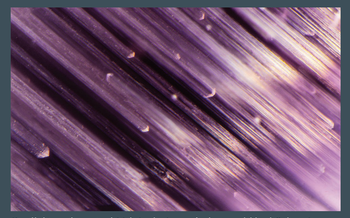

Parallel translucent whitish inclusions of what could be högbomite create chatoyancy in this cat's-eye spinel from Elahera, Sri Lanka. Field of view 3.09 mm.

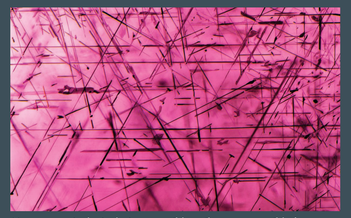

Numerous acicular inclusions, possibly rutile, are responsible for causing asterism in the form of a six-rayed star in this spinel from Okkampitiya, Sri Lanka. Field of view 3.38 mm.

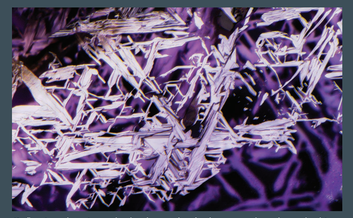

Reflective platy, jagged-edged crystals of sphene are densely packed in this star spinel from Ratnapura, Sri Lanka. Many of the sphene crystals display twinning. Field of view 1.83 mm.

Crystallographically aligned triangular etch features are present on the octahedral face of this spinel, as seen using differential interference contrast microscopy. Field of view 0.72 mm.

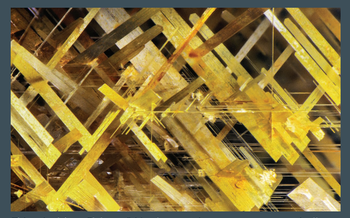

This spinel from Elahera, Sri Lanka, contains numerous geometrically arranged limonite-stained laths. Field of view 4.02 mm.

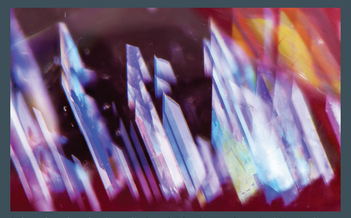

Vibrantly colored polysynthetic twinning is prominent in this spinel from Morogoro, Tanzania. Field of view 1.80 mm.

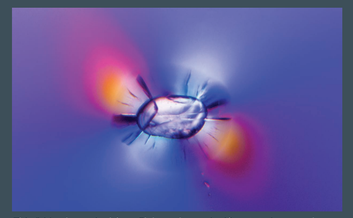

This Sri Lankan spinel from Elahera shows significant strain around a colorless zircon crystal using polarized light. The strain pattern becomes quite colorful with the addition of a first-order red compensator. Field of view 0.91 mm.

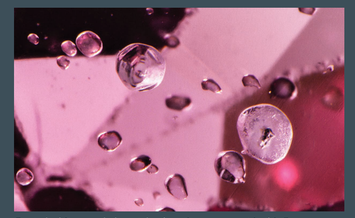

Frosted white rounded crystals of apatite are present in this Burmese spinel. Some also contain small black crystals of graphite or ilmenite. Field of view 3.23 mm.

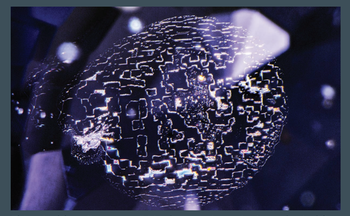

This spinel from Ratnapura, Sri Lanka, contains an intricate classical fingerprint pattern extending from a solid mineral crystal. Field of view 1.30 mm.

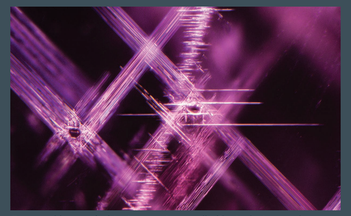

Rows and layers of white intersecting needle-like inclusions such as these are characteristic of spinel from Vietnam. Field of view 1.83 mm.

This Burmese spinel contains a cluster of well-formed octahedral negative crystals filled with white dolomite and black graphite. Field of view 2.37 mm.

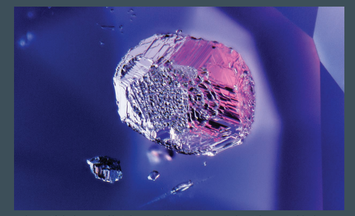

A beautiful cluster of bright metallic pyrite crystals with a wrinkled texture is seen in this spinel from Kuruwita, Sri Lanka. Field of view 2.96 mm.

A large complex three-phase fluid inclusion with numerous solid daughter crystals is contained in this spinel from Tajikistan. Field of view 0.96 mm.

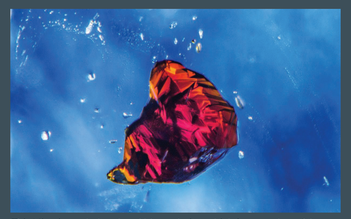

This Nigerian cobalt-colored blue gahnite, which is a member of the spinel group, contains a red-brown crystal of sphalerite. Field of view 0.91 mm.

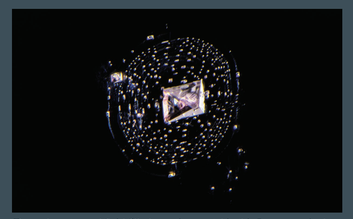

The carbonate- and fluid-filled negative crystal in this Burmese spinel resembles a solar system with concentric rings of tiny octahedral negative crystals. Field of view 1.30 mm.

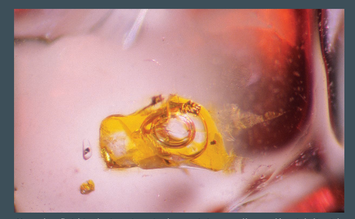

Complex fluid inclusions in spinel containing a yellow sulfur-rich liquid are diagnostic of Burmese origin. Field of view 3.60 mm.

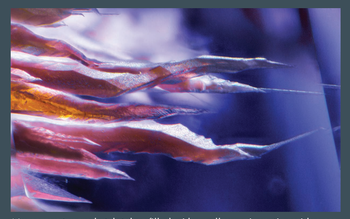

Numerous tapered etch tubes filled with a yellow epigenetic residue are contained in this violet spinel. Field of view 1.79 mm.

This Burmese spinel contains a center cluster of negative crystals within a strongly colored red core. Field of view 1.41 mm.

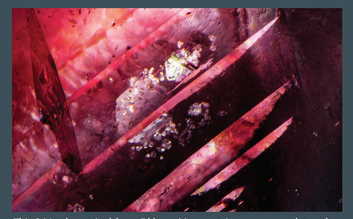

This Sri Lankan spinel from Okkampitiya contains numerous plates of hematite aligned along octahedral planes. Field of view 2.47 mm.

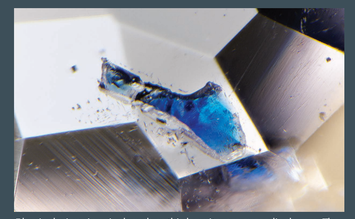

Blue inclusions in spinel, such as this lazurite, are exceedingly rare. The spinel is from Mogok, Myanmar. Field of view 1.60 mm.

Spinel as an Inclusion

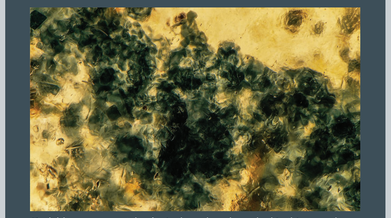

Dark blue-green crystals of spinel are densely packed in this grossular garnet from Tissamaharama, Sri Lanka. Field of view 5.63 mm.

Violet spinel octahedrons are a rare inclusion in Sri Lankan sapphire. Field of view 5.63 mm.

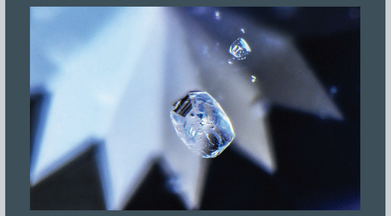

A ghost-like spinel crystal is visible in its spinel host from Okkampitiya, Sri Lanka, due to the partial interface that decorates the surface of the inclusion. Because of the matching optical properties of guest and host, spinel in spinel is often nearly invisible. Field of view 2.27 mm.

This unusual vanadium-rich Burmese ruby contains numerous orangy spinel crystals in addition to elongate crystals of green pargasite. Field of view 4.33 mm.

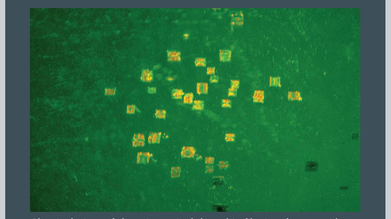

Platy inclusions of chromium spinel show thin-film interference with oblique fiber-optic illumination in this peridot from Myanmar. Field of view 1.44 mm.

This chart contains a selection of photomicrographs of natural, treated, and synthetic spinel. It is by no means comprehensive. The images show the appearance of numerous features a gemologist might observe when viewing spinel with a microscope.

Published in conjunction with Nathan Renfro, John I. Koivula, Shane F. McClure, Kevin Schumacher, and James E. Shigley (2021), "Micro-Features of Spinel," *Gems & Gemology*, Vol. 57, No. 1, pp. 46–49. Photomicrographs by Nathan Renfro and John I. Koivula.

© 2021 Gemological Institute of America

GIA®